

Non-Collinear Magnetism of Ultrathin Magnetic Films

von

Philipp Kurz

Diplomarbeit in Physik

vorgelegt der

Mathematisch-Naturwissenschaftlichen Fakultät

– Fachbereich I –

der

Rheinisch-Westfälischen Technischen Hochschule Aachen

im Januar 1997

angefertigt im

Institut für Festkörperforschung

Forschungszentrum Jülich

Contents

1	Introduction	1
2	The Density Functional Theory	5
2.1	The Theorem of Hohenberg and Kohn	5
2.2	The Kohn-Sham Equations	6
2.3	Spin Density Functional Theory	8
2.4	The Local Spin Density Approximation	9
2.5	Determination of the Total Energy	10
2.6	The Stoner Model of Itinerant Magnetism	11
3	The FLAPW Method	15
3.1	The FLAPW Method	15
3.1.1	The APW Method and its Problems	15
3.1.2	The Concept of LAPW	17
3.1.3	The Concept of FLAPW	19
3.1.4	The Generalized Eigenvalue Problem	20
3.1.5	Film Calculations within FLAPW	21
3.2	Relativity in Valence Electron Calculations	23
3.2.1	The Kohn-Sham-Dirac Equation	24
3.2.2	The Scalar Relativistic Approximation	25
3.3	Construction of the Hamiltonian Matrix	28
3.3.1	Contribution of the Muffin-Tins	29
3.3.2	The Vacuum Contribution	31
3.3.3	The Interstitial Contribution	32
3.3.4	The Muffin-Tin A- and B-Coefficients	34
3.4	Brillouin Zone Integration and Fermi Energy	38
3.5	Representation of the Density and the Potential	40
3.6	Construction of the Electron Density	41
3.6.1	“ <i>l</i> -like” Charge	42
3.6.2	Determination of the Optimal Energy Parameter	42
3.6.3	Construction of the Electron Density in the Muffin-Tins	43
3.6.4	Construction of the Electron Density in the Interstitial Region	44
3.6.5	Construction of the Electron Density in the Vacuum Region	45
3.7	Construction of the Coulomb Potential	46

3.7.1	The Pseudocharge Method	47
3.7.2	Determination of the interstitial Coulomb Potential in Bulk Calculations	48
3.7.3	Determination of the interstitial and vacuum Coulomb Potential in Film Calculations	48
3.8	Computation of the Exchange Correlation Potential	50
3.8.1	Calculation of ϵ_{xc}^σ and V_{xc}^σ in the Interstitial-Region	51
3.8.2	Calculation of ϵ_{xc}^σ and V_{xc}^σ in the Vacuum-Region	51
3.8.3	Calculation of ϵ_{xc}^σ and V_{xc}^σ in the Muffin-Tin Spheres	51
3.9	Minimization of the Energy Functional	52
3.9.1	“simple mixing”	52
3.9.2	The Newton-Raphson Method	53
3.9.3	Quasi-Newton Methods	53
4	Non-Collinear Magnetism in FLAPW	55
4.1	The Frozen Potential Approximation	56
4.2	The Implementation of Non-Collinear Magnetism	59
4.3	Possible Extensions of the Method	62
5	The Local Orbital Extension	63
5.1	Multiple Window FLAPW	64
5.2	Implementation of the Local Orbital Extension	65
5.3	Construction of the Local Orbitals	66
5.4	Hamiltonian and Overlap Matrix Elements	68
5.4.1	The Overlap Matrix Elements	69
5.4.2	The Hamiltonian Matrix Elements	70
5.5	The Electron Density of Local Orbitals	73
5.5.1	“l-like” Charge	74
5.5.2	The Optimal Local Orbital Energy Parameter	74
5.5.3	Construction of the Electron Density in the Muffin-Tins in the Presents of Local Orbitals	75
5.6	Test Calculation on Tungsten and Titanium	77
6	Non-Collinear Magnetism of Unsupported Monolayers with fcc(111) Geometry	83
6.1	Model Structures	84
6.2	Calculational Details	85
6.3	Accuracy of the Frozen Potential Approximation	86
6.4	Results for the Cr UML	87
6.5	Results for the Mn UML	97
7	Conclusion and Outlook	101

Chapter 1

Introduction

The investigation of surfaces and interfaces is a rapidly developing field in modern solid state physics. Experimental and theoretical techniques have advanced tremendously during recent years. The possibility of growing metallic over-layers and multi-layers of high quality opened way to access a completely new class of system with remarkable properties: The ultrathin magnetic films. The preparation of such specimen has become feasible with state of the art epitaxy in combination with sophisticated vacuum technology. With the molecular beam epitaxy (MBE), for example, thin layers can be grown in a precise and controlled way on an atomic scale. Simultaneously, techniques monitoring the growth and characterizing these materials chemically, structurally and electronically have advanced at the same pace. With the scanning tunneling microscope (STM) the structure of surfaces can be studied in real space with atomic resolution. The STM can even be used to place single atoms at a chosen position, and thus to “design” artificial materials atom by atom. Spin-polarized electron techniques have been developed to investigate the magnetism at surfaces and in addition the recently discovered magnetic dichroism can be employed to analyze the magnetic properties. Discoveries like the inter-layer exchange coupling and the giant magnetoresistance, that found their way into industrial application, lead to extensive research activities in the field of thin magnetic films.

In order to understand the complex interactions that lead to a specific magnetic structure, it is necessary to develop a theoretical description of the magnetism at surfaces. An important contribution to the understanding of the physics of surfaces has been obtained from *ab-initio* calculations. With these methods, which contain the charge of the nuclei as the only parameter, ground-state properties like lattice parameter, lattice structure, cohesive energies magnetic moments and magnetic structure can be determined. Bandstructures are calculated to guide the interpretation of experiments. The rapid progress in computer technology made it possible to apply *ab-initio* methods to larger and more complex systems, e.g. systems with broken symmetry, like surfaces. The basis of such calculations is the density functional theory (DFT) by Hohenberg and Kohn [HK64] and Kohn and Sham [KS65], which states, that the ground-state properties of a many electron system are completely determined by the electron (charge) density. However, this theory could not be applied until the local

(spin) density approximation (LSDA) was introduced. This relatively simple approximation to the unknown exchange correlation potential proved to be very successful, describing the electronic structure of most material including the transition metals. On the basis of the DFT and the LSDA many bandstructure methods, which differ by the way the Kohn-Sham equations are solved, have been developed. The results of the present work have been obtain with the full-potential linearized augmented planewave method (FLAPW).

The FLAPW method is an all-electron method. The core electrons are treated (full-) relativistically, taking into account only the spherical part of the potential. The valence electrons are calculated in the scalar-relativistic approximation including the full potential. With no approximation to the shape of the potential being made, the FLAPW method is very suitable for open structures and surfaces. Due to its elaborate expansion of the wavefunctions, including radial functions near the atomic nuclei, the FLAPW method can be applied to transition metals with their localized *d*-electrons. Surfaces are approximated by a thin slab. The necessary extension to the FLAPW method [KPF79] contains an accurate description of the vacuum.

The magnetism and the dimensionality (coordination) of transition-metal systems are closely related. This fact can most easily be realized comparing the two extreme cases of low and high dimension, free atoms and bulk materials. Nearly all transition-metal atoms have magnetic moments, which are well described by Hund's rule. In contrast, only 5 transition-metals (Cr, Mn, Fe, Co and Ni) remain magnetic in the bulk crystalline phase, with magnetic moments that are substantially reduced compared to the free atoms.

Recently, a lot of research has been devoted to transition-metal monolayers, in particular on noble-metal substrates [FPB⁺90, Sie92, LMF85, FFO85, Ter87, BDZD89, FW91, WB93, Blü95]. Because of the filled *d*-bands of the noble-metals the *d*-bands of the transition-metal monolayers hybridize very little with the substrate. This leads to a narrowing of the *d*-bands and an enhancement of the magnetic moments in the overlayers [Blü88, Blü95]. In this context, Fe on the Cu (100) surface belongs to the most extensively investigated systems. Fe on Cu(100) as well as Mn on Cu(100) show complex reconstructions, which are expected to be driven by magnetism. In general the atomic ground-state structure and also the magnetic ground-state structure of systems with low dimension, like overlayers, clusters and nano-structures, is more difficult to predict, because restrictions to the phase-space of possible structures due to symmetry are dropped and more degrees of freedom have to be relaxed.

So far, mainly overlayers on (100) surfaces have been investigated, where the atoms in the monolayer form a square lattice. Two different magnetic structures have been found, the ferromagnetic $p(1 \times 1)$ and the antiferromagnetic $c(2 \times 2)$ structure. It turns out, that the early transition-metals V, Cr and Mn prefer the antiferromagnetic ordering (on Pd, Cu and Ag (100))¹, while Fe, Co and Ni prefer the ferromagnetic structure. However, little work has been done on overlayers on the (111) surface,

¹No magnetic solution has been found for V on Cu (100).

where the atoms are arranged on a hexagonal lattice. Under the assumption, that the antiferromagnetic ordering of the early transition-metals is predominantly driven by the nearest neighbor exchange coupling, spin-frustration has to be expected on the hexagonal lattice. This spin-frustration can be resolved by a non-collinear ground-state. In fact, a Heisenberg model including only nearest neighbor interaction leads to a ground-state, where the spins on each triangle of the hexagonal lattice form 120° angles. Spin-frustrated antiferromagnets are a very general problem in low dimensions. Other expected examples are: i) Small Cr or Mn clusters, where each atom couples antiferromagnetically to its neighbors, ii) Mn monolayers on Fe substrate: Here the Mn atoms couple antiferromagnetically to the nearest neighbor atoms in the monolayer plane, but ferromagnetically to the Fe atoms of the substrate, iii) steps in a Fe covered Cr surface: The Fe atoms couple antiferromagnetically to the Cr substrate. However, the Fe atom at the step edge has two Cr nearest neighbors with opposite magnetization, because the Cr substrate couples antiferromagnetically layer by layer normal to the surface. In all these cases the orientation of the magnetic moments is unclear, and the ground-state might be a non-collinear configuration.

The interest in the hexagonal overlayers is reinforced by the discovery of the complex $c(2 \times 8)$ reconstruction of the Mn monolayer on Cu (100) [FHW92]. Within this reconstruction the Mn atoms are locally hexagonal, while globally the overlayer stays compatible with the geometry of the substrate. This feature suggests, that the Mn monolayer prefers a hexagonal geometry. In order to investigate this Pentcheva [Pen96] removed the influence of the substrate and performed systematic calculations on unsupported monolayers (UML) of the 3d transition-metals. These calculations show, that Mn monolayers prefer the hexagonal structure. However, this result could only be obtained from magnetic calculations, non-magnetic calculations yield a lower energy for the square lattice. This proves, that magnetism can have a strong impact on structural properties. In addition, the investigation by Pentcheva showed, that a collinear antiferromagnetic configuration, where four of the six nearest neighbors of each Mn atom have opposite magnetization and the other two atoms have parallel magnetization, is lower in energy than the ferromagnetic configuration on the hexagonal lattice, which supports the assumption of a non-collinear ground-state. Such systems can only be described accurately if both, the structural and the magnetic degrees of freedom, are relaxed. Therefore, it is necessary to develop a method that combines the calculation of the forces on the atoms with non-collinear magnetism.

So far the majority of *ab-initio* calculations have been performed allowing only parallel or anti-parallel orientation of magnetic moments. With the present work we took a first step towards an extension of the FLAPW method to non-collinear magnetism. Non-collinear configurations of unsupported Cr monolayer with Ag(111) geometry and Mn monolayer with Cu(111) geometry have been compared to the ferromagnetic phase and the antiferromagnetic configuration introduced by Pentcheva. A non-collinear structure proved to be lowest in energy in the case of the Cr monolayer. The results have been obtained non-selfconsistently in the frozen potential approximation.

In chapter 2 the basics of the density functional theory and the local spin-density approximation are discussed. The Stoner model, which provides the framework for the interpretation of the results of the calculation, is briefly reviewed. The FLAPW method is discussed in chapter 3. During this discussion we put emphasize to the computation of the contribution to the Hamiltonian and overlap matrix from the muffin-tin spheres and the construction of the charge density in the spheres, because the corresponding parts of the program have been changed for the implementation of the local orbital extension. In chapter 4 the implementation of non-collinear magnetism is described and the approximations that have been made are discussed. Chapter 5 contains a description of the local orbital extension that has been implemented as part of this work. The local orbitals are extra basis functions added to the FLAPW basis set, which are completely localized inside the muffin-tins. With the improved variational freedom due to this extension it is possible to used a common basis set for the majority and minority spin-states, which is necessary for an efficient implementation for future selfconsistent non-collinear calculations. Test results are presented, where the local orbitals have been applied to the semicore states of bcc Tungsten, fcc and hcp Titanium. The results for the non-collinear calculations on Cr unsupported monolayers with Ag (111) geometry and the Mn monolayer with the Cu (111) geometry are presented in chapter 6. All results are summarized in chapter 7 and ideas for the experimental verification are put forward. The approximations made and deficiencies of the current implementation are review and it is discussed how the results can be improved by extending the method to allow selfconsistent non-collinear calculations.

Chapter 2

The Density Functional Theory

In order to establish a deep understanding of the physical properties of solids, it is of major importance to develop a valid quantum-mechanical description of these systems. However, the atom nuclei and the electrons constitute a complex many-body problem. A simplification of this problem can be achieved employing the Born-Oppenheimer-approximation, within which the atomic nuclei are considered point charges at fixed positions. Thus, all quantum effects of the nuclei are neglected. This approximation, which is made in the vast majority of first-principle calculations, leads to the following Schrödinger equation.

$$\begin{aligned}\mathcal{H}\Psi &= \left\{ -\sum_{i=1}^N \frac{\hbar^2}{2m} \nabla^2 + \sum_{\substack{i,j=1 \\ i \neq j}}^N \frac{e^2}{|\mathbf{r}_i - \mathbf{r}_j|} + \sum_{i=1}^N \sum_{\mu=1}^M \frac{e^2 Z^\mu}{|\mathbf{r}_i - \boldsymbol{\tau}^\mu|} \right\} \Psi(\mathbf{r}_1, \dots, \mathbf{r}_N) \\ &= E\Psi(\mathbf{r}_1, \dots, \mathbf{r}_N)\end{aligned}\tag{2.1}$$

However, due to the large dimension of Ψ and the requirement of antisymmetry, which means that Ψ has to be expanded into a sum of Slater determinants, rather than simple product-functions, this equation can be solved only for tiny systems, including few electrons. In order to deal with realistic materials, relevant in solid state physics, further approximations have to be made.

A breakthrough in the parameter-free *ab-initio* description of complex electronic systems has been achieved with the development of the density functional theory by Hohenberg and Kohn [HK64] and Kohn and Sham [KS65].

2.1 The Theorem of Hohenberg and Kohn

The all-electron wavefunction contains all information available about an electronic system. However, not the whole information is needed to determine the ground state properties of a physical system. The measurable quantities are given by expectation values of the quantum-mechanical operators corresponding to the observable under consideration. The central idea of the density functional theory [JG89] is to replace

the complex many particle wavefunction by a far simpler quantity, the electron density, given by

$$n(\mathbf{r}) = \langle \Psi | \sum_{i=1}^N \delta(\mathbf{r} - \mathbf{r}_i) | \Psi \rangle. \quad (2.2)$$

Hohenberg and Kohn were able to show for systems with a non-degenerate ground state, that:

- For a given external Potential V_{ext} , the ground state energy and all other ground state properties of the system are unique functionals of the electron density $n(\mathbf{r})$.
- The energy functional is variational, i.e. the ground state density $n_0(\mathbf{r})$ minimizes the energy functional $E[n]$, under the subsidiary condition that the number of electrons is kept constant.

$$E[n] > E[n_0] = E_0 \quad \text{for all } n(\mathbf{r}) \neq n_0(\mathbf{r}) \quad (2.3)$$

The density functional formalism can be extended to degenerate ground states [Koh85, DG90]. The second part of the theorem implies, that the ground state density can be obtained from the minimization of the energy functional.

$$\delta E[n] = 0 \quad (2.4)$$

Levy [Lev79] provided a simpler and more general derivation of the above theorems, defining the energy functional by

$$E[n] = \min_{\Psi, n[\Psi]=n} \langle \Psi | \mathcal{H} | \Psi \rangle. \quad (2.5)$$

However, no explicit representation of $E[n]$ has been derived so far.

2.2 The Kohn-Sham Equations

An important step on the way to finding an applicable approximation of the energy functional is the idea of Kohn and Sham [KS65]. The central concept of their theory is to split the energy functional into three contributions.

$$E[n] = T_s[n] + U[n] + E_{xc}[n] \quad (2.6)$$

Where T_s is the kinetic energy of non-interacting electrons. The Coulomb energy U consists of the interaction of the electrons with the external potential, which is usually due to the atomic nuclei, and the electron-electron interaction in Hartree approximation.

$$\begin{aligned} U[n] &= E_{ext}[n] + E_H[n] \\ E_{ext}[n] &= \int V_{ext}(\mathbf{r})n(\mathbf{r})d^3r \\ E_H[n] &= 4\pi \frac{e^2}{2} \int \frac{n(\mathbf{r})n(\mathbf{r}')}{|\mathbf{r} - \mathbf{r}'|} d^3r d^3r' \end{aligned} \quad (2.7)$$

Equation 2.6 can be regarded as a definition of the exchange correlation functional $E_{xc}[n]$, which contains all remaining contributions to $E[n]$, i.e. the exchange and correlation energy and correction to the kinetic energy due to the electron-electron interaction. The importance of this representation of $E[n]$ has two reasons. The kinetic energy of the non-interacting electrons T_s , which is a significant contribution to the total energy, can be calculated exactly. By that, many deficiencies due to inaccurate treatment of the kinetic energy by the Thomas-Fermi method are removed. In addition approximations to $E_{xc}[n]$ can be found, that lead to excellent results for the ground state properties calculated for a wide variety of systems.

An explicit formula for $T_s[n]$ can be obtained using a special ansatz for the electron density. The density can be written as a sum of single particle wavefunctions, as in the case of non-interacting electrons.

$$n(\mathbf{r}) = 2 \sum_{i=1}^N |\psi_i(\mathbf{r})|^2 \quad (2.8)$$

Where, where the sum is over the occupied states and the factor “2” accounts for the spin degeneracy. With this ansatz the kinetic energy can be written as:

$$T_s[n] = -2 \sum_{i=1}^N \int \psi_i^*(\mathbf{r}) \frac{\hbar^2}{2m} \nabla^2 \psi_i(\mathbf{r}) d^3r \quad (2.9)$$

Instead of minimizing the energy functional with respect to the electron density, it can also be minimized with respect to the wavefunctions ψ_i (or their complex conjugates). In this case the subsidiary condition of particle conservation is replaced by the requirement of normalized wavefunctions.

$$\int |\psi_i(\mathbf{r})|^2 d^3r = 1 \quad (2.10)$$

This requirement is taken into account by Lagrange parameters ϵ_i . Applying the variational principle yields the Kohn-Sham equations.

$$\left\{ -\frac{\hbar^2}{2m} \nabla^2 + V_{eff}(\mathbf{r}) \right\} \psi_i(\mathbf{r}) = \epsilon_i \psi_i(\mathbf{r}) \quad (2.11)$$

with

$$V_{eff}(\mathbf{r}) = V_{ext}(\mathbf{r}) + V_H(\mathbf{r}) + V_{xc}(\mathbf{r}) \quad (2.12)$$

These equations have the form of a single particle Schrödinger equations. However, the potential has been replaced by an effective potential consisting of three contributions: The external potential V_{ext} , the Hartree potential

$$V_H(\mathbf{r}) = 4\pi e^2 \int \frac{n(\mathbf{r}')}{|\mathbf{r} - \mathbf{r}'|} d^3r' \quad (2.13)$$

and the exchange correlation potential

$$V_{xc}(\mathbf{r}) = \frac{\delta E_{xc}[n(\mathbf{r})]}{\delta n(\mathbf{r})} \quad (2.14)$$

Since V_H and V_{xc} depend on the electron density, this formalism constitutes a self-consistency problem.

Even though the Kohn-Sham equations have the form of a single-electron Schrödinger equation, the formalism does not provide any justification to interpret the Lagrange parameters ϵ_i as excitation energies, nor to regard the wavefunctions as physical electron wavefunctions. Nevertheless, experience shows, that doing so without formal justification can be meaningful, and helps to understand the properties of the system under consideration.

2.3 Spin Density Functional Theory

In order to describe magnetic effects the density functional theory has to be extended to the case of spin polarized electrons. This is important for systems that possess non-zero ground state magnetization, which is the case for most atoms, magnetic solids and surfaces and electronic systems exposed to an external magnetic field. The necessary extension to the Hohenberg-Kohn theory can be formulated replacing the electron density by the electron density plus the magnetization density as fundamental variables. In this case, the variational principle becomes

$$E[n(\mathbf{r}), \mathbf{m}(\mathbf{r})] \geq E[n_0(\mathbf{r}), \mathbf{m}_0(\mathbf{r})]. \quad (2.15)$$

An alternative, but completely equivalent, formulation can be obtained using a four component density matrix $\rho_{\alpha\beta}$ instead of $n(\mathbf{r})$ and $\mathbf{m}(\mathbf{r})$ [vBH72, Küb95]. In order to gain a generalized form of the Kohn-Sham equations, it is necessary at least to introduce two component Pauli wavefunctions, that reproduce the electron and magnetization density.

$$\boldsymbol{\psi}_i(\mathbf{r}) = \begin{pmatrix} \psi_{1,i}(\mathbf{r}) \\ \psi_{2,i}(\mathbf{r}) \end{pmatrix} \quad (2.16)$$

$$\begin{aligned} n(\mathbf{r}) &= \sum_{i=1}^N |\boldsymbol{\psi}_i(\mathbf{r})|^2 \\ \mathbf{m}(\mathbf{r}) &= \sum_{i=1}^N \boldsymbol{\psi}_i^*(\mathbf{r}) \boldsymbol{\sigma} \boldsymbol{\psi}_i(\mathbf{r}) \end{aligned} \quad (2.17)$$

Applying the variational principle again yields the Kohn-Sham equations, which now have the form of Schrödinger-Pauli equations.

$$\left\{ -\frac{\hbar^2}{2m} \nabla^2 + V_{eff}(\mathbf{r}) + \boldsymbol{\sigma} \cdot \mathbf{B}_{eff}(\mathbf{r}) \right\} \boldsymbol{\psi}_i(\mathbf{r}) = \epsilon_i \boldsymbol{\psi}_i(\mathbf{r}) \quad (2.18)$$

The additional effective magnetic field consists of two terms. One of them is due to the variation of the exchange correlation energy with respect to the magnetization

density. The second term is the external B-field, if present.

$$\begin{aligned}\mathbf{B}_{eff}(\mathbf{r}) &= \mathbf{B}_{xc}(\mathbf{r}) + \mathbf{B}_{ext}(\mathbf{r}) \\ \mathbf{B}_{xc}(\mathbf{r}) &= \frac{\delta E_{xc}[n(\mathbf{r}), \mathbf{m}(\mathbf{r})]}{\delta \mathbf{m}(\mathbf{r})}\end{aligned}\quad (2.19)$$

In many applications, like for example ferromagnetic and antiferromagnetic solids, the magnetization is orientated along one particular direction. For these collinear cases the problem can be simplified further. The z-axis can be chosen along the direction of the magnetic field. Therefore, the Hamiltonian of equation 2.18 becomes diagonal in the two spin components of the wavefunction, i.e. the spin-up and -down problems become completely decoupled and can be solved independently. The energy and all other physical observables become functionals of the electron density and the magnitude of the magnetization density $m(\mathbf{r}) = |\mathbf{m}(\mathbf{r})|$ rather than $\mathbf{m}(\mathbf{r})$, or, equivalently, of the spin-up and spin-down electron densities $n_{\uparrow}(\mathbf{r})$ and $n_{\downarrow}(\mathbf{r})$ which are given by

$$n_{\sigma}(\mathbf{r}) = \sum_{i=1}^N |\psi_{i\sigma}(\mathbf{r})|^2 \quad (2.20)$$

The vast majority of the spin-polarized density functional calculations have been performed using this formalism.

2.4 The Local Spin Density Approximation

So far, no approximations have been made. The density functional formalism, outlined in the previous sections, could in principle reproduce all ground state properties of any complex many-electron system exactly, if the exchange correlation energy E_{xc} was known. Unfortunately, no explicit representation of this functional, that contains all many-body effects, has been found yet. Thus, approximations to E_{xc} have to be used. The most widely used and very successful approximation is the local spin density approximation (LSDA). The underlying idea is very simple. At each point of space E_{xc} is approximated locally by the exchange correlation energy of a homogeneous electron gas with the same electron and magnetization density. Hence, the approximate functional E_{xc} is of the form

$$E_{xc}[n(\mathbf{r}), |\mathbf{m}(\mathbf{r})|] = \int n(\mathbf{r}) \epsilon_{xc}(n(\mathbf{r}), |\mathbf{m}(\mathbf{r})|) d^3r \quad (2.21)$$

It is important to note, that ϵ_{xc} is not a functional, but a function of $n(\mathbf{r})$ and $|\mathbf{m}(\mathbf{r})|$ at a particular point of space. As a consequence of its local definition ϵ_{xc} and thus E_{xc} depend only of the magnitude of the magnetization. This, in terms, leads to the fact that $\mathbf{B}_{xc}(\mathbf{r})$ and $\mathbf{m}(\mathbf{r})$ do always have the same direction. Therefore, the exchange correlation potential and magnetic field derived from 2.21 become

$$V_{xc}(\mathbf{r}) = \epsilon_{xc}(n(\mathbf{r}), |\mathbf{m}(\mathbf{r})|) + n(\mathbf{r}) \frac{\delta \epsilon_{xc}(n(\mathbf{r}), |\mathbf{m}(\mathbf{r})|)}{\delta n(\mathbf{r})}$$

$$\mathbf{B}_{xc}(\mathbf{r}) = n(\mathbf{r}) \frac{\delta \epsilon_{xc}(n(\mathbf{r}), |\mathbf{m}(\mathbf{r})|)}{\delta |\mathbf{m}(\mathbf{r})|} \hat{\mathbf{m}}(\mathbf{r}). \quad (2.22)$$

Using the LSDA the Kohn-Sham equations take exactly the same form as the Hartree equations, and they are no more difficult to solve. In particular, they are far easier to deal with than the Hartree-Fock equations because of the local effective potential. Intuitively one should expect, that the LSDA is valid only for slowly varying densities. Nevertheless, it has been applied successfully to inhomogeneous systems.

Explicit parameterizations of ϵ_{xc} can be obtained for example from Hartree-Fock calculations for the homogeneous electron gas. Of course, such calculations do only take into account the exchange effects, but neglect correlation. Modern parameterizations of ϵ_{xc} are based on quantum-mechanical many-body calculations. Most commonly used are the parameterizations of v. Barth and Hedin [vBH72] and Moruzzi, Janak and Williams [MJW78], which have been obtained applying the random phase approximation (RPA), the parameterization of Vosko, Wilk and Nusair [VWN80], that is based on Quantum-Monte-Carlo simulations by Ceperley and Alder [CA80], and goes beyond the RPA, and the parameterization of Perdew and Zunger [PZ81], which is, in a certain sense, a mixture of the previous two. The results of the present work have been obtained using the parameterization of Moruzzi, Janak and Williams.

2.5 Determination of the Total Energy

If the total energy of a system is needed, for example in order to calculate the equilibrium lattice constant of a crystal, the Coulomb interaction of the atomic nuclei has to be taken into account. This extra contribution E_{ii} (ion-ion) has to be added to the electronic energy, given by 2.6.

$$E[n] = T_s[n] + U[n] + E_{xc}[n] + E_{ii}, \quad E_{ii} = e^2 \sum_{\substack{\mu, \mu'=1 \\ \mu \neq \mu'}}^M \frac{Z^\mu Z^{\mu'}}{|\boldsymbol{\tau}^\mu - \boldsymbol{\tau}^{\mu'}|}, \quad (2.23)$$

where μ sums over all atoms of the crystal with the position $\boldsymbol{\tau}^\mu$. In principle, this formula could be used to calculate the total energy. However, for numerical reasons it is desirable to avoid the explicit application of the operator ∇^2 . Therefore, the kinetic energy is calculated from the sum of the single particle eigenvalues ϵ_i . Rewriting the Schrödinger-Pauli equation 2.18 yields

$$-\frac{\hbar^2}{2m} \nabla^2 \boldsymbol{\psi}_i(\mathbf{r}) = \epsilon_i \boldsymbol{\psi}_i(\mathbf{r}) - V_{eff}(\mathbf{r}) \boldsymbol{\psi}_i(\mathbf{r}) - \boldsymbol{\sigma} \cdot \mathbf{B}_{eff}(\mathbf{r}) \boldsymbol{\psi}_i(\mathbf{r}) \quad (2.24)$$

Multiplying from the left with $\int d^3r \boldsymbol{\psi}_i^*(\mathbf{r}, \sigma)$ and summing over the occupied states gives the kinetic energy.

$$T_s[n] = \sum_{i=1}^N \epsilon_i - \int n(\mathbf{r}) V_{eff}(\mathbf{r}) d^3r - \int \mathbf{m}(\mathbf{r}) \cdot \mathbf{B}_{eff}(\mathbf{r}) d^3r \quad (2.25)$$

Using 2.7, 2.21 and assuming that the external potential is given by the atomic nuclei and that no external magnetic field is present,

$$V_{ext}(\mathbf{r}) = -4\pi e^2 \sum_{\mu=1}^M \frac{Z^\mu}{|\mathbf{r} - \boldsymbol{\tau}^\mu|}, \quad \mathbf{B}_{ext}(\mathbf{r}) = 0 \quad (2.26)$$

the total energy becomes

$$\begin{aligned} E[n, \mathbf{m}] &= \sum_{i=1}^N \epsilon_i - \int n(\mathbf{r}) V_{eff}(\mathbf{r}) d^3 r - \int \mathbf{m}(\mathbf{r}) \cdot \mathbf{B}_{xc}(\mathbf{r}) d^3 r \\ &- 4\pi e^2 \sum_{\mu=1}^M \int \frac{n(\mathbf{r}) Z^\mu}{|\mathbf{r} - \boldsymbol{\tau}^\mu|} d^3 r + 4\pi e^2 \frac{1}{2} \int \frac{n(\mathbf{r}) n(\mathbf{r}')}{|\mathbf{r} - \mathbf{r}'|} d^3 r d^3 r' \\ &+ \int n(\mathbf{r}) \epsilon_{xc}(n(\mathbf{r}), |\mathbf{m}(\mathbf{r})|) d^3 r + 4\pi e^2 \sum_{\substack{\mu, \mu'=1 \\ \mu \neq \mu'}}^M \frac{Z^\mu Z^{\mu'}}{|\boldsymbol{\tau}^\mu - \boldsymbol{\tau}^{\mu'}|}. \end{aligned} \quad (2.27)$$

Using 2.7 and 2.22 this can be simplified further.

$$\begin{aligned} E[n, \mathbf{m}] &= \sum_{i=1}^N \epsilon_i - \int n(\mathbf{r}) V_{xc}(\mathbf{r}) d^3 r - \int \mathbf{m}(\mathbf{r}) \cdot \mathbf{B}_{xc}(\mathbf{r}) d^3 r \\ &- 4\pi e^2 \frac{1}{2} \int \frac{n(\mathbf{r}) n(\mathbf{r}')}{|\mathbf{r} - \mathbf{r}'|} d^3 r d^3 r' \\ &+ \int n(\mathbf{r}) \epsilon_{xc}(n(\mathbf{r}), |\mathbf{m}(\mathbf{r})|) d^3 r + 4\pi e^2 \sum_{\substack{\mu, \mu'=1 \\ \mu \neq \mu'}}^M \frac{Z^\mu Z^{\mu'}}{|\boldsymbol{\tau}^\mu - \boldsymbol{\tau}^{\mu'}|} \end{aligned} \quad (2.28)$$

Equation (2.28) holds exactly for the selfconsistent electron and magnetization density. During the iterations on the way to selfconsistency this result represents only an approximation to the total energy. Another difficulty arises, because the Hartree energy and the contribution from the Coulomb interaction of the nuclei are divergent. Weinert, Wimmer and Freeman [WWF82] showed how these singularities can be canceled analytically.

2.6 The Stoner Model of Itinerant Magnetism

Although all results of the present work have been obtained from *ab-initio* calculations, a brief discussion of the Stoner Model will be given in this section. This model provides a framework within which to interpret the results of the calculations. It is very important to keep these simple models in mind, in order to build ones physical intuition. Comparing ones “intuitive” expectations with the outcome of the calculations is certainly the most important step on the way to understanding the physics of a system. The magnetism of solid is determined by the interplay of the

gain of exchange energy due to the formation of a local moment and the increase of the kinetic energy, if not all \mathbf{k} -states are double occupied within the Fermi sphere. This effect can most easily be illustrated within the Stoner model for ferromagnets.

The magnetization density $m(\mathbf{r}) = |\mathbf{m}(\mathbf{r})|$ of solids is usually small compared to the electron density $n(\mathbf{r})$. Expanding the exchange correlation energy $\epsilon_{xc}(n(\mathbf{r}), m(\mathbf{r}))$ into a Taylor series in terms of the parameter $\xi = \frac{m}{n}$ yields

$$\epsilon_{xc}(n, \xi) = \epsilon_{xc}(n, 0) + \frac{1}{2}\epsilon''_{xc}(n, 0)\xi^2 + \dots \quad (2.29)$$

Thus, the magnetic field \mathbf{B}_{xc} becomes

$$\mathbf{B}_{xc} = \frac{1}{n^2}\epsilon''_{xc}(n, 0)\mathbf{m}. \quad (2.30)$$

In the case of ferromagnetism \mathbf{B}_{xc} acts as an extra potential term \tilde{V}_{xc} , that adds to the non-magnetic exchange correlation potential V_{xc}^0 . This term, which is proportional to m , has the same magnitude for both spin-directions, but it is attractive for the majority-spin (+) and repulsive for the minority-spin(-).

$$V_{xc}^{\pm}(\mathbf{r}) = V_{xc}^0(\mathbf{r}) \mp \tilde{V}_{xc}(\mathbf{r})m(\mathbf{r}) \quad (2.31)$$

Within the Stoner theory this rising and lowering of the potential is expressed by a constant.

$$V_{xc}^{\pm}(\mathbf{r}) = V_{xc}^0(\mathbf{r}) \mp \frac{1}{2}IM \quad (2.32)$$

Where M is the total magnetic moment per atom, and I is the exchange integral (Stoner parameter). Because of this constant shift the spatial shape of the potential remains the same as in the non-magnetic case. Consequently, the solutions of the Kohn-Sham equations also remain unchanged, only the single particle energies ϵ_i are shifted by the same amount as the potential.

$$\psi_i^{\pm}(\mathbf{r}) = \psi_i^0(\mathbf{r}), \quad \epsilon_i^{\pm} = \epsilon_i^0 \mp \frac{1}{2}IM \quad (2.33)$$

Hence, the whole band structure is spin-split, but the shape of the bands remains unchanged. As a result, the local densities of states projected on an atom for the spin-directions $\pm, n^{\pm}(\epsilon)$, are also shifted by $\pm\frac{1}{2}IM$.

$$n^{\pm}(\epsilon) = n^0(\epsilon \pm \frac{1}{2}IM) \quad (2.34)$$

From this property of the density of states a criterion for the existence of ferromagnetism can be derived. Integrating the density of states up to the Fermi energy E_F yields the number of electrons N and the total magnetic moment per atom M .

$$\begin{aligned} N &= \int_{\epsilon < E_F} \left[n^0(\epsilon + \frac{1}{2}IM) + n^0(\epsilon - \frac{1}{2}IM) \right] d\epsilon \\ M &= \int_{\epsilon < E_F} \left[n^0(\epsilon + \frac{1}{2}IM) - n^0(\epsilon - \frac{1}{2}IM) \right] d\epsilon \end{aligned} \quad (2.35)$$

These two equations determine the unknown Fermi energy and magnetic moment. Requiring charge neutrality the first equation can be used to obtain the Fermi energy as a function of the magnetization $E_F = E_F(M)$. Substituting this into the second equation leads to a selfconsistency problem for M .

$$M = F(M), \quad F(M) = \int_{\epsilon < E_F(M)} \left[n^0(\epsilon + \frac{1}{2}IM) - n^0(\epsilon - \frac{1}{2}IM) \right] d\epsilon \quad (2.36)$$

The function $F(M)$ has the following properties.

- $F(0) = 0$
- $F(M) = -F(-M)$
- $F(\pm\infty) = \pm M_\infty$
- $F'(M) > 0$

Where M_∞ is the largest possible magnetization, reached when only majority-spin states are occupied. The graphic solution of 2.36 is illustrated in Fig. 2.1. Two

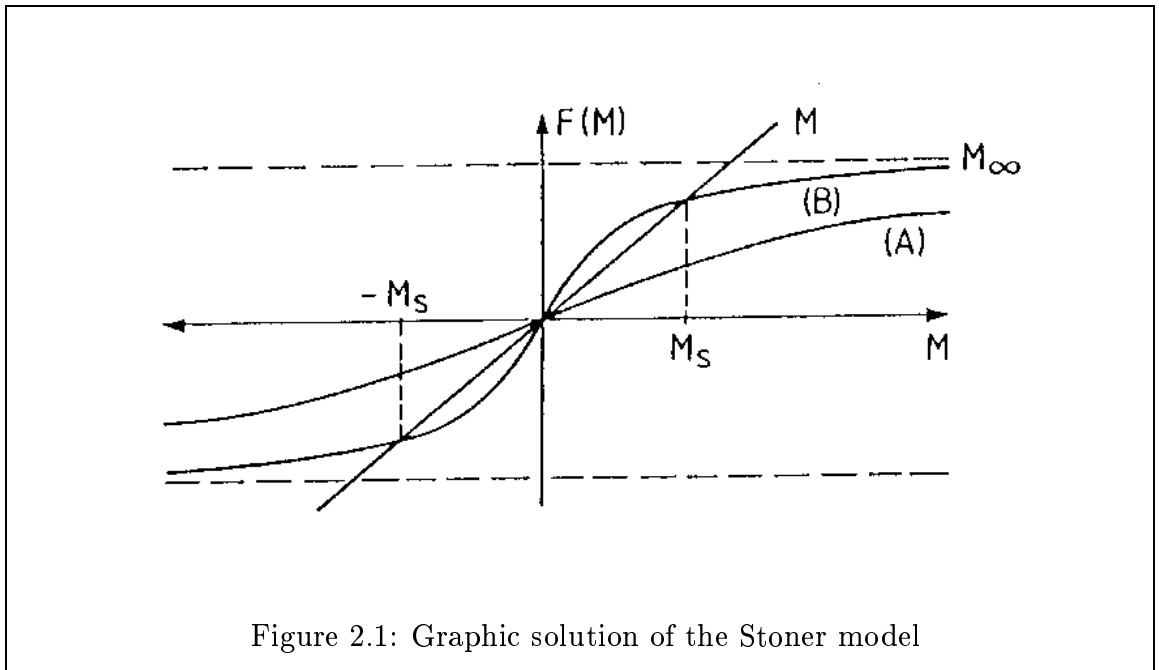


Figure 2.1: Graphic solution of the Stoner model

functions $F(M)$, consistent with the above properties, are plotted. In case A only the trivial non-magnetic solution $M = 0$ is present, whereas in case B three solutions exist, two of which have non-zero magnetization. From the properties of $F(M)$ follows, that 2.36 always has solutions with non-zero magnetization, if the slope of $F(M)$ at $M = 0$ is larger than 1. From 2.36 follows that the slope of $F(M)$ is given by

$$F'(0) = In^0(E_F). \quad (2.37)$$

This finally is the Stoner criterion for ferromagnetism:

$$In^0(E_F) > 1. \quad (2.38)$$

A big exchange integral and a large non-magnetic density of states at the Fermi energy favors ferromagnetism. This result is not surprising, because a large $n^0(E_F)$ means, that only a small increase in kinetic energy has to be accepted to obtain a large magnetization, and thus a large gain of exchange energy. In the most simple approximation the size of the density of states is proportional to the inverse of the bandwidth W . Thus, the smaller the bandwidth is, the larger the tendency towards magnetism becomes. The limiting case of zero bandwidth are atoms. Here the Stoner criterion is always satisfied, and the magnetic moments are determined by Hund's rule, with the exception of the Lanthanides and the Actinides. The only bulk materials that fulfill the Stoner criterion are Fe, Co and Ni. However, due to the reduced coordination, the bandwidth at surfaces is smaller than in bulk materials. Thus, from the Stoner model one should expect an enhancement of magnetism at surfaces and even new magnetic materials, which are non-magnetic in their bulk crystalline phase, but become magnetic at the surface.

Chapter 3

The FLAPW Method

3.1 The FLAPW Method

There are many possible ways to solve the Kohn-Sham equations. One very common method is to use some kind of basis set to represent the wavefunctions. A very suitable choice that is already suggested by Bloch's theorem are plane waves. They have a lot of advantages: They are orthogonal, they are diagonal in momentum and any power of momentum and the implementation of planewave based methods is rather straightforward because of their simplicity. However, since the electron wavefunctions are varying very quickly near the core, large wavevectors are needed to represent the wavefunctions accurately. This makes planewaves very inefficient. To overcome this problem one can employ pseudopotential techniques, which allow an accurate description of the wavefunctions between the atoms, but avoid the fast oscillations near the core. Thus, less basis functions are needed. Another way to solve this problem is to use a basis set, which contains radial wavefunctions to describe the oscillations near the core. This has already been suggested by Slater [Sla37]. The corresponding technique is called the augmented planewave method (APW).

3.1.1 The APW Method and its Problems

Within the APW approach, space is divided into spheres centered at each atom site, the so-called muffin-tins, and the remaining interstitial region (cf. fig. 3.1). Inside the muffin-tins the potential is approximated to be spherically symmetric, and in many implementations the interstitial potential is set constant. The restrictions to the potential are commonly called shape-approximations. Noting that planewaves solve the Schrödinger equation in a constant potential, while spherical harmonics times a radial function are the solution in a spherical potential, suggests to expand the single

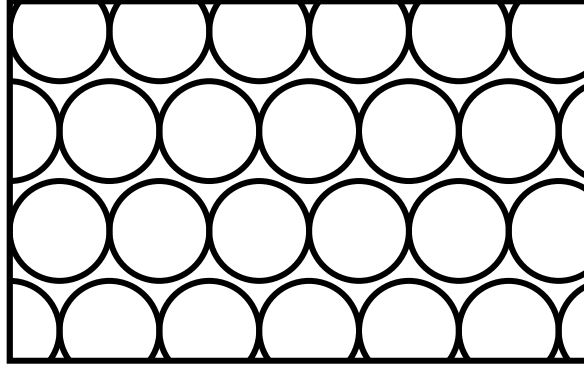


Figure 3.1: The division of space in the APW method. The muffin-tin spheres are surrounded by the interstitial region.

particle wavefunctions¹ $\phi_\nu(\mathbf{k}, \mathbf{r})$ in terms of the following basis functions:

$$\varphi_{\mathbf{G}}(\mathbf{k}, \mathbf{r}) = \begin{cases} e^{i(\mathbf{G}+\mathbf{k})\mathbf{r}} & \text{interstitial region} \\ \sum_{lm} A_L^{\mu\mathbf{G}}(\mathbf{k}) u_l(r) Y_L(\hat{\mathbf{r}}) & \text{muffin-tin } \mu \end{cases} \quad (3.1)$$

Where \mathbf{k} is the Bloch vector, Ω is the cell volume, \mathbf{G} is a reciprocal lattice vector, L abbreviates the quantum numbers l and m and u_l is the regular solution of the radial Schrödinger equation

$$\left\{ -\frac{\hbar^2}{2m} \frac{\partial^2}{\partial r^2} + \frac{\hbar^2}{2m} \frac{l(l+1)}{r^2} + V(r) - E_l \right\} r u_l(r) = 0 \quad (3.2)$$

Here E_l is an energy parameter and $V(r)$ is the spherical component of the potential. The coefficients $A_L^{\mu\mathbf{G}}(\mathbf{k})$ are determined from the requirement, that the wavefunctions have to be continuous at the boundary of the muffin-tin spheres.

Hence, the APW's form a set of continuous basis functions that cover all space. Where each function consists of a planewave in the interstitial region plus a sum of functions, which are solutions of the Schrödinger equation to a given set of angular momentum quantum numbers lm and a given parameter E_l , inside the muffin-tin spheres.

If the E_l were kept fixed, used only as a parameter during the construction of the basis, the hamiltonian could be set up in terms of this basis. This would lead to a standard secular equation for the band energies. Unfortunately, it turns out, that the

¹I will only discuss the application of FLAPW to systems that possess either 2- or 3-dimensional translational symmetry, i.e. bulk crystals or thin crystal films.

APW basis does not offer enough variational freedom if the E_l are kept fixed. An accurate description can only be achieved if they are set to the corresponding band energies. However, requiring the E_l 's to equal the band energies, the latter can no longer be determined by a simple diagonalization of the Hamiltonian matrix. Since the u_l 's depend on the band energies, the solution of the secular equation becomes a nonlinear problem, which is computationally much more demanding than a secular problem.

Another disadvantage of the APW method is, that it is difficult to extend beyond the spherically averaged muffin-tin potential approximation, because in the case of a general potential the optimal choice of E_l is no longer the band energy. And finally, but less serious, if, for a given choice of E_l , the radial functions u_l vanish at the muffin tin radius, the boundary conditions on the spheres cannot be satisfied, i.e. the planewaves and the radial functions become decoupled. This is called the asymptote problem. It can already cause numerical difficulties if u_l becomes very small at the sphere boundary.

Further information about the APW method can be found in the book by Loucks [Lou67], which also reprints several early papers including Slater's original publication [Sla37].

3.1.2 The Concept of LAPW

The basic idea of the linearized augmented planewave method (LAPW) is to add extra variational freedom to the basis inside the muffin-tins, so that it is not necessary to set the E_l equal to the band energy. This is done by using not only the radial solution of the Schrödinger equation, but also its derivative with respect to the energy. This construction, which was first suggested by Andersen [And75], can be regarded as a linearization of the APW. To realize this recall that in the APW method the u_l 's depend on the band energies and can thus be understood as functions of r and ϵ . Hence, u_l can be expanded into a Taylor-series around E_l .

$$u_l(\epsilon, r) = u_l(E_l, r) + \dot{u}_l(E_l, r)(\epsilon - E_l) + O[(\epsilon - E_l)^2] \quad (3.3)$$

Here \dot{u}_l denotes the energy derivative of u_l , $\partial u_l(\epsilon, r)/\partial \epsilon$, and $O[(\epsilon - E_l)^2]$ denotes errors that are quadratic in the energy difference. Ergo, the LAPW method introduces an error of order $(\epsilon - E_l)^2$ in the wavefunction. Therefore, according to the variational principle the error in the calculated band energies is of the order $(\epsilon - E_l)^4$. Because of this high order, the linearization works very well even over rather broad energy regions. In most cases a single set of energy parameters is sufficient for the whole valence band. However, sometimes the energy region has to be split up in two (very rarely more) windows with separate sets of energy parameters.

But let's turn to some important properties of the LAPW basis first, before dis-

cussing its quality and accuracy. The LAPW basis functions are of the form

$$\varphi_{\mathbf{G}}(\mathbf{k}, \mathbf{r}) = \begin{cases} e^{i(\mathbf{G}+\mathbf{k})\mathbf{r}} & \text{interstitial region} \\ \sum_L A_L^{\mu\mathbf{G}}(\mathbf{k}) u_l(r) Y_L(\hat{\mathbf{r}}) + B_L^{\mu\mathbf{G}}(\mathbf{k}) \dot{u}_l(r) Y_L(\hat{\mathbf{r}}) & \text{muffin-tin } \mu \end{cases} \quad (3.4)$$

with the extra term $B_L^{\mu\mathbf{G}} \dot{u}_l(r) Y_L(\hat{\mathbf{r}})$ compared to the APW method. The additional coefficient is determined by requiring that not only the basis functions, but also their derivatives with respect to r are continuous at the sphere boundaries. It is useful to require the following normalization.

$$\langle u|u \rangle = \int_0^{R_{MT}} u_l^2(r) r^2 dr = 1 \quad (3.5)$$

Here R_{MT} is the muffin-tin radius. Taking the derivative of (3.5) with respect to the energy it can easily be shown, that u_l and \dot{u}_l are orthogonal. \dot{u}_l is calculated from a Schrödinger-like equation, derived by taking the energy derivative of (3.2).

$$\left\{ -\frac{\hbar^2}{2m} \frac{\partial^2}{\partial r^2} + \frac{\hbar^2}{2m} \frac{l(l+1)}{r^2} + V(r) - E_l \right\} r \dot{u}_l(r) = r u_l(r) \quad (3.6)$$

Still the solution of this equation has to be made orthogonal to u_l , since any linear combination of \dot{u}_l and u_l also solves the equation. Once the u_l and \dot{u}_l are made orthogonal the basis functions inside the spheres form a completely orthogonal basis set, since the angular functions $Y_{lm}(\hat{\mathbf{r}})$ are also orthogonal. However, the LAPW functions are in general not orthogonal to the core states, which are treated separately in the LAPW method. This fact can cause problems in the presence of high lying core states. A detailed discussion of these problems and strategies to circumvent them can be found in the book by Singh [Sin94], which includes a very comprehensive review of many aspects of the LAPW method.

With the construction of the LAPW basis the main problems of the APW method are solved:

- Since it is no longer necessary to set the energy parameters equal the band energies, the later can be determined by a single diagonalization of the Hamiltonian matrix.
- The LAPW method can be extended to nonspherical muffin tin potentials with little difficulty, because the basis offers enough variational freedom. This leads then to the full-potential linearized augmented planewave method (FLAPW).
- If u_l is zero at the sphere boundary, its radial derivative and \dot{u}_l are in general nonzero. Hence, the boundary conditions can always be satisfied and there is no asymptote problem.

As a final remark it is worth mentioning, that the nonlinearity inherent to the APW method can only be circumvented at the expense of a larger eigenvalue problem. To

see this, recall that within LAPW (and also within APW) the basis functions are represented by planewaves. The functions inside the muffin tins are coupled to the planewaves via the boundary conditions, and can only varied indirectly by a variation of the planewave coefficients. Clearly, with a finite number of planewaves, at maximum the same number of functions inside the spheres can be varied independently. Hence, to make use of the of the extra variational freedom, that the LAPW basis set allows compared to the APW basis, i.e. to vary the u_l 's and the \dot{u}_l 's independently, more planewaves have to be used.

3.1.3 The Concept of FLAPW

In the past the majority of applications of APW and LAPW² method employed shape-approximations on the potential used in the Hamiltonian. Typically, the potential in the unit cell $V(\mathbf{r})$ is approximated by $V_0(\mathbf{r})$,

$$V(\mathbf{r}) = \begin{cases} V_I^0 = \text{const.} & \text{interstitial region} \\ V_{MT}^0(r) & \text{muffin-tin} \end{cases} \quad (3.7)$$

using a constant potential in the interstitial region and a spherically symmetric potential inside each sphere.

While the LAPW method yields accurate results for close-packed metal systems the shape-approximation becomes difficult to justify for crystals with open structures such as silizides, perovskides, surfaces or clusters.

In the full-potential LAPW method (FLAPW) [Ham79, WKWF81] any shape-approximations in the interstitial region and inside the muffin-tins are dropped. This generalization is achieved by relaxing the constant interstitial potential V_I^0 and the spherical muffin-tin approximation $V_{MT}^0(r)$ due to the inclusion of a warped interstitial $\sum V_I^{\mathbf{G}} e^{i\mathbf{G}\mathbf{r}}$ and the non-spherical terms inside the muffin-tin spheres:

$$V(\mathbf{r}) = \begin{cases} \sum_{\mathbf{G}} V_I^{\mathbf{G}} e^{i\mathbf{G}\mathbf{r}} & \text{interstitial region} \\ \sum_L V_{MT}^L(r) Y_L(\hat{\mathbf{r}}) & \text{muffin-tin} \end{cases} \quad (3.8)$$

This method became possible with the development of a technique for obtaining the Coulomb potential for a general periodic charge density without shape-approximations and with the inclusion of the Hamiltonian matrix elements due to the warped interstitial and non-spherical terms of the potential. The charge density is represented in the same way as the potential:

$$\rho(\mathbf{r}) = \begin{cases} \sum_{\mathbf{G}} \rho_I^{\mathbf{G}} e^{i\mathbf{G}\mathbf{r}} & \text{interstitial region} \\ \sum_L \rho_{MT}^L(r) Y_L(\hat{\mathbf{r}}) & \text{muffin-tin} \end{cases} \quad (3.9)$$

²There are APW and LAPW methods available which include the warped interstitial potential [Koe72].

Detail of the solution of the Poisson equation for an arbitrarily shaped periodic potential are described in section 3.7.

3.1.4 The Generalized Eigenvalue Problem

After discussing the FLAPW basis it is necessary to say a few words about the eigenvalue problem. The solution of the eigenvalue problem has to be carried out separately for every Bloch vector. And, of course, the basis set and the Hamiltonian matrix have to be set up for each Bloch vector. However, I will not add the index \mathbf{k} to the basis functions and the Hamiltonian matrix.

There is one important fact that I have not mentioned so far. Even though plane-waves form an orthogonal basis set, the FLAPW functions do not. The plane-waves in the interstitial-region are non-orthogonal, because the muffin-tin are cut out, i.e. the integration, in terms of which orthogonality is defined, does not stretch over the whole unit cell, but only over interstitial region. An additional contribution comes from the muffin-tin. Even though the $u_l(r)Y_L$ and $\dot{u}_l(r)Y_L$ are mutually orthogonal, in general each plane-wave couples to all functions in the spheres.

Due to the non-orthogonality of the basis functions the overlap matrix \mathbf{S} , defined by (3.10), is not a diagonal, but a hermitian matrix.

$$S^{\mathbf{G}'\mathbf{G}} = \int \varphi_{\mathbf{G}'}^*(\mathbf{r})\varphi_{\mathbf{G}}(\mathbf{r})d^3r \quad (3.10)$$

In (the more convenient) Dirac notation the eigenvalue problem has the following form.

$$\mathcal{H}|\phi_i\rangle = \epsilon_i|\phi_i\rangle \quad (3.11)$$

Where $|\phi_i\rangle$ denotes the eigenfunction corresponding to the i^{th} eigenvalue ϵ_i . Substituting the expansion of the eigenfunctions

$$|\phi_i\rangle = \sum_{\mathbf{G}} c_{i\mathbf{G}}|\varphi_{\mathbf{G}}\rangle \quad (3.12)$$

we obtain

$$\sum_{\mathbf{G}} c_{i\mathbf{G}}\mathcal{H}|\varphi_{\mathbf{G}}\rangle = \epsilon_i \sum_{\mathbf{G}} c_{i\mathbf{G}}|\varphi_{\mathbf{G}}\rangle \quad (3.13)$$

Multiplying this from the left with $\langle\varphi_{\mathbf{G}'}|$ we find

$$\sum_{\mathbf{G}} c_{i\mathbf{G}}\langle\varphi_{\mathbf{G}'}|\mathcal{H}|\varphi_{\mathbf{G}}\rangle = \epsilon_i \sum_{\mathbf{G}} c_{i\mathbf{G}}\langle\varphi_{\mathbf{G}'}|\varphi_{\mathbf{G}}\rangle \quad (3.14)$$

which can be written in matrix form

$$\{\mathbf{H} - \epsilon_i\mathbf{S}\}\mathbf{c}_i = 0 \quad (3.15)$$

where the eigenvector \mathbf{c}_i is the coefficient vector corresponding to the i^{th} eigenvalue. (3.15) is called a generalized eigenvalue problem.

However, this problem can be reduced to a standard eigenvalue problem using the Cholesky decomposition. It can be shown (e.g. Stoer [Sto94]), that any hermitian and positive definite matrix can be decomposed into a matrix product of a lower triangular with only positive diagonal elements matrix and its transposed. Clearly, the overlap matrix satisfies these conditions and can be written

$$\mathbf{S} = \mathbf{L}\mathbf{L}^{tr} \quad (3.16)$$

Therefore (3.15) becomes

$$\mathbf{H}\mathbf{c}_i = \epsilon_i \mathbf{L}\mathbf{L}^{tr} \mathbf{c}_i \quad (3.17)$$

multiplying from the left with \mathbf{L}^{-1} and introducing a unit matrix we get

$$\mathbf{L}^{-1}\mathbf{H}(\mathbf{L}^{-1})^{tr}\mathbf{L}^{tr} \mathbf{c}_i = \epsilon_i \mathbf{L}^{tr} \mathbf{c}_i \quad (3.18)$$

defining

$$\mathbf{P} = \mathbf{L}^{-1}\mathbf{H}(\mathbf{L}^{-1})^{tr}, \quad \mathbf{x}_i = \mathbf{L}^{tr} \mathbf{c}_i \quad (3.19)$$

we finally have

$$\mathbf{P}\mathbf{x}_i = \epsilon_i \mathbf{x}_i \quad (3.20)$$

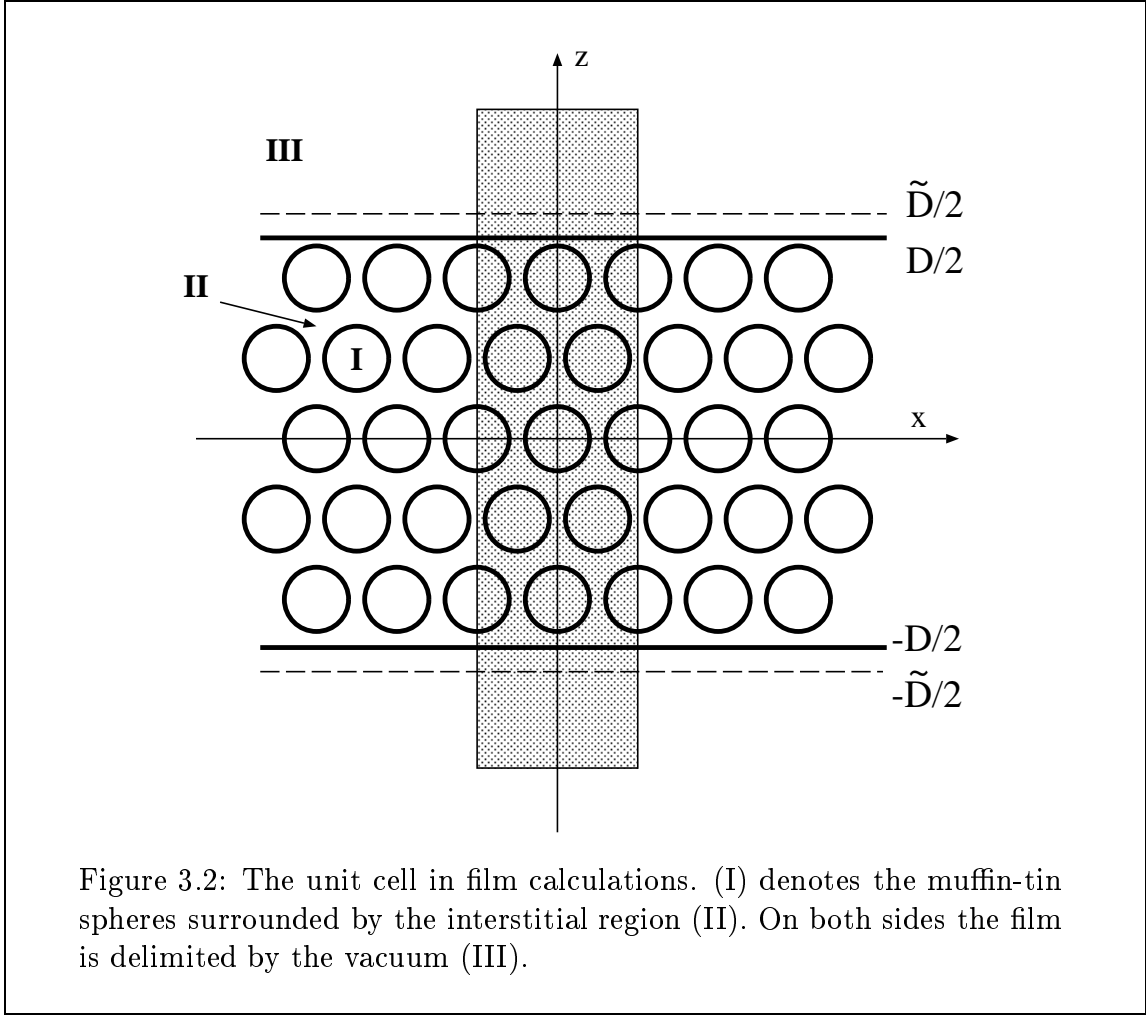
Thus the generalized eigenvalue problem has been reduced to a simple eigenvalue problem. The eigenvectors \mathbf{c}_i can be obtained by the back-transformation

$$\mathbf{c}_i = (\mathbf{L}^{tr})^{-1} \mathbf{x}_i \quad (3.21)$$

3.1.5 Film Calculations within FLAPW

Nowadays the physics of surfaces is an field of major interest and investigation. However, surfaces are difficult to treat, because they break the translational symmetry, i.e. there is only the 2-dimensional symmetry parallel to the surface left to be used to reduce the problem, and a semi-infinite problem is left perpendicular to the surface. In our approach surfaces are approximated by thin films, typically 10–15 atomic layers thick. Obviously, this approximation, which is called the thin-slab approximation, can only yield good results if the interaction between the two surfaces of the film is weak enough, so that each of them shows the properties of the surfaces of an ideal semi-infinite crystal.

In the case of film calculations space is divided into three distinct regions, the muffin-tins, the interstitial and the vacuum region (cf. fig. 3.2). The interstitial region now stretches from $-D/2$ to $D/2$ in z -direction, which is defined to be the direction perpendicular to the film. The representation of the wavefunctions inside the muffin-tin spheres remains exactly the same as in the bulk case. Since the periodicity along the z -direction is lost, the unit cell extends principally from $-\infty$ to ∞ in z -direction. Still the wavefunctions can be expanded in terms of planewaves. However, the wavevectors perpendicular to the film are not defined in terms of D , but in terms



of \tilde{D} , which is chosen larger than D to gain greater variational freedom. Therefore, the planewaves have the form

$$\varphi_{\mathbf{G}_{\parallel}G_{\perp}}(\mathbf{k}_{\parallel}, \mathbf{r}) = e^{i(\mathbf{G}_{\parallel} + \mathbf{k}_{\parallel})\mathbf{r}_{\parallel}} e^{iG_{\perp}z} \quad (3.22)$$

with

$$G_{\perp} = \frac{2\pi n}{\tilde{D}} \quad (3.23)$$

where \mathbf{G}_{\parallel} and \mathbf{k}_{\parallel} are the 2-dimensional wave- and Bloch vectors, \mathbf{r}_{\parallel} is the parallel component of \mathbf{r} and G_{\perp} is the wavevector perpendicular to the film. The basis functions in the vacuum region are constructed in the same spirit as the functions in the muffin-tins. They consist of planewaves parallel to the film, and a z -dependent function $u_{\mathbf{G}_{\parallel}}(\mathbf{k}_{\parallel}, z)$, which solves the corresponding 1-dimensional Schrödinger equation (3.24), plus its energy derivative $\dot{u}_{\mathbf{G}_{\parallel}}(\mathbf{k}_{\parallel}, z)$.

$$\left\{ -\frac{\hbar^2}{2m} \frac{\partial^2}{\partial z^2} + V_0(z) - E_{vac} + \frac{\hbar^2}{2m} (\mathbf{G}_{\parallel} + \mathbf{k}_{\parallel})^2 \right\} u_{\mathbf{G}_{\parallel}}(\mathbf{k}_{\parallel}, z) = 0 \quad (3.24)$$

E_{vac} is the vacuum energy parameter and $V_0(z)$ is the planar averaged part of the vacuum potential. As in the case of \dot{u}_l in the muffin-tins, the function $\dot{u}_{\mathbf{G}_{\parallel}}(\mathbf{k}_{\parallel}, z)$ is calculated from a Schrödinger-like equation, which can be obtained by deriving (3.24) with respect to the energy.

$$\left\{ -\frac{\hbar^2}{2m} \frac{\partial^2}{\partial z^2} + V_0(z) - E_{vac} + \frac{\hbar^2}{2m} (\mathbf{G}_{\parallel} + \mathbf{k}_{\parallel})^2 \right\} \dot{u}_{\mathbf{G}_{\parallel}}(\mathbf{k}_{\parallel}, z) = u_{\mathbf{G}_{\parallel}}(\mathbf{k}_{\parallel}, z) \quad (3.25)$$

The resulting basis functions have the form

$$\varphi_{\mathbf{G}_{\parallel}G_{\perp}}(\mathbf{k}_{\parallel}, \mathbf{r}) = \left\{ A_{\mathbf{G}_{\parallel}G_{\perp}}(\mathbf{k}_{\parallel}) u_{\mathbf{G}_{\parallel}}(\mathbf{k}_{\parallel}, z) + B_{\mathbf{G}_{\parallel}G_{\perp}}(\mathbf{k}_{\parallel}) \dot{u}_{\mathbf{G}_{\parallel}}(\mathbf{k}_{\parallel}, z) \right\} e^{i(\mathbf{G}_{\parallel} + \mathbf{k}_{\parallel})\mathbf{r}_{\parallel}} \quad (3.26)$$

The coefficients $A_{\mathbf{G}_{\parallel}G_{\perp}}(\mathbf{k}_{\parallel})$ and $B_{\mathbf{G}_{\parallel}G_{\perp}}(\mathbf{k}_{\parallel})$ are determined in exactly the same way as it is done for the muffin-tins by requiring that the functions are continuous and differentiable at the vacuum boundary. It should be mentioned, that the vacuum basis functions offer less variational freedom than the basis set in the interstitial region does. This can be seen by noting that there are only two functions, $u_{\mathbf{G}_{\parallel}}$ and $\dot{u}_{\mathbf{G}_{\parallel}}$ times the corresponding planar planewave, to be matched to all planewaves of the interstitial region with the same \mathbf{G}_{\parallel} . But there are generally far more than two different G_{\perp} 's, i.e the number of basis functions in the vacuum region is significantly smaller than in the interstitial region. However, this can be improved rather easily. In equation 3.24 only one energy parameter E_{vac} is used. Instead one can use a whole series of parameters E_{vac}^i to cover an energy region. A possible choice of the energy parameters could be $E_{vac}^i = E_{vac}^{G_{\perp}} = E_{vac} - \frac{\hbar^2}{2m} G_{\perp}^2$, which leads correspondingly to G_{\perp} dependent basis functions $u_{\mathbf{G}_{\parallel}G_{\perp}}(\mathbf{k}_{\parallel}, z)$. For more details see [NKD86]. In general, however, the present approximations is accurate, the energy spectrum of the electrons in the vacuum region is small due to the work-function.

Finally we would like to summarize the basis set used for thin film calculation with the FLAPW method.

$$\varphi_{\mathbf{G}_{\parallel}G_{\perp}}(\mathbf{k}_{\parallel}, \mathbf{r}) = \begin{cases} e^{i(\mathbf{G}_{\parallel} + \mathbf{k}_{\parallel})\mathbf{r}_{\parallel}} e^{iG_{\perp}z} & \text{Int.} \\ \left\{ A_{\mathbf{G}_{\parallel}G_{\perp}}(\mathbf{k}_{\parallel}) u_{\mathbf{G}_{\parallel}}(\mathbf{k}_{\parallel}, z) \right. \\ \left. + B_{\mathbf{G}_{\parallel}G_{\perp}}(\mathbf{k}_{\parallel}) \dot{u}_{\mathbf{G}_{\parallel}}(\mathbf{k}_{\parallel}, z) \right\} e^{i(\mathbf{G}_{\parallel} + \mathbf{k}_{\parallel})\mathbf{r}_{\parallel}} & \text{Vac.} \\ \sum_L A_L^{\mu\mathbf{G}}(\mathbf{k}) u_l(r) Y_L(\hat{\mathbf{r}}) + B_L^{\mu\mathbf{G}}(\mathbf{k}) \dot{u}_l(r) Y_L(\hat{\mathbf{r}}) & \text{MT } \mu \end{cases} \quad (3.27)$$

This expansion has been suggested by H. Krakauer, M. Posternak and A.J. Freeman [KPF79].

3.2 Relativity in Valence Electron Calculations

Relativistic effects are important for the correct numerical description of core or valence electrons. Both core and valence electrons have finite wavefunctions near the

nucleus, where the kinetic energy is large. This kinetic energy enhancement becomes more significant for heavier elements and compounds. Additionally, only relativistic effects, in particular the spin-orbit-coupling, introduce a link between spatial and spin coordinates. Thus, information about the orientation of spins relative to the lattice can only be gained if relativity is taken into account. For fully relativistic description of the electronic structure all relativistic effects (mass-velocity, Darwin-term, spin-orbit coupling) have to be taken into account [SDKW]. However, in many applications an approximation is used, where the spin-orbit interaction is neglected. This approximation is called the scalar relativistic approximation.

3.2.1 The Kohn-Sham-Dirac Equation

In a relativistic density functional theory the Kohn-Sham equation has the form of a single particle Dirac equation

$$\{c\boldsymbol{\alpha} \cdot \mathbf{p} + (\beta - 1)mc^2 + V^{eff}(\mathbf{r})\} \Psi = E\Psi \quad (3.28)$$

$$\boldsymbol{\alpha} = \left(\left(\begin{array}{cc} 0 & \sigma_x \\ \sigma_x & 0 \end{array} \right), \left(\begin{array}{cc} 0 & \sigma_y \\ \sigma_y & 0 \end{array} \right), \left(\begin{array}{cc} 0 & \sigma_z \\ \sigma_z & 0 \end{array} \right) \right)^{tr} = \left(\begin{array}{cc} 0 & \boldsymbol{\sigma} \\ \boldsymbol{\sigma} & 0 \end{array} \right) \quad (3.29)$$

$$\beta = \left(\begin{array}{cc} \mathbf{I}_2 & 0 \\ 0 & -\mathbf{I}_2 \end{array} \right) \quad (3.30)$$

Here, σ_x σ_y σ_z are the Pauli matrices and $\boldsymbol{\sigma}$ is the vector of Pauli matrices, \mathbf{p} is the momentum operator, and I_n denotes an $(n \times n)$ unit matrix. V^{eff} is the effective potential, that contains electron-nucleon Coulomb potential, Hartree potential and exchange-correlation potential. In the case of non-zero spin-polarization, V^{eff} becomes spin-dependent. Finally, Ψ is the relativistic four component wavefunction.

The straightforward way to solve this problem would be to expand each of the four components of Ψ in terms of the FLAPW basis. However, if all four components were treated with the same accuracy, this would result in a basis set which contains four times as many functions as in the non-relativistic (non-magnetic) case. Since the numerical effort of the Hamiltonian diagonalization scales with the dimension of the matrix to the power of three, this would increase the computing time needed for the diagonalization by a factor of 64.

The FLAPW implementation we use introduces some approximations to make relativistic calculations more efficient. One of these approximations is the scalar relativistic approximations, which has been suggested by D.D. Koelling and B.N. Harmon [KH77], where the spin-orbit term is neglected, and spin and spatial coordinates become decoupled. Hence, the Hamiltonian matrix reduces to two matrices of half the size, which can be diagonalized separately. This saves a factor of four in computing time. The scalar relativistic approximation will be discussed more detailed in

the next section. It should be noted, that relativistic effects are only significant close to the nucleus, where the kinetic energy is large. It is therefore reasonable to treat the interstitial region and the vacuum non-relativistically. Thus, merely within the muffin-tins the electrons are treated relativistically. And only the large component of Ψ is matched to the non-relativistic wavefunctions at the boundary between the muffin-tins and the interstitial region, because the small component is already negligible at this distance from the nucleus. The small component is attached to the large component, and cannot be varied independently. However, this is a sensible approximation for two reasons: Firstly even inside the muffin-tin sphere the large component is still much bigger than the small component, and plays the more important role, and secondly the two components are determined by solving the scalar relativistic equations for the spherically averaged potential. Therefore, they are very well suited to describe the wavefunctions.

Hence, the size of the basis set and the Hamiltonian matrix remains the same as in non-relativistic calculations, but the problem has to be solved twice, once for each direction of spin. This amounts to a numerical effort, that is equal to that needed in spin-polarized non-relativistic calculations.

3.2.2 The Scalar Relativistic Approximation

As I pointed out in the previous section, the electrons are only treated relativistically inside the muffin-tin spheres. Thus, the first problem that has to be addressed is the construction of the relativistic radial function. This is done by solving the scalar relativistic equation, including only the spherically averaged part of the potential. The starting point is the following Dirac equation.

$$\{c\boldsymbol{\alpha} \cdot \mathbf{p} + (\beta - 1)mc^2 + V(r)\} \Psi = E\Psi \quad (3.31)$$

The solution of (3.31) is discussed in many textbooks, e.g. E.M. Rose [Ros61]. Due to spin-orbit coupling m and m_s are not good quantum numbers any more, and they have to be replaced by the quantum numbers κ and μ (or j and μ), which are eigenvalues of the operators K and the z-component of the total angular momentum j_z (or the total angular momentum \mathbf{j} and j_z) respectively. K is defined by

$$K = \beta(\boldsymbol{\sigma} \cdot \mathbf{l} + 1) \quad (3.32)$$

The solutions of (3.31) have the form

$$\Psi = \Psi_{\kappa\mu} = \begin{pmatrix} g_{\kappa}(r)\chi_{\kappa\mu} \\ if_{\kappa}(r)\chi_{-\kappa\mu} \end{pmatrix} \quad (3.33)$$

Where $g_{\kappa}(r)$ is the large component, $f_{\kappa}(r)$ is the small component, $\chi_{\kappa\mu}$ and $\chi_{-\kappa\mu}$ are spin angular functions, which are eigenfunctions of \mathbf{j} , j_z , K and \mathbf{s}^2 with eigenvalues j , μ , κ ($-\kappa$) and $s = 1/2$ respectively. The spin angular functions can be expanded into

a sum of products of spherical harmonics and Pauli spinors. Where the expansion coefficients are the Clebsch-Gordon coefficients. The radial functions have to satisfy the following set of coupled equations.

$$\frac{\partial}{\partial r} g_\kappa(r) = -\frac{\kappa+1}{r} g_\kappa(r) + 2Mc f_\kappa(r) \quad (3.34)$$

$$\frac{\partial}{\partial r} f_\kappa(r) = \frac{1}{c}(V(r) - E)g_\kappa(r) + \frac{\kappa-1}{r} f_\kappa(r) \quad (3.35)$$

with

$$M = m + \frac{1}{2c^2}(E - V(r)) \quad (3.36)$$

This can be written in matrix form.

$$\begin{pmatrix} -\frac{\kappa+1}{r} - \frac{\partial}{\partial r} & 2Mc \\ \frac{1}{c}(V(r) - E) & \frac{\kappa-1}{r} - \frac{\partial}{\partial r} \end{pmatrix} \begin{pmatrix} g_\kappa(r) \\ f_\kappa(r) \end{pmatrix} = 0 \quad (3.37)$$

To derive the scalar relativistic approximation D.D. Koelling and B.N. Harmon [KH77] introduce the following transformation.

$$\begin{pmatrix} g_\kappa(r) \\ \phi_\kappa(r) \end{pmatrix} = \begin{pmatrix} 1 & 0 \\ \frac{1}{2Mc} \frac{\kappa+1}{r} & 1 \end{pmatrix} \begin{pmatrix} g_\kappa(r) \\ f_\kappa(r) \end{pmatrix} \quad (3.38)$$

Using this transformation (3.37) becomes

$$\begin{pmatrix} -\frac{\partial}{\partial r} & 2Mc \\ \frac{1}{2Mc} \frac{\kappa(\kappa+1)}{r^2} + \frac{1}{c}(V(r) - E) - \frac{1}{2Mc} \frac{\kappa+1}{r} \left(\frac{\partial}{\partial r} - \frac{M'}{M} \right) & \frac{\kappa-1}{r} - \frac{\partial}{\partial r} \end{pmatrix} \begin{pmatrix} g_\kappa(r) \\ \phi_\kappa(r) \end{pmatrix} = 0 \quad (3.39)$$

Where M' denotes the derivative of M with respect to r ($\partial M/\partial r$). Multiplying the first line in (3.39) by $(\kappa+1)/2Mc r$ and subtracting it from the second yields

$$\begin{pmatrix} -\frac{\partial}{\partial r} & 2Mc \\ \frac{1}{2Mc} \frac{l(l+1)}{r^2} + \frac{1}{c}(V(r) - E) + \frac{\kappa+1}{r} \frac{M'}{2M^2 c} & -\frac{2}{r} - \frac{\partial}{\partial r} \end{pmatrix} \begin{pmatrix} g_\kappa(r) \\ \phi_\kappa(r) \end{pmatrix} = 0 \quad (3.40)$$

Where the identity $\kappa(\kappa+1) = l(l+1)$ has been used. Recalling, that κ is the eigenvalue of $K = \beta(\boldsymbol{\sigma} \cdot \mathbf{l} + 1)$ the term $(\kappa+1)M'/2M^2 c$ can be identified as the spin-orbit

term. This term is dropped in the scalar relativistic approximation, because it is the only one, that causes coupling of spin up and spin down contributions. In the original paper this is interpreted as an average over all states for the two possible values of κ , $\kappa = l$, ($j = l - 1/2$) and $\kappa = -(l + 1)$, ($j = l + 1/2$). The radial functions $g_l(r)$ and $\phi_l(r)$ (the index κ has been replaced by l) can now be calculated from the following set of differential equations.

$$\frac{\partial}{\partial r} g_l(r) = 2Mc\phi_l(r) \quad (3.41)$$

$$\frac{\partial}{\partial r} \phi_l(r) = \left(\frac{1}{2Mc} \frac{l(l+1)}{r^2} + \frac{1}{c}(V(r) - E) \right) g_l(r) - \frac{2}{r} \phi_l(r) \quad (3.42)$$

Deriving these equations with respect to the energy yields a set of equations for $\dot{g}_l(r)$ and $\dot{\phi}_l(r)$, which are the relativistic analog of $\dot{u}_l(r)$.

$$\frac{\partial}{\partial r} \dot{g}_l(r) = 2Mc\dot{\phi}_l(r) + 2\dot{M}c\phi_l(r) \quad (3.43)$$

$$\begin{aligned} \frac{\partial}{\partial r} \dot{\phi}_l(r) &= \left(\frac{1}{2Mc} \frac{l(l+1)}{r^2} + \frac{1}{c}(V(r) - E) \right) \dot{g}_l(r) \\ &\quad - \left(\frac{\dot{M}}{2M^2c} \frac{l(l+1)}{r^2} + \frac{1}{c} \right) g_l(r) - \frac{2}{r} \dot{\phi}_l(r) \end{aligned} \quad (3.44)$$

For numerical reasons the functions $g_l(r)$ and $\phi_l(r)$ are replaced by $p(r) = rg_l(r)$ and $q(r) = cr\phi_l(r)$. Thus, equations (3.41) – (3.44) become

$$\frac{\partial}{\partial r} p(r) = 2 \left(1 + \frac{1}{2c^2}(E - V(r)) \right) q(r) + \frac{p(r)}{r} \quad (3.45)$$

$$\frac{\partial}{\partial r} q(r) = \left(\frac{l(l+1)}{2 \left(1 + \frac{1}{2c^2}(E - V(r)) \right) r^2} + V(r) - E \right) p(r) - \frac{q(r)}{r} \quad (3.46)$$

$$\frac{\partial}{\partial r} \dot{p}(r) = 2 \left(\left(1 + \frac{1}{2c^2}(E - V(r)) \right) \dot{q}(r) + \frac{1}{2c^2}q(r) \right) + \frac{\dot{p}(r)}{r} \quad (3.47)$$

$$\begin{aligned} \frac{\partial}{\partial r} \dot{q}(r) &= \left(\frac{l(l+1)}{2 \left(1 + \frac{1}{2c^2}(E - V(r)) \right) r^2} + V(r) - E \right) \dot{p}(r) \\ &\quad - \left(\frac{l(l+1)}{4c^2 \left(1 + \frac{1}{2c^2}(E - V(r)) \right) r^2} + 1 \right) p(r) - \frac{\dot{q}(r)}{r} \end{aligned} \quad (3.48)$$

This formulae have been obtained using the definition of M (3.36), $\dot{M} = 1/2c^2$ and the fact that $m = 1$ in Hartree units. In our implementation of FLAPW the radial wavefunctions are normalized according to

$$\left\langle \begin{pmatrix} g_l \\ \phi_l \end{pmatrix} \middle| \begin{pmatrix} g_l \\ \phi_l \end{pmatrix} \right\rangle = \int_0^{R_{MT}} (g_l^2(r) + \phi_l^2(r)) r^2 dr = 1 \quad (3.49)$$

However, $g_l^2(r) + \phi_l^2(r)$ is not the charge density. The radial charge density is defined by

$$\rho_l(r) = \left\langle \begin{pmatrix} g_l \\ f_l \end{pmatrix} \middle| \begin{pmatrix} g_l \\ f_l \end{pmatrix} \right\rangle = \int_0^{R_{MT}} (g_l^2(r) + f_l^2(r)) r^2 dr \quad (3.50)$$

The energy derivatives of the radial functions have to be made orthogonal to the radial functions (comp. section(3.1.2)).

$$\left\langle \begin{pmatrix} g_l \\ \phi_l \end{pmatrix} \middle| \begin{pmatrix} \dot{g}_l \\ \dot{\phi}_l \end{pmatrix} \right\rangle = 0 \quad (3.51)$$

Thus, the scalar relativistic FLAPW basis set is

$$\varphi_{\mathbf{G}_{\parallel} \mathbf{G}_{\perp}}(\mathbf{r}) = \begin{cases} \frac{1}{\sqrt{\Omega}} e^{i(\mathbf{G}_{\parallel} + \mathbf{k}_{\parallel})\mathbf{r}_{\parallel}} e^{i\mathbf{G}_{\perp}z} & Int. \\ \{A_{\mathbf{G}_{\parallel} \mathbf{G}_{\perp}} u_{\mathbf{G}_{\parallel}}(z) + B_{\mathbf{G}_{\parallel} \mathbf{G}_{\perp}} \dot{u}_{\mathbf{G}_{\parallel}}(z)\} e^{i(\mathbf{G}_{\parallel} + \mathbf{k}_{\parallel})\mathbf{r}_{\parallel}} & Vac. \\ \sum_{lm}^{\alpha} A_{lm}^{\alpha \mathbf{G} \mathbf{k}} \begin{pmatrix} g_l(r) \\ \phi_l(r) \end{pmatrix} Y_{lm}(\hat{\mathbf{r}}) + B_{lm}^{\alpha \mathbf{G} \mathbf{k}} \begin{pmatrix} \dot{g}_l(r) \\ \dot{\phi}_l(r) \end{pmatrix} Y_{lm}(\hat{\mathbf{r}}) & MT \end{cases} \quad (3.52)$$

Note, that the Pauli-spinors have been omitted, since the spin up and down problems are solved independently within the scalar relativistic approximation. Rewriting (3.40)

$$\mathcal{H}_{SP} \begin{pmatrix} g_l(r) \\ \phi_l(r) \end{pmatrix} = E \begin{pmatrix} g_l(r) \\ \phi_l(r) \end{pmatrix} \quad (3.53)$$

with

$$\mathcal{H}_{SP} = \begin{pmatrix} \frac{1}{2M} \frac{l(l+1)}{r^2} + V(r) & -\frac{2c}{r} - c \frac{\partial}{\partial r} \\ c \frac{\partial}{\partial r} & -2mc^2 + V(r) \end{pmatrix} \quad (3.54)$$

a matrix expression for the scalar relativistic Hamiltonian including only the spherically averaged part of the potential can be obtained.

3.3 Construction of the Hamiltonian Matrix

The FLAPW Hamiltonian and overlap matrices consist of three contributions from the three regions into which space is divided.

$$\mathbf{H} = \mathbf{H}_I + \mathbf{H}_{MT} + \mathbf{H}_V \quad (3.55)$$

$$\mathbf{S} = \mathbf{S}_I + \mathbf{S}_{MT} + \mathbf{S}_V \quad (3.56)$$

All three contributions have to be computed separately. Let's begin with the muffin-tin spheres.

3.3.1 Contribution of the Muffin-Tins

The contribution of the muffin-tin to the Hamiltonian matrix and the overlap matrix is given by:

$$H_{MT}^{\mathbf{G}'\mathbf{G}}(\mathbf{k}) = \sum_{\mu} \int_{MT^{\mu}} \left(\sum_{L'} A_{L'}^{\mu\mathbf{G}'}(\mathbf{k}) \varphi_{L'}^{\alpha}(\mathbf{r}) + B_{L'}^{\mu\mathbf{G}'}(\mathbf{k}) \dot{\varphi}_{L'}^{\alpha}(\mathbf{r}) \right)^* \mathcal{H}_{MT^{\alpha}} \left(\sum_L A_L^{\mu\mathbf{G}}(\mathbf{k}) \varphi_L^{\alpha}(\mathbf{r}) + B_L^{\mu\mathbf{G}}(\mathbf{k}) \dot{\varphi}_L^{\alpha}(\mathbf{r}) \right) d^3r \quad (3.57)$$

$$S_{MT}^{\mathbf{G}'\mathbf{G}}(\mathbf{k}) = \sum_{\mu} \int_{MT^{\mu}} \left(\sum_{L'} A_{L'}^{\mu\mathbf{G}'}(\mathbf{k}) \varphi_{L'}^{\alpha}(\mathbf{r}) + B_{L'}^{\mu\mathbf{G}'}(\mathbf{k}) \dot{\varphi}_{L'}^{\alpha}(\mathbf{r}) \right)^* \left(\sum_L A_L^{\mu\mathbf{G}}(\mathbf{k}) \varphi_L^{\alpha}(\mathbf{r}) + B_L^{\mu\mathbf{G}}(\mathbf{k}) \dot{\varphi}_L^{\alpha}(\mathbf{r}) \right) d^3r \quad (3.58)$$

with

$$\varphi_L^{\alpha}(\mathbf{r}) = \begin{pmatrix} g_l(r) \\ \phi_l(r) \end{pmatrix} Y_L(\hat{\mathbf{r}}), \quad \dot{\varphi}_L^{\alpha}(\mathbf{r}) = \begin{pmatrix} \dot{g}_l(r) \\ \dot{\phi}_l(r) \end{pmatrix} Y_L(\hat{\mathbf{r}}) \quad (3.59)$$

Where we distinguish between the atom index μ and the atom type index $\alpha(\mu)$. In most application the are symmetry equivalent atom in the unit cell, i.e. some atoms can be mapped onto each other by space group operations. Clearly, these atom must possess the same physical properties, e.g. the potential has to be equal. As a consequence, the Hamiltonian and the basis functions $\varphi_L^{\alpha}(\mathbf{r})$ do not differ among the atoms of the same type. This fact is exploited in that the muffin-tin potential of an atom type is only stored once for the representative atom, and the matrices 3.61–3.64 is also calculated for the representative only. $\mathcal{H}_{MT^{\alpha}}$ is the scalar relativistic Hamiltonian operator. It can be split up into two parts, the spherical Hamiltonian \mathcal{H}_{sp} (3.54) and the nonspherical contributions to the potential V_{ns} .

$$\mathcal{H}_{MT^{\alpha}} = \mathcal{H}_{sp}^{\alpha} + V_{ns}^{\alpha} \quad (3.60)$$

The above integrations contain the following matrix elements.

$$t_{L'L}^{\alpha\varphi\varphi} = \int_{MT^{\alpha}} \varphi_{L'}^{\alpha}(\mathbf{r}) \mathcal{H}_{MT^{\alpha}} \varphi_L^{\alpha}(\mathbf{r}) d^3r \quad (3.61)$$

$$t_{L'L}^{\alpha\varphi\dot{\varphi}} = \int_{MT^{\alpha}} \varphi_{L'}^{\alpha}(\mathbf{r}) \mathcal{H}_{MT^{\alpha}} \dot{\varphi}_L^{\alpha}(\mathbf{r}) d^3r \quad (3.62)$$

$$t_{L'L}^{\alpha\dot{\varphi}\varphi} = \int_{MT^{\alpha}} \dot{\varphi}_{L'}^{\alpha}(\mathbf{r}) \mathcal{H}_{MT^{\alpha}} \varphi_L^{\alpha}(\mathbf{r}) d^3r \quad (3.63)$$

$$t_{L'L}^{\alpha\dot{\varphi}\dot{\varphi}} = \int_{MT^{\alpha}} \dot{\varphi}_{L'}^{\alpha}(\mathbf{r}) \mathcal{H}_{MT^{\alpha}} \dot{\varphi}_L^{\alpha}(\mathbf{r}) d^3r \quad (3.64)$$

These matrix elements do not depend on the $A_L^{\mu\mathbf{G}}(\mathbf{k})$ and $B_L^{\mu\mathbf{G}}(\mathbf{k})$ coefficients. Thus, they are independent of the Bloch vector and need to be calculated only once per

iteration. The functions φ_L^α and $\dot{\varphi}_L^\alpha$ have been constructed to diagonalize the spherical part \mathcal{H}_{sp}^α of the muffin-tin Hamiltonian \mathcal{H}_{MT}^α .

$$\mathcal{H}_{sp}^\alpha \varphi_L^\alpha = E_l \varphi_L^\alpha \quad (3.65)$$

$$\mathcal{H}_{sp}^\alpha \dot{\varphi}_L^\alpha + \dot{\mathcal{H}}_{sp}^\alpha \varphi_L^\alpha = E_l \dot{\varphi}_L^\alpha + \varphi_L^\alpha \quad (3.66)$$

However, $\dot{\mathcal{H}}_{sp}^\alpha$ is smaller than \mathcal{H}_{sp}^α , by a factor of $1/c^2$ and is therefore neglected.

$$\mathcal{H}_{sp}^\alpha \dot{\varphi}_L^\alpha = E_l \dot{\varphi}_L^\alpha + \varphi_L^\alpha \quad (3.67)$$

Multiplying these equations with $\varphi_{L'}^\alpha(\mathbf{r})$ and $\dot{\varphi}_{L'}^\alpha(\mathbf{r})$ respectively and integrating over the muffin-tins gives

$$\langle \varphi_{L'}^\alpha | \mathcal{H}_{sp}^\alpha \varphi_L^\alpha \rangle_{MT} = \delta_{ll'} \delta_{mm'} E_l \quad (3.68)$$

$$\langle \varphi_{L'}^\alpha | \mathcal{H}_{sp}^\alpha \dot{\varphi}_L^\alpha \rangle_{MT} = \delta_{ll'} \delta_{mm'} \quad (3.69)$$

$$\langle \dot{\varphi}_{L'}^\alpha | \mathcal{H}_{sp}^\alpha \varphi_L^\alpha \rangle_{MT} = 0 \quad (3.70)$$

$$\langle \dot{\varphi}_{L'}^\alpha | \mathcal{H}_{sp}^\alpha \dot{\varphi}_L^\alpha \rangle_{MT} = \delta_{ll'} \delta_{mm'} E_l \langle \dot{\varphi}_L^\alpha | \dot{\varphi}_L^\alpha \rangle_{MT} \quad (3.71)$$

Where the normalization condition for φ_L^α has been used. So, only the expectation values of the nonspherical part of the potential are left to be determined. Since the potential is also expanded into a product of radial functions and spherical harmonics, the corresponding integrals consist of product of a radial integrals and an angular integrals over three spherical harmonics, the so-called gaunt coefficients.

$$V^\alpha(\mathbf{r}) = \sum_{L'} V_{L'}^\alpha(r) Y_{L'}(\hat{\mathbf{r}}) \quad (3.72)$$

$$t_{L'L}^{\alpha\varphi\varphi} = \sum_{l''} I_{l'l''}^{\alpha\varphi\varphi} G_{l'l''}^{m'mm''} + \delta_{ll'} \delta_{mm'} E_l \quad (3.73)$$

$$t_{L'L}^{\alpha\varphi\dot{\varphi}} = \sum_{l''} I_{l'l''}^{\alpha\varphi\dot{\varphi}} G_{l'l''}^{m'mm''} + \delta_{ll'} \delta_{mm'} \quad (3.74)$$

$$t_{L'L}^{\alpha\dot{\varphi}\varphi} = \sum_{l''} I_{l'l''}^{\alpha\dot{\varphi}\varphi} G_{l'l''}^{m'mm''} \quad (3.75)$$

$$t_{L'L}^{\alpha\dot{\varphi}\dot{\varphi}} = \sum_{l''} I_{l'l''}^{\alpha\dot{\varphi}\dot{\varphi}} G_{l'l''}^{m'mm''} + \delta_{ll'} \delta_{mm'} E_l \langle \dot{\varphi}_{lm}^\alpha | \dot{\varphi}_{lm}^\alpha \rangle_{MT} \quad (3.76)$$

with

$$I_{l'l''}^{\alpha\varphi\varphi} = \int (g_l^\alpha(r) g_{l''}^\alpha(r) + \phi_l^\alpha(r) \phi_{l''}^\alpha(r)) V_{l''}^\alpha(r) r^2 dr \quad (3.77)$$

$$I_{l'l''}^{\alpha\varphi\dot{\varphi}} = \int (g_l^\alpha(r) \dot{g}_{l''}^\alpha(r) + \phi_l^\alpha(r) \dot{\phi}_{l''}^\alpha(r)) V_{l''}^\alpha(r) r^2 dr \quad (3.78)$$

$$I_{l'l''}^{\alpha\dot{\varphi}\varphi} = \int (\dot{g}_l^\alpha(r) g_{l''}^\alpha(r) + \dot{\phi}_l^\alpha(r) \phi_{l''}^\alpha(r)) V_{l''}^\alpha(r) r^2 dr \quad (3.79)$$

$$I_{l'l''}^{\alpha\dot{\varphi}\dot{\varphi}} = \int (\dot{g}_l^\alpha(r) \dot{g}_{l''}^\alpha(r) + \dot{\phi}_l^\alpha(r) \dot{\phi}_{l''}^\alpha(r)) V_{l''}^\alpha(r) r^2 dr \quad (3.80)$$

and

$$G_{l'l''}^{mm'm''} = \int Y_{lm}^* Y_{l'm'} Y_{l''m''} d\Omega \quad (3.81)$$

The I matrices contain the radial integrals. Finally, the Hamiltonian and overlap matrix elements become

$$\begin{aligned} H_{MT}^{\mathbf{G}'\mathbf{G}}(\mathbf{k}) &= \sum_{\mu} \sum_{L'L} (A_{L'}^{\mu\mathbf{G}'}(\mathbf{k}))^* t_{L'L}^{\alpha\varphi\varphi} A_L^{\mu\mathbf{G}}(\mathbf{k}) + (B_{L'}^{\mu\mathbf{G}'}(\mathbf{k}))^* t_{L'L}^{\alpha\dot{\varphi}\dot{\varphi}} B_L^{\mu\mathbf{G}}(\mathbf{k}) \\ &+ (A_{L'}^{\mu\mathbf{G}'}(\mathbf{k}))^* t_{L'L}^{\alpha\varphi\dot{\varphi}} B_L^{\mu\mathbf{G}}(\mathbf{k}) + (B_{L'}^{\mu\mathbf{G}'}(\mathbf{k}))^* t_{L'L}^{\alpha\dot{\varphi}\varphi} A_L^{\mu\mathbf{G}}(\mathbf{k}) \end{aligned} \quad (3.82)$$

$$S_{MT}^{\mathbf{G}'\mathbf{G}}(\mathbf{k}) = \sum_{\mu} \sum_L (A_L^{\mu\mathbf{G}'}(\mathbf{k}))^* A_L^{\mu\mathbf{G}}(\mathbf{k}) + (B_L^{\mu\mathbf{G}'}(\mathbf{k}))^* B_L^{\mu\mathbf{G}}(\mathbf{k}) \langle \dot{\varphi}_L^{\alpha} | \dot{\varphi}_L^{\alpha} \rangle_{MT\mu} \quad (3.83)$$

3.3.2 The Vacuum Contribution

The vacuum contributions to the Hamiltonian and overlap matrix are.

$$\begin{aligned} H_V^{\mathbf{G}'\mathbf{G}}(\mathbf{k}_{\parallel}) &= \int_V \left(\{ A_{\mathbf{G}'_{\parallel}\mathbf{G}'_{\perp}}(\mathbf{k}_{\parallel}) u_{\mathbf{G}'_{\parallel}}(\mathbf{k}_{\parallel}, z) + B_{\mathbf{G}'_{\parallel}\mathbf{G}'_{\perp}}(\mathbf{k}_{\parallel}) \dot{u}_{\mathbf{G}'_{\parallel}}(\mathbf{k}_{\parallel}, z) \} e^{i(\mathbf{G}'_{\parallel} + \mathbf{k}_{\parallel})\mathbf{r}_{\parallel}} \right)^* \\ &\mathcal{H}_V \left(\{ A_{\mathbf{G}_{\parallel}\mathbf{G}_{\perp}}(\mathbf{k}_{\parallel}) u_{\mathbf{G}_{\parallel}}(\mathbf{k}_{\parallel}, z) + B_{\mathbf{G}_{\parallel}\mathbf{G}_{\perp}}(\mathbf{k}_{\parallel}) \dot{u}_{\mathbf{G}_{\parallel}}(\mathbf{k}_{\parallel}, z) \} e^{i(\mathbf{G}_{\parallel} + \mathbf{k}_{\parallel})\mathbf{r}_{\parallel}} \right) d^3r \\ S_V^{\mathbf{G}'\mathbf{G}}(\mathbf{k}_{\parallel}) &= \int_V \left(\{ A_{\mathbf{G}'_{\parallel}\mathbf{G}'_{\perp}}(\mathbf{k}_{\parallel}) u_{\mathbf{G}'_{\parallel}}(\mathbf{k}_{\parallel}, z) + B_{\mathbf{G}'_{\parallel}\mathbf{G}'_{\perp}}(\mathbf{k}_{\parallel}) \dot{u}_{\mathbf{G}'_{\parallel}}(\mathbf{k}_{\parallel}, z) \} e^{i(\mathbf{G}'_{\parallel} + \mathbf{k}_{\parallel})\mathbf{r}_{\parallel}} \right)^* \\ &\left(\{ A_{\mathbf{G}_{\parallel}\mathbf{G}_{\perp}}(\mathbf{k}_{\parallel}) u_{\mathbf{G}_{\parallel}}(\mathbf{k}_{\parallel}, z) + B_{\mathbf{G}_{\parallel}\mathbf{G}_{\perp}}(\mathbf{k}_{\parallel}) \dot{u}_{\mathbf{G}_{\parallel}}(\mathbf{k}_{\parallel}, z) \} e^{i(\mathbf{G}_{\parallel} + \mathbf{k}_{\parallel})\mathbf{r}_{\parallel}} \right) d^3r \end{aligned} \quad (3.84)$$

The treatment of the vacuum region in FLAPW is in many way similar to the treatment of the muffin-tins. As in the muffin-tins the basis functions are constructed to diagonalize only a certain part of the Hamiltonian. Here this part of the Hamiltonian includes only the non-corrugated planar averaged part of the potential ($V_{nc}(z)$), that depends only on z .

$$\mathcal{H}_V = \mathcal{H}_{nc} + V_{co}(\mathbf{r}) \quad (3.85)$$

The t-matrices can be defined in the same way as inside the muffin-tin spheres ((3.61) – (3.64)).

$$t_{\mathbf{G}'_{\parallel}\mathbf{G}_{\parallel}}^{uu}(\mathbf{k}_{\parallel}) = \langle \varphi_{\mathbf{G}'_{\parallel}}(\mathbf{k}_{\parallel}) | \mathcal{H}_V \varphi_{\mathbf{G}_{\parallel}}(\mathbf{k}_{\parallel}) \rangle_V \quad (3.86)$$

$$t_{\mathbf{G}'_{\parallel}\mathbf{G}_{\parallel}}^{u\dot{u}}(\mathbf{k}_{\parallel}) = \langle \varphi_{\mathbf{G}'_{\parallel}}(\mathbf{k}_{\parallel}) | \mathcal{H}_V \dot{\varphi}_{\mathbf{G}_{\parallel}}(\mathbf{k}_{\parallel}) \rangle_V \quad (3.87)$$

$$t_{\mathbf{G}'_{\parallel}\mathbf{G}_{\parallel}}^{\dot{u}u}(\mathbf{k}_{\parallel}) = \langle \dot{\varphi}_{\mathbf{G}'_{\parallel}}(\mathbf{k}_{\parallel}) | \mathcal{H}_V \varphi_{\mathbf{G}_{\parallel}}(\mathbf{k}_{\parallel}) \rangle_V \quad (3.88)$$

$$t_{\mathbf{G}'_{\parallel}\mathbf{G}_{\parallel}}^{\dot{u}\dot{u}}(\mathbf{k}_{\parallel}) = \langle \dot{\varphi}_{\mathbf{G}'_{\parallel}}(\mathbf{k}_{\parallel}) | \mathcal{H}_V \dot{\varphi}_{\mathbf{G}_{\parallel}}(\mathbf{k}_{\parallel}) \rangle_V \quad (3.89)$$

The contribution to these matrices from \mathcal{H}_{nc} , are given by the analog of equations (3.68) – (3.71). The non-corrugated potential is expanded into z -dependent functions

and planewaves in the x-y-plane.

$$V_{co}(\mathbf{r}) = \sum_{\mathbf{G}''_{\parallel}} V_{\mathbf{G}''_{\parallel}}(z) e^{i\mathbf{G}''_{\parallel}\mathbf{r}} \quad (3.90)$$

The contribution due to the expectation values of $V_{CO}(\mathbf{r})$ consists of a z-dependent integral and an integral in the x-y-plane of the following form.

$$\int e^{-i\mathbf{G}'_{\parallel}\mathbf{r}} e^{i\mathbf{G}''_{\parallel}\mathbf{r}} e^{i\mathbf{G}_{\parallel}\mathbf{r}} dx dy = \delta_{\mathbf{G}'_{\parallel}(\mathbf{G}_{\parallel}+\mathbf{G}''_{\parallel})} \quad (3.91)$$

Thus, the t-matrices are given by

$$t_{\mathbf{G}'_{\parallel}\mathbf{G}_{\parallel}}^{uu}(\mathbf{k}_{\parallel}) = I_{\mathbf{G}'_{\parallel}\mathbf{G}_{\parallel}(\mathbf{G}'_{\parallel}-\mathbf{G}_{\parallel})}^{uu}(\mathbf{k}_{\parallel}) + \delta_{\mathbf{G}'_{\parallel}\mathbf{G}_{\parallel}} E_{vac} \quad (3.92)$$

$$t_{\mathbf{G}'_{\parallel}\mathbf{G}_{\parallel}}^{u\dot{u}}(\mathbf{k}_{\parallel}) = I_{\mathbf{G}'_{\parallel}\mathbf{G}_{\parallel}(\mathbf{G}'_{\parallel}-\mathbf{G}_{\parallel})}^{u\dot{u}}(\mathbf{k}_{\parallel}) + \delta_{\mathbf{G}'_{\parallel}\mathbf{G}_{\parallel}} \quad (3.93)$$

$$t_{\mathbf{G}'_{\parallel}\mathbf{G}_{\parallel}}^{\dot{u}u}(\mathbf{k}_{\parallel}) = I_{\mathbf{G}'_{\parallel}\mathbf{G}_{\parallel}(\mathbf{G}'_{\parallel}-\mathbf{G}_{\parallel})}^{\dot{u}u}(\mathbf{k}_{\parallel}) \quad (3.94)$$

$$t_{\mathbf{G}'_{\parallel}\mathbf{G}_{\parallel}}^{\dot{u}\dot{u}}(\mathbf{k}_{\parallel}) = I_{\mathbf{G}'_{\parallel}\mathbf{G}_{\parallel}(\mathbf{G}'_{\parallel}-\mathbf{G}_{\parallel})}^{\dot{u}\dot{u}}(\mathbf{k}_{\parallel}) + \delta_{\mathbf{G}'_{\parallel}\mathbf{G}_{\parallel}} E_{vac} \langle \dot{u}_{\mathbf{G}_{\parallel}}(\mathbf{k}_{\parallel}) | \dot{u}_{\mathbf{G}_{\parallel}}(\mathbf{k}_{\parallel}) \rangle_V \quad (3.95)$$

Where the I matrices abbreviate the z-dependent integrals including $V_{(\mathbf{G}'_{\parallel}-\mathbf{G}_{\parallel})}(z)$.

$$I_{\mathbf{G}'_{\parallel}\mathbf{G}_{\parallel}\mathbf{G}''_{\parallel}}^{uu}(\mathbf{k}_{\parallel}) = \int u_{\mathbf{G}'_{\parallel}}(\mathbf{k}_{\parallel}) u_{\mathbf{G}_{\parallel}}(\mathbf{k}_{\parallel}) V_{\mathbf{G}''_{\parallel}}(z) dz \quad (3.96)$$

$$I_{\mathbf{G}'_{\parallel}\mathbf{G}_{\parallel}\mathbf{G}''_{\parallel}}^{u\dot{u}}(\mathbf{k}_{\parallel}) = \int u_{\mathbf{G}'_{\parallel}}(\mathbf{k}_{\parallel}) \dot{u}_{\mathbf{G}_{\parallel}}(\mathbf{k}_{\parallel}) V_{\mathbf{G}''_{\parallel}}(z) dz \quad (3.97)$$

$$I_{\mathbf{G}'_{\parallel}\mathbf{G}_{\parallel}\mathbf{G}''_{\parallel}}^{\dot{u}u}(\mathbf{k}_{\parallel}) = \int \dot{u}_{\mathbf{G}'_{\parallel}}(\mathbf{k}_{\parallel}) u_{\mathbf{G}_{\parallel}}(\mathbf{k}_{\parallel}) V_{\mathbf{G}''_{\parallel}}(z) dz \quad (3.98)$$

$$I_{\mathbf{G}'_{\parallel}\mathbf{G}_{\parallel}\mathbf{G}''_{\parallel}}^{\dot{u}\dot{u}}(\mathbf{k}_{\parallel}) = \int \dot{u}_{\mathbf{G}'_{\parallel}}(\mathbf{k}_{\parallel}) \dot{u}_{\mathbf{G}_{\parallel}}(\mathbf{k}_{\parallel}) V_{\mathbf{G}''_{\parallel}}(z) dz \quad (3.99)$$

The Hamiltonian and overlap matrix elements are calculated according to

$$\begin{aligned} H_V^{\mathbf{G}'\mathbf{G}}(\mathbf{k}_{\parallel}) &= (A_{\mathbf{G}'_{\parallel}\mathbf{G}'_{\perp}}(\mathbf{k}_{\parallel}))^* t_{\mathbf{G}'_{\parallel}\mathbf{G}_{\parallel}}^{uu}(\mathbf{k}_{\parallel}) A_{\mathbf{G}_{\parallel}\mathbf{G}_{\perp}}(\mathbf{k}_{\parallel}) \\ &\quad + (A_{\mathbf{G}'_{\parallel}\mathbf{G}'_{\perp}}(\mathbf{k}_{\parallel}))^* t_{\mathbf{G}'_{\parallel}\mathbf{G}_{\parallel}}^{u\dot{u}}(\mathbf{k}_{\parallel}) B_{\mathbf{G}_{\parallel}\mathbf{G}_{\perp}}(\mathbf{k}_{\parallel}) \\ &\quad + (B_{\mathbf{G}'_{\parallel}\mathbf{G}'_{\perp}}(\mathbf{k}_{\parallel}))^* t_{\mathbf{G}'_{\parallel}\mathbf{G}_{\parallel}}^{\dot{u}u}(\mathbf{k}_{\parallel}) A_{\mathbf{G}_{\parallel}\mathbf{G}_{\perp}}(\mathbf{k}_{\parallel}) \\ &\quad + (B_{\mathbf{G}'_{\parallel}\mathbf{G}'_{\perp}}(\mathbf{k}_{\parallel}))^* t_{\mathbf{G}'_{\parallel}\mathbf{G}_{\parallel}}^{\dot{u}\dot{u}}(\mathbf{k}_{\parallel}) B_{\mathbf{G}_{\parallel}\mathbf{G}_{\perp}}(\mathbf{k}_{\parallel}) \end{aligned} \quad (3.100)$$

$$\begin{aligned} S_V^{\mathbf{G}'\mathbf{G}}(\mathbf{k}_{\parallel}) &= (A_{\mathbf{G}'_{\parallel}\mathbf{G}'_{\perp}}(\mathbf{k}_{\parallel}))^* A_{\mathbf{G}_{\parallel}\mathbf{G}_{\perp}}(\mathbf{k}_{\parallel}) \delta_{\mathbf{G}'_{\parallel}\mathbf{G}_{\parallel}} \\ &\quad + (B_{\mathbf{G}'_{\parallel}\mathbf{G}'_{\perp}}(\mathbf{k}_{\parallel}))^* B_{\mathbf{G}_{\parallel}\mathbf{G}_{\perp}}(\mathbf{k}_{\parallel}) \langle \dot{u}_{\mathbf{G}_{\parallel}}(\mathbf{k}_{\parallel}) | \dot{u}_{\mathbf{G}_{\parallel}}(\mathbf{k}_{\parallel}) \rangle_V \delta_{\mathbf{G}'_{\parallel}\mathbf{G}_{\parallel}} \end{aligned} \quad (3.101)$$

3.3.3 The Interstitial Contribution

The interstitial contributions to the Hamiltonian and overlap matrix have the following form.

$$H_I^{\mathbf{G}'\mathbf{G}}(\mathbf{k}) = \frac{1}{\Omega} \int_I e^{-i(\mathbf{G}+\mathbf{k})\mathbf{r}} \left(-\frac{\hbar^2}{2m} \Delta + V(\mathbf{r}) \right) e^{i(\mathbf{G}'+\mathbf{k})\mathbf{r}} d^3r \quad (3.102)$$

$$S_I^{\mathbf{G}\mathbf{G}'} = \frac{1}{\Omega} \int_I e^{-i(\mathbf{G}+\mathbf{k})\mathbf{r}} e^{i(\mathbf{G}'+\mathbf{k})\mathbf{r}} d^3r \quad (3.103)$$

The potential is also expanded into planewaves in the interstitial region.

$$V(\mathbf{r}) = \sum_{\mathbf{G}'} V_{\mathbf{G}'} e^{-i\mathbf{G}'\mathbf{r}} \quad (3.104)$$

Without the existence of the muffin-tin spheres the integration would stretch over the entire unit cell and the integration becomes rather simple. The kinetic energy is diagonal in momentum space and the potential is local, diagonal in real space and of convolution form in momentum space.

$$H_I^{\mathbf{G}\mathbf{G}'}(\mathbf{k}) = \frac{\hbar^2}{2m} |\mathbf{G} + \mathbf{k}|^2 \delta_{\mathbf{G}\mathbf{G}'} + V_{(\mathbf{G}-\mathbf{G}')}$$

$$S_I^{\mathbf{G}\mathbf{G}'} = \delta_{\mathbf{G}\mathbf{G}'}$$

However, these matrix elements are not as straightforward to calculate as they appear at first glance, because of the complicated structure of the interstitial region. The integrations have to be performed only in between the muffin-tins. Therefore, a step function $\Theta(\mathbf{r})$ has to be introduced, that cuts out the muffin-tins.

$$\Theta(\mathbf{r}) = \begin{cases} 1 & \text{interstitial region} \\ 0 & \text{muffin-tins} \end{cases} \quad (3.105)$$

In film calculations the region between $D/2$ and $\tilde{D}/2$ has to be cut out too, but to keep it simple we will discuss the only the bulk case in this section. Using the step function the matrix elements can be written:

$$H_{INT}^{\mathbf{G}\mathbf{G}'}(\mathbf{k}) = \frac{1}{\Omega} \int_{cell} e^{-i(\mathbf{G}-\mathbf{G}')\mathbf{r}} V(\mathbf{r}) \Theta(\mathbf{r}) d^3r + \frac{1}{2} (\mathbf{G}' + \mathbf{k})^2 \frac{1}{\Omega} \int_{cell} e^{-i(\mathbf{G}-\mathbf{G}')\mathbf{r}} \Theta(\mathbf{r}) d^3r \quad (3.106)$$

$$S_{INT}^{\mathbf{G}\mathbf{G}'} = \frac{1}{\Omega} \int_{cell} e^{-i(\mathbf{G}-\mathbf{G}')\mathbf{r}} \Theta(\mathbf{r}) d^3r \quad (3.107)$$

In momentum space 3.106 becomes:

$$\Rightarrow H_{INT}^{\mathbf{G}\mathbf{G}'}(\mathbf{k}) = (V\Theta)_{(\mathbf{G}-\mathbf{G}')} + \frac{\hbar^2}{2m} (\mathbf{G}' + \mathbf{k})^2 \Theta_{(\mathbf{G}-\mathbf{G}')} \quad (3.108)$$

$$S_{INT}^{\mathbf{G}\mathbf{G}'} = \Theta_{(\mathbf{G}-\mathbf{G}')} \quad (3.109)$$

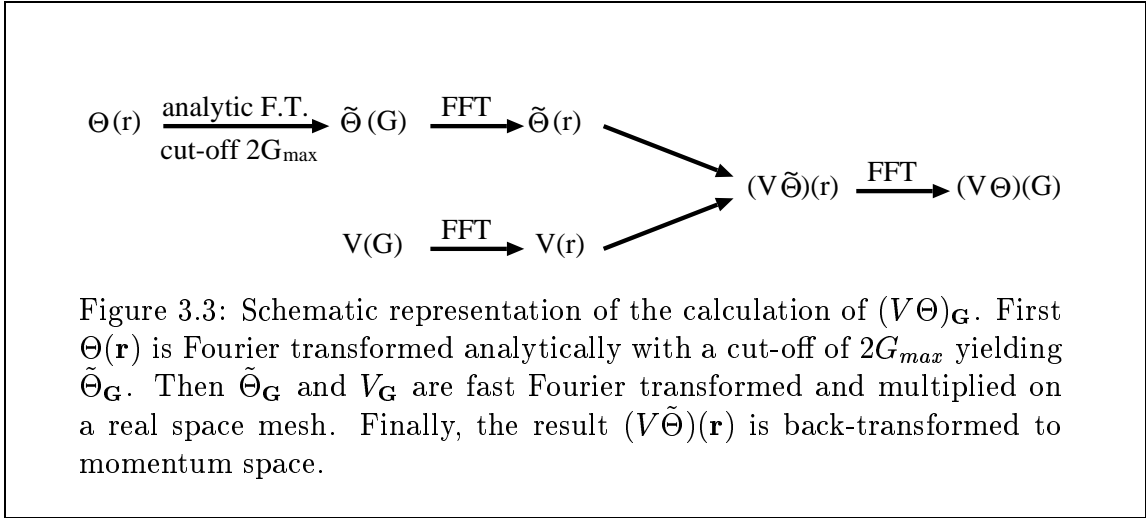
Where $\Theta_{\mathbf{G}}$ and $(V\Theta)_{\mathbf{G}}$ are the Fourier coefficients of $\Theta(\mathbf{r})$ and $V(\mathbf{r})\Theta(\mathbf{r})$ respectively. Apparently these coefficients are needed up to a cut-off of $2G_{max}$. The step function can be Fourier transformed analytically.

$$\Theta_{\mathbf{G}} = \delta_{\mathbf{G},\mathbf{0}} - \sum_{\alpha} e^{-i\mathbf{G}\boldsymbol{\tau}^{\alpha}} \frac{4\pi(R_{MT}^{\alpha})^3}{\Omega} \frac{j_1(GR_{MT}^{\alpha})}{GR_{MT}^{\alpha}}$$

The Fourier transform of the product of $V(\mathbf{r})$ and $\Theta(\mathbf{r})$ is given by a convolution in momentum space.

$$(V\Theta)_{\mathbf{G}} = \sum_{\mathbf{G}'} V_{\mathbf{G}'} \Theta_{(\mathbf{G}-\mathbf{G}')}$$

This convolution depends on both, \mathbf{G} and \mathbf{G}' , therefore the numerical effort increases like $(G_{max})^6$. However, $(V\Theta)_{\mathbf{G}}$ can be determined more efficiently, using Fast-Fourier-Transform (FFT). In fig. 3.3 it is shown schematically how $(V\Theta)_{\mathbf{G}}$ can be obtained using FFT. Using this scheme the numerical effort increases like $(G_{max})^3 \ln((G_{max})^3)$ with G_{max} .



3.3.4 The Muffin-Tin A- and B-Coefficients

Within FLAPW the electron wavefunctions are expanded differently in the interstitial region and the muffin-tins. Each basis function consists of a planewave in the interstitial, which is matched to the radial functions and spherical harmonics in the muffin-tins. The coefficients of the function inside the spheres are determined from the requirement, that the basis functions and their derivatives are continuous at the sphere boundaries. These coefficients play an important role, and they will be needed again during the discussion of the local orbitals in chapter 5. In this section we will therefore discuss how the matching conditions can be solved and what properties they induce.

In many systems that the FLAPW method can be applied to some atoms are symmetry equivalent, i.e. these atoms can be mapped onto each other by a space group operation $\{\mathbf{R}|\boldsymbol{\tau}\}$. Such a group of atoms is called an atom type, represented by one of the atoms. Let $\{\mathbf{R}^{\mu}|\boldsymbol{\tau}^{\mu}\}$ the operation that maps the atom μ onto its representative. This atom can now be assigned a local coordinate frame S^{μ} (cf. fig. 3.4), where the origin of S^{μ} is at the atoms position³ \mathbf{p}^{μ} . The local frame is

³The atom position is very frequently denoted by $\boldsymbol{\tau}^{\mu}$, which would clearly cause some confusion

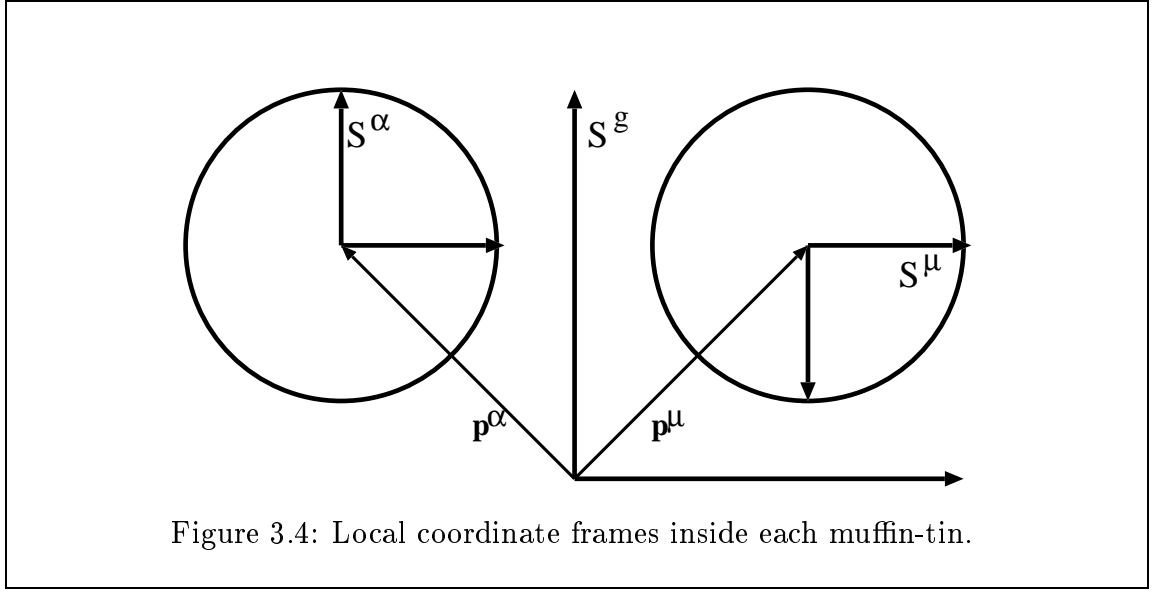


Figure 3.4: Local coordinate frames inside each muffin-tin.

chosen such that the unit vectors of the local frame S^μ are mapped onto those of the global frame by \mathbf{R}^g ($\mathbf{R}^\mu S^\mu = S^g$). The local frame of the representative atom S^α is only translated with respect to the global frame, i.e. the same rotation \mathbf{R}^μ maps S^μ onto S^α . The potential (and other quantities) inside the muffin-tins can now be written in terms of the local coordinate system. Due to the symmetry we find $V_{MT^\alpha}(\mathbf{r}^\alpha) = V_{MT^\mu}(\mathbf{r}^\mu)$, where \mathbf{r}^α and \mathbf{r}^μ are expanded in terms of the local frames S^α and S^μ respectively. As a consequence the radial functions⁴ $u_l(r)$ and the t-matrices are the same for all atoms of the same type. This way symmetry is exploited to save memory and computer time (during the calculation of the t-matrices).

Any plane wave can be expanded into spherical harmonics via the Rayleigh expansion.

$$e^{i\mathbf{K}\mathbf{r}} = 4\pi \sum_L i^l j_l(rK) Y_L^*(\hat{\mathbf{K}}) Y_L(\hat{\mathbf{r}}) \quad (3.110)$$

Where $r = |\mathbf{r}|$, $K = |\mathbf{K}|$ and \mathbf{K} abbreviates $(\mathbf{G} + \mathbf{k})$. Looked at from the local frame \mathbf{K} and \mathbf{p}^μ appear rotated, besides the origin of the local frame is shifted. Therefore, the plane wave has the following form in the local frame:

$$e^{i(\mathbf{R}^\mu \mathbf{K})(\mathbf{r} + \mathbf{R}^\mu \mathbf{p}^\mu)} \quad (3.111)$$

Thus, the Rayleigh expansion of the plane wave in the local frame is given by:

$$e^{i\mathbf{K}\mathbf{p}^\mu} 4\pi \sum_L i^l j_l(rK) Y_L^*(\mathbf{R}^\mu \hat{\mathbf{K}}) Y_L(\hat{\mathbf{r}}) \quad (3.112)$$

in this context.

⁴Within this section the radial functions are denoted by $u_l(r)$ for simplicity, though in scalar relativistic calculating the large component $g_l(r)$ is used instead of $u_l(r)$.

The requirement of continuity of the wavefunctions at the sphere boundary leads to the equation:

$$\begin{aligned} & \sum_L A_L^{\mu\mathbf{G}}(\mathbf{k}) u_l(R_{MT^\alpha}) Y_L(\hat{\mathbf{r}}) + B_L^{\mu\mathbf{G}}(\mathbf{k}) \dot{u}_l(R_{MT^\alpha}) Y_L(\hat{\mathbf{r}}) \\ &= e^{i\mathbf{K}\mathbf{p}^\mu} 4\pi \sum_L i^l j_l(rK) Y_L^*(\mathbf{R}^\mu \hat{\mathbf{K}}) Y_L(\hat{\mathbf{r}}) \end{aligned} \quad (3.113)$$

Where R_{MT^α} is the muffin-tin radius of the atom type α . The second requirement is, that the derivative with respect to r , denoted by $\partial/\partial r = '$, is also continuous.

$$\begin{aligned} & \sum_L A_L^{\mu\mathbf{G}}(\mathbf{k}) u_l'(R_{MT^\alpha}) Y_L(\hat{\mathbf{r}}) + B_L^{\mu\mathbf{G}}(\mathbf{k}) \dot{u}_l'(R_{MT^\alpha}) Y_L(\hat{\mathbf{r}}) \\ &= e^{i\mathbf{K}\mathbf{p}^\mu} 4\pi \sum_L i^l K j_l'(rK) Y_L^*(\mathbf{R}^\mu \hat{\mathbf{K}}) Y_L(\hat{\mathbf{r}}) \end{aligned} \quad (3.114)$$

These conditions can only be satisfied, if the coefficients of each spherical harmonic $Y_L(\hat{\mathbf{r}})$ are equal. Solving the resulting equations for $A_L^{\mu\mathbf{G}}(\mathbf{k})$ and $B_L^{\mu\mathbf{G}}(\mathbf{k})$ yields:

$$\begin{aligned} A_L^{\mu\mathbf{G}}(\mathbf{k}) &= e^{i\mathbf{K}\mathbf{p}^\mu} 4\pi \frac{1}{W} i^l Y_L^*(\mathbf{R}^\mu \hat{\mathbf{K}}) \\ & \quad [\dot{u}_l(R_{MT^\alpha}) K j_l'(R_{MT^\alpha} K) - \dot{u}_l'(R_{MT^\alpha}) j_l(R_{MT^\alpha} K)] \\ B_L^{\mu\mathbf{G}}(\mathbf{k}) &= e^{i\mathbf{K}\mathbf{p}^\mu} 4\pi \frac{1}{W} i^l Y_L^*(\mathbf{R}^\mu \hat{\mathbf{K}}) \\ & \quad [u_l(R_{MT^\alpha}) K j_l'(R_{MT^\alpha} K) - u_l'(R_{MT^\alpha}) j_l(R_{MT^\alpha} K)] \end{aligned} \quad (3.115)$$

The Wronskian W is given by:

$$W = [\dot{u}_l(R_{MT^\alpha}) u_l'(R_{MT^\alpha}) - u_l(R_{MT^\alpha}) \dot{u}_l'(R_{MT^\alpha})] \quad (3.116)$$

Transformation of the FLAPW basis functions in systems that possess inversion symmetry

Planewaves transform in a very simple way under the operation $\mathbf{r} \rightarrow -\mathbf{r}$. Let \mathcal{I} be the inversion operator:

$$\mathcal{I} e^{i\mathbf{K}\mathbf{r}} = e^{-i\mathbf{K}\mathbf{r}} = (e^{i\mathbf{K}\mathbf{r}})^* \quad (3.117)$$

The FLAPW basis functions still have this property, i.e. $\varphi_{\mathbf{G}}(\mathbf{k}, -\mathbf{r}) = \varphi_{\mathbf{G}}^*(\mathbf{k}, \mathbf{r})$. Clearly, the system must possess inversion symmetry, because only if there is an equivalent atom at the position $-\mathbf{p}^\mu$ to each atom μ at position \mathbf{p}^μ , the basis functions inside the corresponding spheres can be complex conjugates. The value of the basis function $\varphi_{\mathbf{G}}(\mathbf{k}, \mathbf{r})$ inside the muffin-tin μ is give by:

$$\varphi_{\mathbf{G}}(\mathbf{k}, \mathbf{r}) = \sum_L A_L^{\mu\mathbf{G}}(\mathbf{k}) u_l(r) Y_L(\hat{\mathbf{r}}) + B_L^{\mu\mathbf{G}}(\mathbf{k}) \dot{u}_l(r) Y_L(\hat{\mathbf{r}}) \quad (3.118)$$

The vector $-\mathbf{r}$ lies in the opposite muffin-tin at the position $-\mathbf{p}^\mu$. Let's denote this atom by $-\mu$. Thus, we find:

$$\varphi_{\mathbf{G}}(\mathbf{k}, -\mathbf{r}) = \sum_L A_L^{-\mu\mathbf{G}}(\mathbf{k}) u_l(r) Y_L(\hat{\mathbf{r}}) + B_L^{-\mu\mathbf{G}}(\mathbf{k}) \dot{u}_l(r) Y_L(\hat{\mathbf{r}}) \quad (3.119)$$

The argument of the spherical harmonic is $\hat{\mathbf{r}}$ rather than $-\hat{\mathbf{r}}$, because the vector is expanded in the local frame of the atom $-\mu$. Substituting the explicit form of $A_L^{-\mu\mathbf{G}}(\mathbf{k})$ and $B_L^{-\mu\mathbf{G}}(\mathbf{k})$ from (3.115), yields:

$$\varphi_{\mathbf{G}}(\mathbf{k}, -\mathbf{r}) = \sum_L e^{i\mathbf{K}(-\mathbf{p}^\mu)} i^l Y_L^*(-\mathbf{R}^\mu \hat{\mathbf{K}}) Y_L(\hat{\mathbf{r}}) \{A u_l(r) + B \dot{u}_l(r)\} \quad (3.120)$$

Where it has been used, that $\mathbf{p}^{-\mu} = -\mathbf{p}^\mu$ and $\mathbf{R}^{-\mu} = -\mathbf{R}^\mu$, A and B abbreviates all terms in (3.115) that are real and do not depend on r or $\hat{\mathbf{r}}$. Using that $Y_L(\hat{\mathbf{r}}) = (-1)^l Y_L(\hat{\mathbf{r}})$ (3.120) becomes:

$$\varphi_{\mathbf{G}}(\mathbf{k}, -\mathbf{r}) = \sum_L e^{-i\mathbf{K}(\mathbf{p}^\mu)} (-i)^l Y_L^*(\mathbf{R}^\mu \hat{\mathbf{K}}) Y_L(\hat{\mathbf{r}}) \{A u_l(r) + B \dot{u}_l(r)\} \quad (3.121)$$

In the last step it can be exploited that $Y_{l-m}(\hat{\mathbf{r}}) = (-1)^m Y_m^*(\hat{\mathbf{r}})$. Substituting $m' = -m$ (3.121) becomes:

$$\varphi_{\mathbf{G}}(\mathbf{k}, -\mathbf{r}) = \sum_{lm'} e^{-i\mathbf{K}(\mathbf{p}^\mu)} (-i)^l Y_{lm'}(\mathbf{R}^\mu \hat{\mathbf{K}}) Y_{lm'}^*(\hat{\mathbf{r}}) \{A u_l(r) + B \dot{u}_l(r)\} \quad (3.122)$$

Hence, we have shown, that the FLAPW basis functions transform according to

$$\varphi_{\mathbf{G}}(\mathbf{k}, -\mathbf{r}) = \varphi_{\mathbf{G}}^*(\mathbf{k}, \mathbf{r}) \quad (3.123)$$

in the interstitial region and the muffin-tins, if the system possesses inversion symmetry.

The Hamiltonian Matrix of Systems with Inversion Symmetry

The property of the FLAPW basis functions derived in the previous section leads to property of the Hamiltonian and overlap matrix. In systems that possess inversion symmetry these two matrices are real symmetric rather than complex hermitian. The Hamiltonian depends explicitly on \mathbf{r} via the potential. The matrix elements are given by:

$$H^{\mathbf{G}'\mathbf{G}}(\mathbf{k}) = \int \varphi_{\mathbf{G}'}^*(\mathbf{k}, \mathbf{r}) \mathcal{H}(\mathbf{r}) \varphi_{\mathbf{G}}(\mathbf{k}, \mathbf{r}) d^3r \quad (3.124)$$

Substituting $\mathbf{r}' = -\mathbf{r}$ yields:

$$H^{\mathbf{G}'\mathbf{G}}(\mathbf{k}) = \int \varphi_{\mathbf{G}'}(\mathbf{k}, \mathbf{r}') \mathcal{H}(\mathbf{r}') \varphi_{\mathbf{G}}^*(\mathbf{k}, \mathbf{r}') d^3r' \quad (3.125)$$

Where (3.123) and $\mathcal{H}(\mathbf{r}) = \mathcal{H}(-\mathbf{r})$ have been used. In addition the Hamiltonian operator is real, i.e. $\mathcal{H}(\mathbf{r}) = \mathcal{H}^*(\mathbf{r})$. Thus, we finally obtain:

$$\begin{aligned} H^{\mathbf{G}'\mathbf{G}}(\mathbf{k}) &= \int \varphi_{\mathbf{G}'}(\mathbf{k}, \mathbf{r}') \mathcal{H}^*(\mathbf{r}') \varphi_{\mathbf{G}}^*(\mathbf{k}, \mathbf{r}') d^3r \\ &= (H^{\mathbf{G}'\mathbf{G}}(\mathbf{k}))^* \end{aligned} \quad (3.126)$$

Apparently, the same relation holds for the overlap matrix. The fact, that the two matrices are real means a great simplification in actual calculation. In principle, the diagonalization of a hermitian matrix is no more difficult than in the real case. However, one complex multiplication contains four real multiplication, and therefore the complex problem is far more “expensive” than the real, and the diagonalization needs the biggest part of the computer-time in each iteration.

3.4 Brillouin Zone Integration and Fermi Energy

If density functional theory is applied to infinite periodic solids, quantities that are given by integrals of functions that depend on the band and the Bloch vector over the Brillouin zone have to be determined. These integrations stretch only over the occupied part of the band, i.e. over the region of the Brillouin zone where the band energy $\epsilon_\nu(\mathbf{k})$ (ν is the band index) is smaller than the Fermi energy. Hence, the integrals are of the form

$$\frac{1}{V_{BZ}} \int_{BZ} \sum_{\nu, \epsilon_\nu(\mathbf{k}) < E_F} f_\nu(\mathbf{k}) d^3k, \quad (3.127)$$

where f is the function to be integrated. Example of such quantities are the number of electrons per unit cell

$$N = \frac{1}{V_{BZ}} \int_{BZ} \sum_{\nu, \epsilon_\nu(\mathbf{k}) < E_F} 1 d^3k, \quad (3.128)$$

the electron (charge) density (cf. section 3.6) and the eigenvalue sum

$$\frac{1}{V_{BZ}} \int_{BZ} \sum_{\nu, \epsilon_\nu(\mathbf{k}) < E_F} \epsilon_\nu(\mathbf{k}) d^3k. \quad (3.129)$$

Numerically, these integrations are performed on a discrete mesh in the Brillouin zone. In fact, only the irreducible part can be used to save computer time. There are different methods, that can be used to perform the integration, e.g. the special points method [CC73, Cun74] and the tetrahedron method [JA71, LT72, BJA94]. The special points method is a method to integrate smoothly varying periodic functions of \mathbf{k} . The function to be integrated has to be calculated a set of special points in the (irreducible) Brillouin zone, each of which is assigned a weight. Thus, the Brillouin zone integration is transformed into a sum over a set of \mathbf{k} -points. However,

these weights do not take into account, that the integration stretches only over the occupied part of the bands. This problem is solved by including only those bands into the summation that have an energy below the Fermi energy at the \mathbf{k} -point under consideration. Thus, the integrals become:

$$\frac{1}{V_{BZ}} \int_{BZ} \sum_{\nu, \epsilon_{\nu}(\mathbf{k}) < E_F} f_{\nu}(\mathbf{k}) d^3k \longrightarrow \sum_{\mathbf{k}} \sum_{\nu, \epsilon_{\nu}(\mathbf{k}) < E_F} f_{\nu}(\mathbf{k}) w(\mathbf{k}) \quad (3.130)$$

Alternatively, this integration can be viewed as an integration over the whole Brillouin zone, where the function to be integrated is given by a product of the function f with a step function that cuts out the region of the Brillouin zone, where the band energy is above the Fermi energy. Clearly, the resulting function does not satisfy the condition of being smoothly varying. Therefore, the special k-points method does not converge very quickly, and rather many k-points are needed to obtain accurate results. On the other hand this method is simple to implement, because the weights depend only on \mathbf{k} and the band energy (via the step function) at each k-point. Another problem arises from this “sharp” differentiation between occupied and empty bands (parts of bands). Let’s consider a band that is very close to the Fermi energy at a certain k-point. During the iterations the energy of this band might rise above or drop below the Fermi energy. This leads to sudden changes in the charge density, which can slow down or even prevent the convergence of the density. These sudden changes are clearly a result of the discretization in momentum space. To avoid this problem, the sharp edges of the step function have to be removed. This can be done, e.g. by using the Fermi function $(e^{(\epsilon - E_F)/k_B T} + 1)^{-1}$ rather than the step function. In other words, the function to be integrated is artificially made smoothly varying. The temperature T can then be adjusted to obtain the best convergence. This method is called temperature broadening.

In the current implementation of the FLAPW method the Fermi energy is determined in two steps. First the bands are occupied (at all k-points simultaneously), starting from the lowest energy, until the sum of their weights equals the total number of electrons per unit cell, i.e. the discretized equivalent of (3.128) is solved at $T = 0$. Then the step function is replaced by the Fermi and the Fermi energy is determined from the requirement that:

$$N = \sum_{\mathbf{k}} \sum_{\nu} w(\mathbf{k}, \epsilon_{\nu}(\mathbf{k}) - E_F) \quad (3.131)$$

Where the weights are given by:

$$w(\mathbf{k}, \epsilon_{\nu}(\mathbf{k}) - E_F) = w(\mathbf{k}) \frac{1}{e^{(\epsilon_{\nu}(\mathbf{k}) - E_F)/k_B T} + 1} \quad (3.132)$$

The weights $w(\mathbf{k}, \epsilon_{\nu}(\mathbf{k}) - E_F)$ are stored to be used for later Brillouin zone integrations.

3.5 Representation of the Density and the Potential

The expansion of the charge density ρ ⁵ and the potential is very similar to expansion of the wavefunction. In the interstitial-region the two quantities are expanded into three-dimensional planewave, inside the muffin-tins they are represented by spherical harmonics and radial functions, which are store on an exponential mesh and in the vacuum they are expanded into two-dimensional planewave and z-depended functions, which are also given on an exponential mesh. However, the charge density is given by

$$\rho(\mathbf{r}) = \sum_i |\psi_i(\mathbf{r})|^2, \quad (3.133)$$

which contains terms of the form $e^{i(\mathbf{G}-\mathbf{G}')\mathbf{r}}$. Consequently, for a consistent representation the charge density cut-off has to be twice the wavefunction cut-off G_{max} . In section 3.3.3 we explained, that the potential is also needed up to cut-off of $2G_{max}$. This leads to a large number of coefficients, that need to be stored. Fortunately, this number can be reduced, if the symmetry of the system is exploited.

Of course, the charge density and the potential posses the lattice symmetry. Therefore, the expansion into planewaves is more general than necessary. The Plane-waves can be replaced by symmetrized planewaves, the so called stars. They are defined by:

$$\Phi_s^{3D}(\mathbf{r}) = \frac{1}{N_{op}} \sum_{op} e^{i\mathbf{R}\mathbf{G}(\mathbf{r}-\boldsymbol{\tau})} \quad (3.134)$$

where $\{\mathbf{R}|\boldsymbol{\tau}\}$ are the symmetry operation of the lattice space group; if all the translation vectors $\boldsymbol{\tau}$ are zero, the space group is call symmorphic. By this construction all planewaves, that are symmetry equivalent, are combined to form one star. The two-dimensional stars $\Phi_s^{2D}(\mathbf{r})$ are defined in the same way, applying the operations of the two-dimensional space group only.

The same arguments can be applied to the expansion of the $\rho(V)$ inside the muffin-tins. In this case the relevant symmetry group is the point group of the atom under consideration. Thus, different expansions are used at different atoms in general. The symmetrized functions are called lattice harmonics and they are linear combinations of spherical harmonics.

$$K_\nu(\hat{\mathbf{r}}) = \sum_m c_{\nu,m}^\alpha Y_L(\hat{\mathbf{r}}) \quad (3.135)$$

The lattice harmonics are real, orthonormal and invariant under the point group operations. Finally, the expansion of the the charge density has the form

$$\rho(\mathbf{r}) = \begin{cases} \sum_s \rho_s \Phi_s^{3D}(\mathbf{r}) & \mathbf{r} \in I \\ \sum_s \rho_s(z) \Phi_s^{2D}(\mathbf{r}) & \mathbf{r} \in \text{Vakuum} \\ \sum_\nu \rho_\nu^\alpha(r) K_\nu(\hat{\mathbf{r}}) & \mathbf{r} \in MT^\alpha \end{cases} \quad (3.136)$$

⁵The charge density is related to the electron density by $\rho(\mathbf{r}) = -en(\mathbf{r})$. However, the program is written in Hartree units, where $e = 1$, therefore ρ and n are equal.

The Potential is expanded in exactly the same way.

3.6 Construction of the Electron Density

In this section we will discuss the determination of the charge density from the eigenfunctions. However, we will concentrate on the charge density inside the muffin-tin spheres and two related issues, because the formulae derived in this section will be the starting point for the discussion of the contributions to the charge density of the local orbitals (cf. chap. 5). The local orbitals are an extension to the FLAPW basis set. They do not contribute to the charge density in the interstitial and the vacuum-region, because they are completely localized inside the muffin-tins.

In density functional calculations of an infinite periodic solid the electron density is given by an integral over the Brillouin zone (cf. (2.20)).

$$n(\mathbf{r}) = \frac{1}{V_{BZ}} \int_{BZ} \sum_{\nu, \epsilon_\nu(\mathbf{k}) < E_F} |\psi_\nu(\mathbf{k}, \mathbf{r})|^2 d^3k \quad (3.137)$$

Where V_{BZ} is the volume of the Brillouin zone, ν is the band index and E_F is the Fermi energy. In spin-polarized calculations the summation includes also the spin-index σ (cf. (2.8)), while in a non-magnetic calculation a factor “2” has to be added to account for the spin-degeneracy. In the case of film calculations the three-dimensional Brillouin zone is replaced by a two-dimensional Brillouin zone. In both cases integration methods that sample eigenfunctions and the eigenvalues on discrete k-point are used to compute the integrals. These methods transform the integration into a weighted sum over the k-points, where the choice of k-points and their weights depend on the integration method used. These weights depend not only on the k-point, but also on the energy of a band, i.e. on the band (index), because each band contributes to the electron density only if its energy is below the Fermi energy.

$$n(\mathbf{r}) = \sum_{\mathbf{k}} \sum_{\nu} |\psi_\nu(\mathbf{k}, \mathbf{r})|^2 w(\nu, \mathbf{k}) \quad (3.138)$$

Within the FLAPW method the eigenfunctions are represented in terms of the coefficients of the augmented planewaves.

$$\psi_\nu(\mathbf{k}, \mathbf{r}) = \sum_{\mathbf{G}} c_\nu^{\mathbf{G}}(\mathbf{k}) \varphi_{\mathbf{G}}(\mathbf{k}, \mathbf{r}) \quad (3.139)$$

Inside the muffin-tin spheres each planewave is coupled to a sum of spherical harmonics and radial functions. Hence, in a sphere μ an eigenfunction is given by:

$$\psi_\nu^\mu(\mathbf{k}, \mathbf{r}) = \sum_{\mathbf{G}} c_\nu^{\mathbf{G}}(\mathbf{k}) \sum_L A_L^{\mu\mathbf{G}}(\mathbf{k}) u_l^\alpha(r) Y_L(\hat{\mathbf{r}}) + B_L^{\mu\mathbf{G}}(\mathbf{k}) \dot{u}_l^\alpha(r) Y_L(\hat{\mathbf{r}}) \quad (3.140)$$

The $A_L^{\mu\mathbf{G}}(\mathbf{k})$ and $B_L^{\mu\mathbf{G}}(\mathbf{k})$ coefficients can be replaced by band dependent A- and B-coefficients, obtained by performing the contraction over the planewaves:

$$\psi_\nu^\mu(\mathbf{k}, \mathbf{r}) = \sum_L A_{L,\nu}^\mu(\mathbf{k}) u_l^\alpha(r) Y_L(\hat{\mathbf{r}}) + B_{L,\nu}^\mu(\mathbf{k}) \dot{u}_l^\alpha(r) Y_L(\hat{\mathbf{r}}), \quad (3.141)$$

where

$$A_{L,\nu}^\mu(\mathbf{k}) = \sum_{\mathbf{G}} c_\nu^{\mathbf{G}}(\mathbf{k}) A_L^{\mu\mathbf{G}}(\mathbf{k}), \quad B_{L,\nu}^\mu(\mathbf{k}) = \sum_{\mathbf{G}} c_\nu^{\mathbf{G}}(\mathbf{k}) B_L^{\mu\mathbf{G}}(\mathbf{k}). \quad (3.142)$$

3.6.1 “*l*-like” Charge

Since the wavefunctions are expanded into spherical harmonics inside the muffin-tin spheres, they can be split up into contributions with a certain *l*-character.

$$\psi_\nu^\mu(\mathbf{k}, \mathbf{r}) = \sum_l \psi_{\nu,l}^\mu(\mathbf{k}, \mathbf{r}) \quad (3.143)$$

The particle density of a certain state depends on the square of the wavefunction. Therefore, it contains cross-terms with a mixture of different *l*'s.

$$n_\nu^\mu(\mathbf{r}) = \frac{1}{V_{BZ}} \int_{BZ} \sum_l |\psi_{\nu,l}^\mu(\mathbf{k}, \mathbf{r})|^2 + \sum_{l'l} 2 \left(\psi_{\nu,l'}^\mu(\mathbf{k}, \mathbf{r}) \right)^* \psi_{\nu,l}^\mu(\mathbf{k}, \mathbf{r}) d^3 k \quad (3.144)$$

If, however, the density is integrated over the muffin-tin, the cross-terms vanish because of the orthogonality of the spherical harmonics. Thus, the total electron density inside a sphere can be written as a sum over contributions with definite *l*-character.

$$n_\nu^\mu = \sum_l n_{\nu,l}^\mu, \quad n_{\nu,l}^\mu = \frac{1}{V_{BZ}} \int_{BZ} \int_{MT^\mu} |\psi_{\nu,l}^\mu(\mathbf{k}, \mathbf{r})|^2 d^3 r d^3 k \quad (3.145)$$

Where $n_{\nu,l}^\mu$ is called “*l*-like” charge. We can also define a *k*-dependent *l*-like charge by:

$$n_{\nu,l}^\mu(\mathbf{k}) = \int_{MT^\mu} |\psi_{\nu,l}^\mu(\mathbf{k}, \mathbf{r})|^2 d^3 r \quad (3.146)$$

Substituting (3.141) yields:

$$n_{\nu,l}^\mu(\mathbf{k}) = \sum_{m=-l}^l |A_{L,\nu}^\mu(\mathbf{k})|^2 + |B_{L,\nu}^\mu(\mathbf{k})|^2 \dot{N}_l^\alpha \quad (3.147)$$

Where

$$\dot{N}_l^\alpha = \int_0^{R_{MT^\alpha}} (\dot{u}_l^\alpha(r))^2 r^2 dr \quad (3.148)$$

and the orthogonality of the spherical harmonics, the normalization of u_l^α and the orthogonality of u_l^α and \dot{u}_l^α have been used.

3.6.2 Determination of the Optimal Energy Parameter

In order to minimize the linearization error, the energy parameters should be chosen as close to the band energies as possible. However, the band energies $\epsilon_\nu(\mathbf{k})$ depend on \mathbf{k} whereas the energy parameters E_l^α are constants. In addition, the radial functions contribute to the eigenfunctions of different band with different energies. Therefore,

deviations between $\epsilon_\nu(\mathbf{k})$ and E_l^α have to be accepted. An optimal choice can be obtained from the requirement, that the energy parameters minimize

$$\int_{BZ} \sum_{\nu, \epsilon_\nu(\mathbf{k}) < E_F} (\epsilon_\nu(\mathbf{k}) - E_l^\alpha)^2 n_{\nu,l}^\mu(\mathbf{k}) d^3 k, \quad (3.149)$$

which is the quadratic error weighted with the amount of charge that each band contributes to the l-like charge with the l-character of the energy parameter. Setting the derivative ($\partial/\partial E_l^\alpha$) equal to zero yields the optimal energy parameter:

$$E_l^\alpha = \left(\int_{BZ} \sum_{\nu, \epsilon_\nu(\mathbf{k}) < E_F} \epsilon_\nu(\mathbf{k}) n_{\nu,l}^\mu(\mathbf{k}) d^3 k \right) / \left(\int_{BZ} \sum_{\nu, \epsilon_\nu(\mathbf{k}) < E_F} n_{\nu,l}^\mu(\mathbf{k}) d^3 k \right) \quad (3.150)$$

The Brillouin zone integration methods transform this into a sum over a discrete k-point set.

$$E_l^\alpha = \left(\sum_{\mathbf{k}} \sum_{\nu} \epsilon_\nu(\mathbf{k}) n_{\nu,l}^\mu(\mathbf{k}) w(\nu, \mathbf{k}) \right) / \left(\sum_{\mathbf{k}} \sum_{\nu} n_{\nu,l}^\mu(\mathbf{k}) w(\nu, \mathbf{k}) \right) \quad (3.151)$$

3.6.3 Construction of the Electron Density in the Muffin-Tins

Substituting (3.141) into (3.137) yields the electron density in the muffin-tin spheres.

$$n^\mu(\mathbf{r}) = \frac{1}{V_{BZ}} \int_{BZ} \sum_{\nu, \epsilon_\nu(\mathbf{k}) < E_F} \sum_{L'} \left(A_{L',\nu}^\mu(\mathbf{k}) u_l^\alpha(r) + B_{L',\nu}^\mu(\mathbf{k}) \dot{u}_l^\alpha(r) \right)^* Y_{L'}^*(\hat{\mathbf{r}}) \sum_L \left(A_{L,\nu}^\mu(\mathbf{k}) u_l^\alpha(r) + B_{L,\nu}^\mu(\mathbf{k}) \dot{u}_l^\alpha(r) \right) Y_L(\hat{\mathbf{r}}) d^3 k \quad (3.152)$$

The particle density inside the muffin-tins is also expanded into spherical harmonics.

$$n^\mu(\mathbf{r}) = \sum_L C_L^\mu(r) Y_L(\hat{\mathbf{r}}) \quad (3.153)$$

The coefficients $C_{L'}^\mu(r)$ can be determined by multiplying (3.152) with $\int d\Omega Y_{L'}(\hat{\mathbf{r}})$.

$$C_{L'}^\mu(r) = \frac{1}{V_{BZ}} \int_{BZ} \sum_{\nu, \epsilon_\nu(\mathbf{k}) < E_F} \sum_{L'} \left(A_{L',\nu}^\mu(\mathbf{k}) u_l^\alpha(r) + B_{L',\nu}^\mu(\mathbf{k}) \dot{u}_l^\alpha(r) \right)^* \sum_L \left(A_{L,\nu}^\mu(\mathbf{k}) u_l^\alpha(r) + B_{L,\nu}^\mu(\mathbf{k}) \dot{u}_l^\alpha(r) \right) G_{L'L'}^{mm'm''} d^3 k \quad (3.154)$$

with

$$G_{L'L'}^{mm'm''} = \int Y_{lm}^* Y_{l'm'} Y_{l''m''} d\Omega \quad (3.155)$$

where it has been used, that the gaunt coefficients are real, i.e.

$$\int Y_{lm} Y_{l'm'}^* Y_{l''m''} d\Omega = \int Y_{lm}^* Y_{l'm'} Y_{l''m''} d\Omega \quad (3.156)$$

Finally, applying a Brillouin zone integration method yields:

$$\begin{aligned}
C_{L\nu}^\mu(r) &= \sum_{l'l} \left(\sum_{\mathbf{k}} \sum_{\nu} \sum_{m'm} \left(A_{L',\nu}^\mu(\mathbf{k}) \right)^* A_{L,\nu}^\mu(\mathbf{k}) G_{ll'l''}^{mm'm''} w(\nu, \mathbf{k}) \right) u_{l'}^\alpha(r) u_l^\alpha(r) \\
&+ \sum_{l'l} \left(\sum_{\mathbf{k}} \sum_{\nu} \sum_{m'm} \left(A_{L',\nu}^\mu(\mathbf{k}) \right)^* B_{L,\nu}^\mu(\mathbf{k}) G_{ll'l''}^{mm'm''} w(\nu, \mathbf{k}) \right) u_{l'}^\alpha(r) \dot{u}_l^\alpha(r) \\
&+ \sum_{l'l} \left(\sum_{\mathbf{k}} \sum_{\nu} \sum_{m'm} \left(B_{L',\nu}^\mu(\mathbf{k}) \right)^* A_{L,\nu}^\mu(\mathbf{k}) G_{ll'l''}^{mm'm''} w(\nu, \mathbf{k}) \right) \dot{u}_{l'}^\alpha(r) u_l^\alpha(r) \\
&+ \sum_{l'l} \left(\sum_{\mathbf{k}} \sum_{\nu} \sum_{m'm} \left(B_{L',\nu}^\mu(\mathbf{k}) \right)^* B_{L,\nu}^\mu(\mathbf{k}) G_{ll'l''}^{mm'm''} w(\nu, \mathbf{k}) \right) \dot{u}_{l'}^\alpha(r) \dot{u}_l^\alpha(r)
\end{aligned} \tag{3.157}$$

3.6.4 Construction of the Electron Density in the Interstitial Region

In the interstitial region the wavefunctions are represented in the following form.

$$\psi_\nu(\mathbf{k}, \mathbf{r}) = \sum_{\mathbf{G}} c_\nu^{\mathbf{G}}(\mathbf{k}) e^{i(\mathbf{G}+\mathbf{k})\mathbf{r}} \tag{3.158}$$

Starting from (2.8) the electron density is given by:

$$n(\mathbf{r}) = \frac{1}{V_{BZ}} \int_{BZ} \sum_{\nu, \epsilon_\nu(\mathbf{k}) < E_F} \sum_{\mathbf{G}'\mathbf{G}''} \left(c_\nu^{\mathbf{G}'}(\mathbf{k}) \right)^* c_\nu^{\mathbf{G}''}(\mathbf{k}) d^3k e^{i(\mathbf{G}''-\mathbf{G}')\mathbf{r}} \tag{3.159}$$

The electron density in the interstitial region is also expanded into planewaves.

$$n(\mathbf{r}) = \sum_{\mathbf{G}} n^{\mathbf{G}} e^{i\mathbf{G}\mathbf{r}} \tag{3.160}$$

Hence, the planewave coefficients of the electron density are:

$$n^{\mathbf{G}} = \frac{1}{V_{BZ}} \int_{BZ} \sum_{\nu, \epsilon_\nu(\mathbf{k}) < E_F} \sum_{\substack{\mathbf{G}'\mathbf{G}'' \\ \mathbf{G}''-\mathbf{G}'=\mathbf{G}}} \left(c_\nu^{\mathbf{G}'}(\mathbf{k}) \right)^* c_\nu^{\mathbf{G}''}(\mathbf{k}) d^3k \tag{3.161}$$

Apparently, the planewave cut-off of the particle density has to be twice the cut-off of the wavefunction expansion (G_{max}) to allow an accurate description. The \mathbf{k} and state dependent density

$$n_\nu^{\mathbf{G}}(\mathbf{k}) = \sum_{\substack{\mathbf{G}'\mathbf{G}'' \\ \mathbf{G}''-\mathbf{G}'=\mathbf{G}}} \left(c_\nu^{\mathbf{G}'}(\mathbf{k}) \right)^* c_\nu^{\mathbf{G}''}(\mathbf{k}) = \sum_{\mathbf{G}'} \left(c_\nu^{\mathbf{G}'}(\mathbf{k}) \right)^* c_\nu^{(\mathbf{G}+\mathbf{G}')}(\mathbf{k}) \tag{3.162}$$

is given by a convolution in momentum space. For each coefficient a sum over \mathbf{G} has to be performed. Consequently, the numerical effort put into the determination of

$n_\nu^{\mathbf{G}}(\mathbf{k})$ scales proportional to the number of G -vectors squared, i.e. proportional to $(G_{max})^6$. However, $n_\nu^{\mathbf{G}}(\mathbf{k})$ can be calculated more efficiently using the fast Fourier transform (FFT). First, $c_\nu^{\mathbf{G}}(\mathbf{k})$ is Fourier transformed to real space, where it is squared on a real space mesh yielding $n_\nu(\mathbf{k}, \mathbf{r})$, then all states are summed up and finally the resulting particle density is back-transformed to momentum space.

$$c_\nu^{\mathbf{G}}(\mathbf{k}) \xrightarrow{FFT} \psi_\nu(\mathbf{k}, \mathbf{r}) \xrightarrow{square} n_\nu(\mathbf{k}, \mathbf{r}) \xrightarrow{\sum_\nu} n(\mathbf{k}, \mathbf{r}) \xrightarrow{FFT^{-1}} n^{\mathbf{G}}(\mathbf{k})$$

With this scheme the numerical effort increases proportional to $(G_{max})^3 \ln((G_{max})^3)$, which is a major improvement for large systems. In a last step the planewaves have to be combined to form the three-dimensional stars.

3.6.5 Construction of the Electron Density in the Vacuum Region

In the vacuum region the wavefunctions are expanded into two-dimensional plane-waves parallel to the surface and z-dependent functions perpendicular to the surface.

$$\psi_\nu(\mathbf{k}_\parallel, \mathbf{r}) = \sum_{\mathbf{G}_\parallel \mathbf{G}_\perp} c_\nu^{\mathbf{G}_\parallel \mathbf{G}_\perp}(\mathbf{k}_\parallel) \left(A_{\mathbf{G}_\parallel \mathbf{G}_\perp}(\mathbf{k}_\parallel) u_{\mathbf{G}_\parallel}(\mathbf{k}_\parallel, z) + B_{\mathbf{G}_\parallel \mathbf{G}_\perp}(\mathbf{k}_\parallel) \dot{u}_{\mathbf{G}_\parallel}(\mathbf{k}_\parallel, z) \right) e^{i(\mathbf{G}_\parallel + \mathbf{k}_\parallel) \mathbf{r}_\parallel} \quad (3.163)$$

Hence, the electron density is given by:

$$\begin{aligned} n(\mathbf{r}) = & \frac{1}{V_{BZ}} \int_{BZ} \sum_{\nu, \epsilon_\nu(\mathbf{k}) < E_F} \sum_{\mathbf{G}'_\parallel \mathbf{G}'_\perp} \sum_{\mathbf{G}''_\parallel \mathbf{G}''_\perp} \\ & \left(c_\nu^{\mathbf{G}'_\parallel \mathbf{G}'_\perp}(\mathbf{k}_\parallel) \left(A_{\mathbf{G}'_\parallel \mathbf{G}'_\perp}(\mathbf{k}_\parallel) u_{\mathbf{G}'_\parallel}(\mathbf{k}_\parallel, z) + B_{\mathbf{G}'_\parallel \mathbf{G}'_\perp}(\mathbf{k}_\parallel) \dot{u}_{\mathbf{G}'_\parallel}(\mathbf{k}_\parallel, z) \right) \right)^* \\ & \left(c_\nu^{\mathbf{G}''_\parallel \mathbf{G}''_\perp}(\mathbf{k}_\parallel) \left(A_{\mathbf{G}''_\parallel \mathbf{G}''_\perp}(\mathbf{k}_\parallel) u_{\mathbf{G}''_\parallel}(\mathbf{k}_\parallel, z) + B_{\mathbf{G}''_\parallel \mathbf{G}''_\perp}(\mathbf{k}_\parallel) \dot{u}_{\mathbf{G}''_\parallel}(\mathbf{k}_\parallel, z) \right) \right) d^3 k \\ & e^{i(\mathbf{G}''_\parallel - \mathbf{G}'_\parallel) \mathbf{r}_\parallel} \end{aligned} \quad (3.164)$$

The particle density in the vacuum is represented in the following form.

$$n(\mathbf{r}) = \sum_{\mathbf{G}_\parallel} n^{\mathbf{G}_\parallel}(z) e^{i\mathbf{G}_\parallel \mathbf{r}_\parallel} \quad (3.165)$$

Performing the Brillouin zone integration on a discrete \mathbf{k}_\parallel -mesh and carrying out the summation over \mathbf{G}'_\perp and \mathbf{G}''_\perp we find that the coefficients $n^{\mathbf{G}_\parallel}(z)$ are:

$$\begin{aligned} n^{\mathbf{G}_\parallel}(z) = & \sum_{\mathbf{k}_\parallel} \sum_{\nu} \sum_{\mathbf{G}'_\parallel} \left(A_{\mathbf{G}'_\parallel, \nu}(\mathbf{k}_\parallel) \right)^* A_{(\mathbf{G}_\parallel + \mathbf{G}'_\parallel), \nu}(\mathbf{k}_\parallel) w(\nu, \mathbf{k}_\parallel) u_{\mathbf{G}'_\parallel}(\mathbf{k}_\parallel, z) u_{(\mathbf{G}_\parallel + \mathbf{G}'_\parallel)}(\mathbf{k}_\parallel, z) \\ & + \sum_{\mathbf{k}_\parallel} \sum_{\nu} \sum_{\mathbf{G}'_\parallel} \left(A_{\mathbf{G}'_\parallel, \nu}(\mathbf{k}_\parallel) \right)^* B_{(\mathbf{G}_\parallel + \mathbf{G}'_\parallel), \nu}(\mathbf{k}_\parallel) w(\nu, \mathbf{k}_\parallel) u_{\mathbf{G}'_\parallel}(\mathbf{k}_\parallel, z) \dot{u}_{(\mathbf{G}_\parallel + \mathbf{G}'_\parallel)}(\mathbf{k}_\parallel, z) \end{aligned}$$

$$\begin{aligned}
& + \sum_{\mathbf{k}_{\parallel}} \sum_{\nu} \sum_{\mathbf{G}'_{\parallel}} \left(B_{\mathbf{G}'_{\parallel}, \nu}(\mathbf{k}_{\parallel}) \right)^* A_{(\mathbf{G}_{\parallel} + \mathbf{G}'_{\parallel}), \nu}(\mathbf{k}_{\parallel}) w(\nu, \mathbf{k}_{\parallel}) \dot{u}_{\mathbf{G}'_{\parallel}}(\mathbf{k}_{\parallel}, z) u_{(\mathbf{G}_{\parallel} + \mathbf{G}'_{\parallel})}(\mathbf{k}_{\parallel}, z) \\
& + \sum_{\mathbf{k}_{\parallel}} \sum_{\nu} \sum_{\mathbf{G}'_{\parallel}} \left(B_{\mathbf{G}'_{\parallel}, \nu}(\mathbf{k}_{\parallel}) \right)^* B_{(\mathbf{G}_{\parallel} + \mathbf{G}'_{\parallel}), \nu}(\mathbf{k}_{\parallel}) w(\nu, \mathbf{k}_{\parallel}) \dot{u}_{\mathbf{G}'_{\parallel}}(\mathbf{k}_{\parallel}, z) \dot{u}_{(\mathbf{G}_{\parallel} + \mathbf{G}'_{\parallel})}(\mathbf{k}_{\parallel}, z)
\end{aligned} \tag{3.166}$$

with

$$A_{\mathbf{G}_{\parallel}, \nu}(\mathbf{k}_{\parallel}) = \sum_{G_{\perp}} c_{\nu}^{\mathbf{G}_{\parallel} G_{\perp}}(\mathbf{k}_{\parallel}) A_{\mathbf{G}_{\parallel} G_{\perp}}(\mathbf{k}_{\parallel}), \quad B_{\mathbf{G}_{\parallel}, \nu}(\mathbf{k}_{\parallel}) = \sum_{G_{\perp}} c_{\nu}^{\mathbf{G}_{\parallel} G_{\perp}}(\mathbf{k}_{\parallel}) B_{\mathbf{G}_{\parallel} G_{\perp}}(\mathbf{k}_{\parallel}) \tag{3.167}$$

Here, the terms of the form

$$\sum_{\mathbf{G}'_{\parallel}} \left(A_{\mathbf{G}'_{\parallel}, \nu}(\mathbf{k}_{\parallel}) \right)^* A_{(\mathbf{G}_{\parallel} + \mathbf{G}'_{\parallel}), \nu}(\mathbf{k}_{\parallel}) u_{\mathbf{G}'_{\parallel}}(\mathbf{k}_{\parallel}, z) u_{(\mathbf{G}_{\parallel} + \mathbf{G}'_{\parallel})}(\mathbf{k}_{\parallel}, z)$$

represent convolutions in momentum space. Similar to the interstitial region these terms could be calculated more efficiently, using two-dimensional fast Fourier transform. However, there are far less two-dimensional planewaves than three-dimensional planewaves. Therefore, the possible saving of computer time is much smaller.

3.7 Construction of the Coulomb Potential

The Coulomb potential consists of two parts, the Hartree term $V_H(\mathbf{r})$ and the external potential of the nuclei $V_i(\mathbf{r})$.

$$V_c(\mathbf{r}) = V_H(\mathbf{r}) + V_i(\mathbf{r}) \tag{3.168}$$

The Hartree potential has to be determined from the charge density via the Poisson equation.

$$\Delta V_H(\mathbf{r}) = 4\pi\rho(\mathbf{r}) \tag{3.169}$$

In real space the solution of 3.169 is given by

$$V_H(\mathbf{r}) = \int \frac{4\pi\rho(\mathbf{r}')}{|\mathbf{r} - \mathbf{r}'|} d^3\mathbf{r}'. \tag{3.170}$$

In reciprocal space, however, the Poisson equation is diagonal, as a result the solution is very simple.

$$V_H(\mathbf{G}) = \frac{4\pi\rho(\mathbf{G})}{\mathbf{G}^2} \tag{3.171}$$

Therefore, and because of the representation of the charge density and the potential in the interstitial- and vacuum-region, the solution of the Poisson equation in reciprocal space appears to be convenient. However, due to the rather localized core and valence states the charge density changes on a very small length scale near the nuclei. Therefore, the planewave expansion of ρ convergences slowly, and a direct use of (3.171) is impractical, if not impossible. This difficulty can be circumvent via the pseudocharge method.

3.7.1 The Pseudocharge Method

The pseudocharge method, developed by Weinert [Wei81], is a very elegant technique to calculate the interstitial and vacuum Hartree potential. The underlying idea is to divide the solution of the Poisson equation into two steps. In the first step the true muffin-tin charge is replaced by a convergent pseudocharge density $\tilde{\rho}$, that leads to the same potential outside the muffin-tins. Then the interstitial (and vacuum) potential is calculated in reciprocal space. In the second step the muffin-tin potential is determined from the Dirichlet boundary value problem, defined by the exact muffin-tin charge and the interstitial potential on the muffin-tin sphere boundaries. The potential outside the the muffin-tin spheres due to a charge distribution inside the sphere is determined completely by its multipole moments q_L .

$$V(\mathbf{r}) = \sum_{l=0}^{\infty} \sum_{m=-l}^l \frac{4\pi}{2l+1} \frac{q_L}{r^{l+1}} Y_L(\hat{\mathbf{r}}), \quad (3.172)$$

However, the multipole moments do not define the charge density uniquely. The charge density is given by:

$$\rho(\mathbf{r}) = \rho_I(\mathbf{r})\Theta(\mathbf{r} \in I) + \sum_{\alpha} \rho_{\alpha}(\mathbf{r})\Theta(\mathbf{r} \in MT^{\alpha}) \quad (3.173)$$

Of course, in film calculation there is also a vacuum charge, and we will come back to this later. 3.173 can be rewritten

$$\rho(\mathbf{r}) = \rho_I(\mathbf{r}) + \sum_{\alpha} [\rho_{\alpha}(\mathbf{r}) - \rho_I(\mathbf{r})]\Theta(\mathbf{r} \in MT^{\alpha}) \quad (3.174)$$

Thus, the interstitial charge has been extended into the muffin-tin and subtracted there again. The second term in 3.174 can now be replaced by a pseudocharge $\tilde{\rho}^{\alpha}$, that has the same multipole moments (s. [Wei81] for details). The resultant pseudocharge $\tilde{\rho}$ is given by

$$\tilde{\rho}(\mathbf{r}) = \rho_I(\mathbf{r}) + \sum_{\alpha} \tilde{q}^{\alpha}(\mathbf{r}) \quad (3.175)$$

$\tilde{\rho}(\mathbf{r})$ is constructed to have a more rapidly converging Fourier expansion than the original charge density $\rho(\mathbf{r})$. Therefore, the Poisson equation can now be solved using (3.171).

Still, the muffin-tin potential V_{MT}^{α} remains to be determined. For this step the exact muffin-tin charge ρ_{α} has to be used. Since, the interstitial potential is already known at this point, the calculation of V_{MT}^{α} constitutes a classical spherically symmetric Dirichlet boundary value problem, which can be solved by the Green's function method [Jac83].

$$V_{MT}^{\alpha}(\mathbf{r}) = \int_{MT^{\alpha}} \rho_{\alpha}(\mathbf{r}') G(\mathbf{r}, \mathbf{r}') d^3 r' - \frac{R_{\alpha}^2}{4\pi} \oint_{S^{\alpha}} V_I(\mathbf{r}') \frac{\partial G}{\partial n'} d\Omega' \quad (3.176)$$

The second integral is over the muffin-tin sphere boundary S^α , and it is necessary to satisfy the boundary conditions. The Green's function is given by:

$$G^\alpha(\mathbf{r}, \mathbf{r}') = 4\pi \sum_{l,m} \frac{Y_L(\hat{\mathbf{r}}') Y_L(\hat{\mathbf{r}})}{2l+1} \frac{r_{<}^l}{r_{>}^{l+1}} \left(1 - \left(\frac{r_{>}}{R_{MT^\alpha}} \right)^{2l+1} \right) \quad (3.177)$$

where $r_{>} = \max\{|\mathbf{r}|, |\mathbf{r}'|\}$, $r_{<} = \min\{|\mathbf{r}|, |\mathbf{r}'|\}$. Finally, the muffin-tin potential has to be expanded into lattice harmonics $K_\nu(\hat{\mathbf{r}})$.

$$V_{MT}^\alpha(\mathbf{r}) = \sum_\nu V_{MT,\nu}^\alpha(r) K_\nu(\hat{\mathbf{r}}) \quad (3.178)$$

The potential of the nuclei $V_i^\alpha(\mathbf{r}) = \frac{eZ_i^\alpha}{|\mathbf{r}|}$ is added to the spherical ($l=0$) component of the potential $V_{MT,0}^\alpha(r)$.

The muffin-tin potential is computed in the same way for both, bulk and film calculations. Apparently, the interstitial and the vacuum have to be treated differently in the two cases, due to the different boundary conditions and the different representation of the vacuum potential. Therefore, in the next two sections the solution of the Poisson equation will be outlined separately for these cases.

3.7.2 Determination of the interstitial Coulomb Potential in Bulk Calculations

In the case of bulk calculations we have periodic boundary conditions in three dimensions. Therefore, the solution of the Poisson equation,

$$\mathbf{G}^2 V(\mathbf{G}) = 4\pi \tilde{\rho}(\mathbf{G}) \quad (3.179)$$

is very simple. Obviously, this equation can only be solved, if $\tilde{\rho}(0) = 0$. Since $\tilde{\rho}(0)$ is the average charge density, this means, that charge neutrality is essential. Still, $V(0)$ remains undetermined by 3.179, i.e. one has the freedom to shift the potential by a constant. This is a consequence of the periodic boundary conditions, because they do not fix the reference of the potential. Usually $V(0)$ is chosen to be zero, hence the Coulomb potential in the interstitial-region is given by:

$$V_I(\mathbf{r}) = \sum_{\mathbf{G} \neq 0} \frac{4\pi \tilde{\rho}(\mathbf{G})}{\mathbf{G}^2} e^{i\mathbf{G}\mathbf{r}} = \sum_{s \neq 0} \frac{4\pi \tilde{\rho}_s}{\mathbf{G}_s^2} \Phi_s^{3D}(\mathbf{r}) \quad (3.180)$$

where the first summation is expressed in terms of G -vectors and the second in terms of stars.

3.7.3 Determination of the interstitial and vacuum Coulomb Potential in Film Calculations

In a film the translational symmetry in z -direction is lost. Accordingly, the boundary conditions are periodic in two dimensions only. In z -direction the periodic boundary

conditions are replaced by the requirement, that the potential approaches zero at infinity. The latter condition defines the absolute reference of the potential. As a consequence of the symmetry breaking, the following expansion of V and ρ is most suitable to solve the Poisson equation:

$$V(\mathbf{r}) = V_0(z) + \sum_{\mathbf{G}_{\parallel} \neq 0} V_{G_{\parallel}}(z) e^{i\mathbf{G}_{\parallel} \mathbf{r}} \quad (3.181)$$

$$\rho(\mathbf{r}) = \rho_0(z) + \sum_{\mathbf{G}_{\parallel} \neq 0} \rho_{G_{\parallel}}(z) e^{i\mathbf{G}_{\parallel} \mathbf{r}} \quad (3.182)$$

Substituting this into the Poisson equations yields:

$$\left(\frac{d^2}{dz^2} - G_{\parallel}^2 \right) V_{G_{\parallel}}(z) = -4\pi \rho_{G_{\parallel}}(z) \quad (3.183)$$

This equation is treated differently for $G_{\parallel} = 0$ and $G_{\parallel} \neq 0$.

The $G_{\parallel} = 0$ Component of the Potential

For the $G_{\parallel} = 0$ component of the potential the Poisson equation has the form

$$\frac{d^2}{dz^2} V_0(z) = -4\pi \rho_0(z) \quad (3.184)$$

The $G_{\parallel} = 0$ component of the pseudocharge density is given by:

$$\rho_0(z) = \begin{cases} \rho_I^{0,0} + \sum_{G_{\perp}} \rho_I^{0,G_{\perp}} e^{iG_{\perp} z} & |z| \leq \frac{D}{2} \\ \rho_V^0(z) & |z| > \frac{D}{2} \end{cases} \quad (3.185)$$

The Poisson equation for the $G_{\parallel} = 0$ can be integrated directly. The result in the vacuum region is given by:

$$V_V^0(z) = -4\pi \int_z^{\infty} \sigma_V(z') dz', \quad (3.186)$$

with

$$\sigma_V(z) = \int_{\frac{D}{2}}^z \rho_V^0(z') dz' + \bar{\rho}_I \frac{D}{2} \quad (3.187)$$

where the average interstitial charge density $\bar{\rho}_I$ is given by:

$$\bar{\rho}_I = \sum_{G_{\perp}} \rho_I^{0,G_{\perp}} j_0(G_{\perp} D). \quad (3.188)$$

Here $\bar{\rho}_I$ does not equal $\rho_I^{0,0}$, because the G_{\perp} are defined in terms of \tilde{D} rather than D , i.e. the period of the z -dependent planewaves does not equal the integration interval.

In the interstitial region the solution to (3.184) is

$$V_I^0(z) = -2\pi \rho_I^{0,0} \left(z^2 - \frac{D^2}{4} \right) - 4\pi \sum_{G_{\perp}} \frac{\rho_I^{0,G_{\perp}}}{G_{\perp}^2} \left(e^{iG_{\perp} z} - e^{iG_{\perp} \frac{D}{2}} \right) - 4\pi \int_{\frac{D}{2}}^{\infty} \sigma_V(z') dz' \quad (3.189)$$

The $G_{\parallel} \neq 0$ Component of the Potential

In the case $G_{\parallel} \neq 0$ the Poisson equation is solved via the Green's function method.

$$V_{G_{\parallel}}(z) = \int_{-\infty}^{\infty} \rho_{G_{\parallel}}(z) G_{G_{\parallel}}(z - z') dz' \quad (3.190)$$

Where the Green's function is given by:

$$G_{G_{\parallel}}(z - z') = \frac{2\pi}{G_{\parallel}} e^{|G_{\parallel}||z-z'|} \quad (3.191)$$

This leads to the following solution in the vacuum-region

$$\begin{aligned} V_V^{G_{\parallel}}(z) &= \frac{2\pi}{G_{\parallel}} e^{G_{\parallel}z} \int_{-\infty}^z \rho_V^{G_{\parallel}}(z') e^{-G_{\parallel}z'} dz' \\ &+ \frac{2\pi}{G_{\parallel}} e^{-G_{\parallel}z} \int_z^{-\frac{D}{2}} \rho_V^{G_{\parallel}}(z') e^{G_{\parallel}z'} dz' \\ &+ \frac{2\pi}{G_{\parallel}} e^{-G_{\parallel}z} \sum_{G_{\perp}} \frac{\rho_I^{G_{\parallel}, G_{\perp}}}{G_{\parallel} + iG_{\perp}} \left(e^{(G_{\parallel} + iG_{\perp})z} - e^{-(G_{\parallel} + iG_{\perp})z} \right) \end{aligned} \quad (3.192)$$

and in the interstitial-region

$$\begin{aligned} V_I^{G_{\parallel}}(z) &= 4\pi \sum_n \frac{\rho_I^{G_{\parallel}, G_{\perp}}}{G^2} e^{iG_{\perp}z} \\ &+ \frac{2\pi}{G_{\parallel}} \sum_{G_{\perp}} \frac{\rho_I^{G_{\parallel}, G_{\perp}}}{G^2} \left[e^{G_{\parallel}z} (G_{\parallel} + iG_{\perp}) e^{-(G_{\parallel} - iG_{\perp})\frac{D}{2}} \right. \\ &+ \left. e^{-G_{\parallel}z} (G_{\parallel} - iG_{\perp}) e^{-(G_{\parallel} + iG_{\perp})\frac{D}{2}} \right] + \\ &+ \frac{2\pi}{G_{\parallel}} \left[e^{G_{\parallel}z} \int_{-\frac{D}{2}}^{\infty} \rho_V^{G_{\parallel}}(z) e^{-G_{\parallel}z'} dz' + e^{-G_{\parallel}z} \int_{-\infty}^{\frac{D}{2}} \rho_V^{G_{\parallel}}(z) e^{G_{\parallel}z'} dz' \right] \end{aligned} \quad (3.193)$$

3.8 Computation of the Exchange Correlation Potential

The problem of the determination of the exchange correlation potential is quite different from the Coulomb potential. On one hand, V_{xc}^{σ} is a local quantity, i.e. $V_{xc}^{\sigma}(\mathbf{r})$ depends only on $n_{\uparrow}(\mathbf{r})$ and $n_{\downarrow}(\mathbf{r})$ at the same position \mathbf{r} . Thus, the muffin-tins, the interstitial- and vacuum-region can be treated independently. On the other hand, V_{xc}^{σ} and ϵ_{xc}^{σ} are non-linear functions of n_{\uparrow} and n_{\downarrow} . Therefore, V_{xc}^{σ} and ϵ_{xc}^{σ} have to be calculated in real space. V_{xc}^{σ} and ϵ_{xc}^{σ} are determined in the same way. First, n_{\uparrow} and n_{\downarrow} are transformed to real space, where V_{xc}^{σ} and ϵ_{xc}^{σ} are calculated. Then V_{xc}^{σ} and ϵ_{xc}^{σ} are back-transformed. Then, V_{xc}^{σ} is added to the Coulomb potential, yielding the spin-dependent potential V_{\uparrow} and V_{\downarrow} . ϵ_{xc}^{σ} is needed for the determination of the total energy.

3.8.1 Calculation of ϵ_{xc}^σ and V_{xc}^σ in the Interstitial-Region

In the interstitial-region the charge density is expanded into three-dimensional stars with coefficients n_s^σ . Multiplying these by $e^{i\mathbf{R}\mathbf{G}\boldsymbol{\tau}}$ yields the planewave coefficients n_G^σ . If the space group is symmorphic the star and planewave coefficients are identical. However, due to numerical inaccuracy, the calculated coefficients of symmetry equivalent planewaves are not exactly equal, and the corresponding star coefficient is obtained from the average of the planewave coefficients. In the next step a three-dimensional Fast-Fourier transform is carried out. Then the exchange correlation potential is calculated on a real space mesh \mathbf{r}_i . Finally, V_{xc}^σ is back-transformed, and the star coefficients are computed.

$$n_s^\sigma \longrightarrow n_G^\sigma \xrightarrow{FFT} n^\sigma(\mathbf{r}_i) \longrightarrow V_{xc}^\sigma(\mathbf{r}_i) \xrightarrow{FFT^{-1}} V_{xc}^{\sigma,G} \longrightarrow V_{xc}^{\sigma,s}.$$

3.8.2 Calculation of ϵ_{xc}^σ and V_{xc}^σ in the Vacuum-Region

The vacuum charge density is stored in terms of two-dimensional stars and a z -dependent exponential mesh z_i . The $G_{\parallel} = 0$ component reaches further into the vacuum than the $G_{\parallel} \neq 0$ components. In the so called warping region the planewave coefficients on each mesh point are determined by a multiplication with the phase factor $e^{i\mathbf{R}\mathbf{G}_{\parallel}\boldsymbol{\tau}}$. Then, for each grid point z_i along the z -axis, the two-dimensional charge density is Fourier transformed to a real space grid $(\mathbf{r}_{\parallel}, z_i)$, where V_{xc}^σ is calculated. Afterwards, V_{xc}^σ is back-transformed and the star coefficients are computed.

$$\begin{aligned} n^\sigma(\Phi_s^{2D}, z_i) &\longrightarrow n^\sigma(\mathbf{G}_{\parallel}, z_i) \xrightarrow{2DFFT} n^\sigma(\mathbf{r}_{\parallel}, z_i) \longrightarrow V_{xc}^\sigma(\mathbf{r}_{\parallel}, z_i) \\ &\xrightarrow{2DFFT^{-1}} V_{xc}^\sigma(\mathbf{G}_{\parallel}, z_i) \longrightarrow V_{xc}^\sigma(\Phi_s^{2D}, z_i) \end{aligned}$$

Beyond the warping region the exchange correlation potential is calculated directly on the z -dependent mesh.

3.8.3 Calculation of ϵ_{xc}^σ and V_{xc}^σ in the Muffin-Tin Spheres

The muffin-tin charge is expanded into lattice harmonics and radial functions. The radial functions are stored on a discrete real-space mesh. Thus, the transform to real space affects only the angular part. The charge density is calculated on a set of special angular points $\hat{\mathbf{r}}_i = (\theta_i, \phi_i)$. Again, the exchange correlation potential is calculated in real space. Thereafter, the result $V_{xc}^\sigma(\mathbf{r})$ is expanded into spherical harmonics Y_L . The Y_L are orthonormal, therefore the coefficients can be obtained from

$$v_{xc,L}^\sigma(r) = \int Y_L(\hat{\mathbf{r}}) V_{xc}^\sigma(r, \hat{\mathbf{r}}) d\Omega. \quad (3.194)$$

The choice of the points $\hat{\mathbf{r}}_i = (\theta_i, \phi_i)$, on which $n^\sigma(\mathbf{r})$ and $V_{xc}^\sigma(\mathbf{r})$ are calculated, depends on the integration method, that is used to perform the angular integration. In the current implementation (3.194) is computed via a Gauß-Legendre integration and the angular points are chosen such, that the orthonormality condition of the Y_L holds also for the angular mesh $\hat{\mathbf{r}}_i$.

3.9 Minimization of the Energy Functional

The aim of electronic structure calculations is to minimize the energy functional with respect to the electron density. Within density functional theory this minimization is performed implicitly, by the determination of a selfconsistent density $n(\mathbf{r})$. In the previous sections we described, how an effective Potential can be calculated from a charge density, how the Kohn-Sham equations including this potential can be solved and how a new electron density can be calculated from the resulting single particle wavefunctions. Combining these steps defines a map:

$$n'(\mathbf{r}) = F\{n(\mathbf{r})\} \quad (3.195)$$

The electron density that minimizes the energy functional $n_0(\mathbf{r})$ is a fix-point of $F\{n(\mathbf{r})\}$, i.e. it solves

$$\mathcal{F}\{n_0(\mathbf{r})\} = 0, \quad \text{with } \mathcal{F}\{n(\mathbf{r})\} = F\{n(\mathbf{r})\} - n(\mathbf{r}). \quad (3.196)$$

The density is expanded into a large set of basis functions. Therefore, in actual calculations, the charge density is a coefficient vector of dimension n , where n is typically of the order of 10^4 . Thus, (3.196) constitutes a system of n nonlinear equations, which can be solved by iteration:

$$n^{m+1}(\mathbf{r}) = F\{n^m(\mathbf{r})\} \quad (3.197)$$

A starting density can be constructed by a superposition of atomic densities. However, this scheme is in general divergent. To achieve convergence the output density has to be mixed with the input density. Different mixing schemes are discussed in the following.

3.9.1 “simple mixing”

The slowest method is the “simple mixing”, which converges only linearly.

$$\frac{|\delta n^{(m+1)}|}{|\delta n^{(m)}|} \leq \text{const.} \quad (3.198)$$

Where $\delta n^{(m)}$ is the difference of the density of the m^{th} iteration and the unknown fix-point, $\delta n^{(m)} = n^{(m)} - n_0$. The density for the next iteration is constructed as a linear combination of $n^{(m)}$ and $F\{n^m\}$ according to:

$$\begin{aligned} n^{(m+1)} &= (1 - \alpha)n^{(m)} + \alpha F\{n^m\} \\ &= n^{(m)} + \alpha \mathcal{F}\{n^{(m)}\} \end{aligned} \quad (3.199)$$

α is the so-called mixing parameter. If it is chosen small enough the iteration converges and is very stable. In spin-polarized calculations different mixing parameters can be used for the charge and the magnetization density. Usually, the spin mixing parameter can be chosen far larger than the parameter for the charge density. However, for the type of systems we are interested in α is very small, requiring many hundreds of iterations.

3.9.2 The Newton-Raphson Method

In the Newton-Raphson method the functional $\mathcal{F}\{n\}$ is linearized around the approximate solution $n^{(m)}$.

$$\mathcal{F}\{n\} \approx \mathcal{F}\{n^{(m)}\} + \mathcal{J}\{n^{(m)}\}(n - n^{(m)}) \quad (3.200)$$

Where the Jacobian is defined by:

$$\mathcal{J}\{n^{(m)}(\mathbf{r})\} = \left. \frac{\partial \mathcal{F}\{n(\mathbf{r})\}}{\partial n(\mathbf{r}')} \right|_{n^{(m)}(\mathbf{r})} \quad (3.201)$$

In actual calculations the Jacobian is a $n \times n$ matrix. Similar to the well known Newton method for one dimensional functions, the next approximation to n_0 , $n^{(m+1)}$, is determined from the requirement, that the linearized functional in (3.200) vanishes at $n^{(m+1)}$. Thus, $n^{(m+1)}$ is given by:

$$n^{(m+1)} = n^{(m)} - [\mathcal{J}\{n^{(m)}\}]^{-1} \mathcal{F}\{n^{(m)}\} \quad (3.202)$$

The Newton-Raphson method converges quadratically:

$$\frac{|\delta n^{(m+1)}|}{|\delta n^{(m)}|^2} \leq \text{const.} \quad (3.203)$$

The major drawback of this method is the difficulty to evaluate the Jacobian. Even if the functional $\mathcal{F}\{n\}$ was known, the evaluation would be cumbersome due to the enormous size of $\mathcal{J}\{n\}$. In addition, the Jacobian has to be inverted where the amount of calculation scales with cube of the dimension. A further problem is that the convergence radius is rather small so that the method can only be used if $n^{(m)}$ is already very close to n_0 .

3.9.3 Quasi-Newton Methods

With the development of the Quasi-Newton methods it became possible to exploit the advantages of the Newton-Raphson method, i.e. to make use of the information that is contained in the Jacobian, for problems where the Jacobian cannot be calculated or its determination is too demanding. Rather than computing the Jacobian each iteration, an approximate Jacobian is set up and improved iteration by iteration. From the linearization of $\mathcal{F}\{n\}$ (3.200) we find the following condition for the Jacobian, which is usually called Quasi-Newton condition:

$$\Delta n^{(m)} = [\mathcal{J}^{(m)}]^{-1} \Delta \mathcal{F}^{(m)} \quad (3.204)$$

$$\Delta n^{(m)} = n^{(m)} - n^{(m-1)}, \quad \Delta \mathcal{F}^{(m)} = \mathcal{F}\{n^{(m)}\} - \mathcal{F}\{n^{(m-1)}\}$$

Quasi-Newton methods converge super-linearly

$$\frac{|\delta n^{(m+1)}|}{|\delta n^{(m)}|} \rightarrow 0,$$

and have a larger convergence radius than the Newton-Raphson method. Since the Jacobian is build up iteration by iteration, the “history” of the previous iterations is memorized in \mathcal{J} , whereas the Jacobian of the Newton-Raphson method depends only on the previous iteration. In this sense the Newton-Raphson method is self-corrective [Blü88], it “forgets” inadequately chosen corrections. The Quasi-Newton methods sometimes need to be restarted, if the iteration converges only slowly. This can happen if the starting density is very far from n_0 or when physical or numerical parameters that affect the calculations are changed during the iteration. Equation (3.204) does not determine the Jacobian uniquely, instead (3.204) constitutes a system of n equations for n^2 unknowns. The various Quasi-Newton schemes differ by the ansatz how the new information is used to build the inverse Jacobian. The methods that are implemented in the FLAPW code are discussed in [Pen96].

Chapter 4

Non-Collinear Magnetism in FLAPW

The implementation of the FLAPW method, outlined in the previous chapter, assumes collinear magnetism, i.e. the magnetization density has to be directed along the z-axis everywhere in space. In this case, the Hamiltonian of the Schrödinger-Pauli equation 2.18, which in general constitutes a two by two matrix, becomes diagonal in the two spin-components. In fact, one can think of the magnetization to be directed along any direction, since real space and spin space are completely decoupled within the scalar-relativistic approximation. The z-axis is only chosen because of the simple form of the Pauli matrix σ_z . Another important simplification, that reduces the expense of calculations, is the fact, that the Hamiltonian and the overlap matrix become real symmetric instead of complex hermitian, if the system possesses inversion symmetry. Finally, only the magnitude of the magnetization density needs to be store. In fact, the particle and magnetization density, n and m can be replaced by a spin-up and -down density, n_\uparrow and n_\downarrow . In the same way V and B can be replaced by V_\uparrow and V_\downarrow .

In the case of general non-collinear magnetism, all the simplifications listed above are lost. A B -field with non-zero x- and y-component means, that the Hamiltonian contains terms including σ_x and σ_y . Thus, the spin-up and -down components of the wavefunctions are no longer decoupled, leading to an eigenvalue problem twice as large as before. In addition, the Hamiltonian becomes explicitly complex, due to the presents of σ_y .

A large amount of work in the field of selfconsistent *ab-initio* calculations on non-collinear magnetic systems has been done by Kübler and coworkers [SHK89, Küb95, SK96] and references therein. Many aspects of non-collinear magnetism can be described within the picture of inter-atomic non-collinear magnetism, where it is the different atomic moments, which are non-collinear. Thus, the magnetization at each atom is predominantly directed along one particular direction, which differs from atom to atom, but deviations from this direction on the intra-atomic scale are expected to be small. Within FLAPW this can be realized assigning different quan-

tization axis to each atom, and allowing the magnetization inside the corresponding muffin-tin to be directed along this axis only. Still, in the interstitial- and vacuum-region one has to deal with a general non-collinear magnetization.

4.1 The Frozen Potential Approximation

The frozen potential approximation allows the calculation of the total energy difference of (similar) systems, based on the eigenvalue sums of non-selfconsistent calculations. In this section we will explain how this method can be employed to estimate the energy difference of different magnetic configurations. In the spirit of the approximations outlined above, these configurations shall differ, in that the directions of the magnetization at each atom, i.e. inside each muffin-tin, are different. Let's consider two configurations, denoted a and b . According to (2.28) the total energy of each of them is given by

$$\begin{aligned}
E[n, \mathbf{m}] &= \sum_{i=1}^N \epsilon_i - \int n(\mathbf{r}) V_{xc}(\mathbf{r}) d^3 r - \int \mathbf{m}(\mathbf{r}) \cdot \mathbf{B}_{xc}(\mathbf{r}) d^3 r \\
&- \frac{1}{2} 4\pi e^2 \int \frac{n(\mathbf{r})n(\mathbf{r}')}{|\mathbf{r} - \mathbf{r}'|} d^3 r d^3 r' \\
&+ \int n(\mathbf{r}) \epsilon_{xc}(n(\mathbf{r}), |\mathbf{m}(\mathbf{r})|) d^3 r + 4\pi e^2 \sum_{\substack{\mu, \mu'=1 \\ \mu \neq \mu'}}^M \frac{Z^\mu Z^{\mu'}}{|\boldsymbol{\tau}^\mu - \boldsymbol{\tau}^{\mu'}|}. \quad (4.1)
\end{aligned}$$

Let us assume now, that the difference of the electron density between the two configurations is negligible $n^a(\mathbf{r}) \approx n^b(\mathbf{r})$, i.e. that a and b differ only by their magnetization. As a consequence, the Hartree energy of a and b is the same. Clearly, the Madelung energy does not change too. Hence, the energy difference is given by

$$\begin{aligned}
E[n^a, \mathbf{m}^b] - E[n^b, \mathbf{m}^b] &= \sum_{i=1}^N \epsilon_i^a - \sum_{i=1}^N \epsilon_i^b \\
&- \int n^a(\mathbf{r}) V_{xc}^a(\mathbf{r}) + \mathbf{m}^a(\mathbf{r}) \cdot \mathbf{B}_{xc}^a(\mathbf{r}) - n^b(\mathbf{r}) V_{xc}^b(\mathbf{r}) - \mathbf{m}^b(\mathbf{r}) \cdot \mathbf{B}_{xc}^b(\mathbf{r}) d^3 r \\
&+ \int n^a(\mathbf{r}) \epsilon_{xc}(n^a(\mathbf{r}), |\mathbf{m}^a(\mathbf{r})|) - n^b(\mathbf{r}) \epsilon_{xc}(n^b(\mathbf{r}), |\mathbf{m}^b(\mathbf{r})|) d^3 r. \quad (4.2)
\end{aligned}$$

From the local character of ϵ_{xc} within the LSDA follows that V_{xc} and ϵ_{xc} depend only on the magnitude of the magnetization $m(\mathbf{r}) = |\mathbf{m}(\mathbf{r})|$. As a result, the magnetic field \mathbf{B}_{xc} is always parallel to the magnetization, with its magnitude also depending on $m(\mathbf{r})$ only. Hence, 4.2 becomes

$$\begin{aligned}
E[n^a, \mathbf{m}^b] - E[n^b, \mathbf{m}^b] &= \sum_{i=1}^N \epsilon_i^a - \sum_{i=1}^N \epsilon_i^b \\
&- \int n^a(\mathbf{r}) V_{xc}(n^a(\mathbf{r}), m^a(\mathbf{r})) + m^a(\mathbf{r}) B_{xc}(n^a(\mathbf{r}), m^a(\mathbf{r}))
\end{aligned}$$

$$\begin{aligned}
& -n^b(\mathbf{r})V_{xc}(n^b(\mathbf{r}), m^b(\mathbf{r})) - m^b(\mathbf{r})B_{xc}(n^b(\mathbf{r}), m^b(\mathbf{r}))d^3r \\
& + \int n^a(\mathbf{r})\epsilon_{xc}(n^a(\mathbf{r}), m^a(\mathbf{r})) - n^b(\mathbf{r})\epsilon_{xc}(n^b(\mathbf{r}), m^b(\mathbf{r}))d^3r.
\end{aligned} \tag{4.3}$$

At this point, the second approximation comes into play. We assume, that the magnitude of the magnetization inside the muffin-tins does not change with the direction. Under this assumption, the contributions from the muffin-tin spheres to the two integrals in 4.3 cancel out exactly. This is a good approximation for the systems we are going to apply this theory to. Blügel et al. [BDZD89] investigated the properties of 3d transition-metal monolayers on Ag(001) and unsupported monolayers (UML) with the same geometry. They compared the ferromagnetic with the c(2 × 2) anti-ferromagnetic structure, and found that the magnetic moments of Mn and Fe hardly change, whereas the moments of Cr change noticeably but not drastically. Assuming the validity of this approximation, the only error terms, that add to the difference of the eigenvalue sums, is due to the change of the magnitude of the magnetization in the interstitial- and vacuum-region.

$$\begin{aligned}
E[n^a, \mathbf{m}^b] - E[n^b, \mathbf{m}^b] &= \sum_{i=1}^N \epsilon_i^a - \sum_{i=1}^N \epsilon_i^b \\
& - \int_{I+V} n^a(\mathbf{r})V_{xc}(n^a(\mathbf{r}), m^a(\mathbf{r})) + m^a(\mathbf{r})B_{xc}(n^a(\mathbf{r}), m^a(\mathbf{r})) \\
& \quad - n^b(\mathbf{r})V_{xc}(n^b(\mathbf{r}), m^b(\mathbf{r})) - m^b(\mathbf{r})B_{xc}(n^b(\mathbf{r}), m^b(\mathbf{r}))d^3r \\
& + \int_{I+V} n^a(\mathbf{r})\epsilon_{xc}(n^a(\mathbf{r}), m^a(\mathbf{r})) - n^b(\mathbf{r})\epsilon_{xc}(n^b(\mathbf{r}), m^b(\mathbf{r}))d^3r
\end{aligned} \tag{4.4}$$

However, the magnetization of the interstitial- and vacuum-region are small, and the magnitudes differ only in a small region of space between the atoms. Therefore, the contribution from the integrals in 4.4 can be neglected, and the difference of the total energy of two magnetic configurations can be approximated by the difference of the eigenvalue sums.

$$E[n^a, \mathbf{m}^b] - E[n^b, \mathbf{m}^b] \approx \sum_{i=1}^N \epsilon_i^a - \sum_{i=1}^N \epsilon_i^b \tag{4.5}$$

The benefit of the frozen potential approximation is, that once one magnetic configuration has been calculated selfconsistently, the energy of other configurations can be obtained from non-selfconsistent calculations. The input electron and magnetization density for the latter is being obtained from the densities of the selfconsistent calculation, by a rotation of the direction of magnetization inside the muffin-tins. In practice, these calculations are carried out in two steps:

- Perform a selfconsistent collinear calculation
- Determine the energy difference to other (non-collinear) magnetic configurations via the frozen potential approximation.

Clearly, this is a great simplification, compared to selfconsistent non-collinear calculations, because no vector-magnetization densities have to be generated or stored

and no exchange correlation potentials and magnetic fields have to be computed from such densities.

Still, one problem remains to be solved. Obviously, the Hamiltonian, i.e. V_{eff} and \mathbf{B}_{eff} , is needed in order to calculate the eigenvalues. Let's consider the situation, where the magnetic configuration a has been calculated selfconsistently. Of course, in this case, V_{eff}^a and \mathbf{B}_{eff}^a are known, but V_{eff}^b and \mathbf{B}_{eff}^b are not. Assuming the validity of the approximations made above, i.e. that $n^a(\mathbf{r}) \approx n^b(\mathbf{r})$ and that \mathbf{B}_{xc}^b inside the muffin-tins can be obtained from a rotation of \mathbf{B}_{xc}^a , only the exchange correlation potential and magnetic field in the interstitial- and vacuum-region, $V_{xc}^{IV,b}$ and $\mathbf{B}_{xc}^{IV,b}$, remain unknown. An approximate Hamiltonian $\tilde{\mathcal{H}}^b$ can be constructed using $V_{xc}^{IV,a}$ and $\mathbf{B}_{xc}^{IV,a}$ instead. The unknown exact Hamiltonian \mathcal{H}^b is related to $\tilde{\mathcal{H}}^b$ by:

$$\tilde{\mathcal{H}}^b = \mathcal{H}^b + (V_{xc}^{IV,a} + \boldsymbol{\sigma} \cdot \mathbf{B}_{xc}^{IV,a} - V_{xc}^{IV,b} - \boldsymbol{\sigma} \cdot \mathbf{B}_{xc}^{IV,b}) \quad (4.6)$$

Now, the error of the eigenvalues $\Delta\epsilon_i^b = \tilde{\epsilon}_i^b - \epsilon_i^b$ can be determined using first order perturbation theory. Since V_{xc} depends only weakly on the magnetization, it can be neglected here. Thus, we have

$$\Delta\epsilon_i^b = \langle \psi_i^b | \boldsymbol{\sigma} \cdot (\mathbf{B}_{xc}^{IV,a} - \mathbf{B}_{xc}^{IV,b}) | \psi_i^b \rangle. \quad (4.7)$$

Summing over the occupied states yields

$$\sum_{i=1}^N \Delta\epsilon_i^b = \int_{I+V} \mathbf{m}^b \cdot (\mathbf{B}_{xc}^{IV,a} - \mathbf{B}_{xc}^{IV,b}) d^3r. \quad (4.8)$$

This error term causes some difficulties. Of course, the interstitial and vacuum magnetization and magnetic field is small, but in contrast to the error term in 4.3, which depend on the magnitudes of \mathbf{m} and \mathbf{B} , here the error depend on the difference of the vectors $\mathbf{B}_{xc}^{IV,a} - \mathbf{B}_{xc}^{IV,b}$. Consider for example the case, where a is the ferromagnetic and b is the antiferromagnetic configuration. Apparently, in one half of the interstitial region the magnetizations and magnetic fields are opposite to each other, while the magnitudes are similar. If we used the selfconsistent ferromagnetic B -field, to construct the approximate antiferromagnetic Hamiltonian, it would favor the ferromagnetic solution, i.e. the ferromagnetic eigenvalue sum would be lowered compared to the antiferromagnetic and vice versa.

A solution to this problem is to set the interstitial and vacuum magnetic field to zero when constructing the trial Hamiltonian. Then the error term 4.8 reduces to

$$\sum_{i=1}^N \Delta\epsilon_i^b = - \int_{I+V} \mathbf{m}^b \cdot \mathbf{B}_{xc}^{IV,b} d^3r. \quad (4.9)$$

Now, we can make use of the fact, that \mathbf{m}^b and $\mathbf{B}_{xc}^{IV,b}$ are always parallel. Ergo, the unknown exact eigenvalue sum is related to the approximate sum by

$$\sum_{i=1}^N \epsilon_i^b = \sum_{i=1}^N \tilde{\epsilon}_i^b - \int_{I+V} m^b B_{xc}^{IV,b} d^3r. \quad (4.10)$$

If we perform this approximation for the two systems, a and b, that we want to compare, the difference of the two eigenvalue sums is given by

$$\sum_{i=1}^N \epsilon_i^a - \sum_{i=1}^N \epsilon_i^b = \sum_{i=1}^N \tilde{\epsilon}_i^a - \sum_{i=1}^N \tilde{\epsilon}_i^b - \int_{I+V} (m^a B_{xc}^{IV,a} - m^b B_{xc}^{IV,b}) d^3 r. \quad (4.11)$$

Hence, the error we are left with depends only on the magnitudes of \mathbf{m} and \mathbf{B} . In fact, it is exactly the same term, that appeared already in 4.4, and it can be neglected. Eventually, the application of the frozen potential approximation has to be supplemented by a third step, the elimination of the interstitial and vacuum magnetic field.

4.2 The Implementation of Non-Collinear Magnetism

In this section we will explain, how the Hamiltonian matrix corresponding to the approximate Hamiltonian $\tilde{\mathcal{H}}$, with the B -field inside the muffin-tin spheres rotated by a arbitrary angle, can be set up. Since spin- and real-space are completely decoupled within the scalar-relativistic approximations, the spin-rotations can be performed without any effect on the real-space coordinates. It will be shown, that no changes to the construction of the muffin-tin basis functions or the determination of the t-matrix are necessary in order to set up $\tilde{\mathcal{H}}$.

The potential and the magnetic field are represented in terms of $V_{\uparrow}(\mathbf{r})$ and $V_{\downarrow}(\mathbf{r})$, where up and down is defined in terms of the global z-axis before the rotation. Performing the rotation leaves both, $V_{\uparrow}(\mathbf{r})$ and $V_{\downarrow}(\mathbf{r})$, unchanged. In particular, no rotation needs to be applied to \mathbf{r} . The only change is, that now spin-up and -down is to be interpreted in terms of a local quantization axis. Therefore, a local spin-space coordinate frame S^α is introduced for each atom type (muffin-tin). The global spin-coordinate frame S^g can be transformed into the local frame by a rotation, given by the Euler angles $(\alpha, \beta, 0)$. In this case, the Euler angles are equivalent to the polar angles of the local quantization axis in the global frame, $\alpha = \varphi$, $\beta = \vartheta$. Thus, the basis vectors of the two frames are related to each other by

$$\mathbf{R}(\alpha, \beta, 0) \hat{\mathbf{e}}_i^g = \hat{\mathbf{e}}_i^\alpha, \quad (4.12)$$

and the magnetization density and the magnetic field, seen from the global frame, $\mathbf{m}^{\alpha g}(\mathbf{r})$ and $\mathbf{B}^{\alpha g}(\mathbf{r})$, are related to the same quantities seen from the local frame by

$$\begin{aligned} \mathbf{m}^{\alpha g}(\mathbf{r}) &= \mathbf{R}(\alpha, \beta, 0) \mathbf{m}^{\alpha l}(\mathbf{r}) \\ \mathbf{B}^{\alpha g}(\mathbf{r}) &= \mathbf{R}(\alpha, \beta, 0) \mathbf{B}^{\alpha l}(\mathbf{r}). \end{aligned} \quad (4.13)$$

where the index α indicates, that this corresponds to quantities inside the muffin-tin of atom type α . The Pauli spinors transform according to

$$\chi^{\alpha g} = \mathbf{U}^{(2)}(\alpha, \beta, 0) \chi^{\alpha l}, \quad (4.14)$$

with

$$\mathbf{U}^{(2)}(\alpha, \beta, 0) = \begin{pmatrix} e^{-\frac{i\alpha}{2}} \cos(\frac{\beta}{2}) & -e^{-\frac{i\alpha}{2}} \sin(\frac{\beta}{2}) \\ e^{\frac{i\alpha}{2}} \sin(\frac{\beta}{2}) & e^{\frac{i\alpha}{2}} \cos(\frac{\beta}{2}) \end{pmatrix}. \quad (4.15)$$

The unitary matrix $\mathbf{U}^{(2)}$ is derived in most standard textbooks [OH93]. In the collinear case the radial functions $u_{l\sigma}^\alpha$ and $\dot{u}_{l\sigma}^\alpha$ ¹ are determined as solutions to the radial Schrödinger (scalar-relativistic) equation 3.2 (3.41), including the spin-dependent potential V_σ . Thus, the basis functions inside the muffin-tins are linear combinations of

$$\begin{aligned} u_{l\uparrow}^\alpha(r) Y_L(\hat{\mathbf{r}}) \chi_{\uparrow}^\alpha, & \quad \dot{u}_{l\uparrow}^\alpha(r) Y_L(\hat{\mathbf{r}}) \chi_{\uparrow}^\alpha, \\ u_{l\downarrow}^\alpha(r) Y_L(\hat{\mathbf{r}}) \chi_{\downarrow}^\alpha, & \quad \dot{u}_{l\downarrow}^\alpha(r) Y_L(\hat{\mathbf{r}}) \chi_{\downarrow}^\alpha, \end{aligned} \quad (4.16)$$

where L abbreviates lm , and

$$\chi_{\uparrow}^{\alpha g} = \chi_{\uparrow}^{\alpha l} = \chi_{\uparrow}^\alpha = \begin{pmatrix} 1 \\ 0 \end{pmatrix}, \quad \chi_{\downarrow}^{\alpha g} = \chi_{\downarrow}^{\alpha l} = \chi_{\downarrow}^\alpha = \begin{pmatrix} 0 \\ 1 \end{pmatrix}. \quad (4.17)$$

Afterwards, the spin-dependent t -matrices (3.61 – 3.64) are calculated. This whole procedure remains completely unchanged in the non-collinear case, with the only difference, that spin-up and -down means up and down in terms of the local quantization axis. Consequently, the muffin-tin basis set becomes

$$\begin{aligned} u_{l\uparrow}^\alpha(r) Y_L(\hat{\mathbf{r}}) \chi_{\uparrow}^{\alpha g}, & \quad \dot{u}_{l\uparrow}^\alpha(r) Y_L(\hat{\mathbf{r}}) \chi_{\uparrow}^{\alpha g}, \\ u_{l\downarrow}^\alpha(r) Y_L(\hat{\mathbf{r}}) \chi_{\downarrow}^{\alpha g}, & \quad \dot{u}_{l\downarrow}^\alpha(r) Y_L(\hat{\mathbf{r}}) \chi_{\downarrow}^{\alpha g}, \end{aligned} \quad (4.18)$$

with

$$\chi_{\uparrow}^{\alpha g} = \mathbf{U}^{(2)} \chi_{\uparrow}^{\alpha l} = \begin{pmatrix} e^{-\frac{i\alpha}{2}} \cos(\frac{\beta}{2}) \\ e^{\frac{i\alpha}{2}} \sin(\frac{\beta}{2}) \end{pmatrix}, \quad \chi_{\downarrow}^{\alpha g} = \mathbf{U}^{(2)} \chi_{\downarrow}^{\alpha l} = \begin{pmatrix} -e^{-\frac{i\alpha}{2}} \sin(\frac{\beta}{2}) \\ e^{\frac{i\alpha}{2}} \cos(\frac{\beta}{2}) \end{pmatrix}. \quad (4.19)$$

The next step is to connect the planewaves, representing the basis functions in the interstitial region, to the muffin-tin basis, with the aim to form a set of continuous and differentiable basis functions. In the collinear case the planewaves with spin σ are connected to the muffin-tin basis functions with the same spin only. Hence, the boundary conditions that have to be satisfied on the muffin-tin sphere are:

$$e^{i(\mathbf{k}+\mathbf{G})\mathbf{r}} \chi_\sigma = \sum_L \left(A_{L\sigma}^{\mu\mathbf{G}}(\mathbf{k}) u_{l\sigma}^\alpha(r) + B_{L\sigma}^{\mu\mathbf{G}}(\mathbf{k}) \dot{u}_{l\sigma}^\alpha(r) \right) Y_L(\hat{\mathbf{r}}) \chi_\sigma \quad (4.20)$$

In the non-collinear case each function in the interstitial couples to both, spin-up and -down, in the muffin-tins. Therefore, the boundary conditions become:

$$e^{i(\mathbf{k}+\mathbf{G})\mathbf{r}} \chi_\sigma = \sum_{\sigma^\alpha} \sum_L \left(A_{L\sigma\sigma^\alpha}^{\mu\mathbf{G}}(\mathbf{k}) u_{l\sigma^\alpha}^\alpha(r) + B_{L\sigma\sigma^\alpha}^{\mu\mathbf{G}}(\mathbf{k}) \dot{u}_{l\sigma^\alpha}^\alpha(r) \right) Y_L(\hat{\mathbf{r}}) \chi_{\sigma^\alpha}^{\alpha g} \quad (4.21)$$

¹The radial functions are denoted u only for convenience. In the actual calculations the scalar-relativistic approximation is employed, and therefore the large component of the radial function is used here.

In order to calculate the A - and B -coefficients, we multiply equation 4.21 with $(\chi_{\uparrow}^{\alpha g})^*$ or $(\chi_{\downarrow}^{\alpha g})^*$, which yields

$$e^{i(\mathbf{k}+\mathbf{G})\mathbf{r}}(\chi_{\sigma\alpha}^{\alpha g})^* \chi_{\sigma} = \sum_L \left(A_{L\sigma\sigma\alpha}^{\mu\mathbf{G}}(\mathbf{k}) u_{l\sigma\alpha}^{\alpha}(r) + B_{L\sigma\sigma\alpha}^{\mu\mathbf{G}}(\mathbf{k}) \dot{u}_{l\sigma\alpha}^{\alpha}(r) \right) Y_L(\hat{\mathbf{r}}). \quad (4.22)$$

Comparing this equation with 4.20 shows, that the non-collinear A - and B -coefficients can be expressed in terms of the collinear coefficients.

$$\begin{aligned} A_{L\sigma\sigma\alpha}^{\mu\mathbf{G}}(\mathbf{k}) &= (\chi_{\sigma\alpha}^{\alpha g})^* \chi_{\sigma} A_{L\sigma\alpha}^{\mu\mathbf{G}}(\mathbf{k}) \\ B_{L\sigma\sigma\alpha}^{\mu\mathbf{G}}(\mathbf{k}) &= (\chi_{\sigma\alpha}^{\alpha g})^* \chi_{\sigma} B_{L\sigma\alpha}^{\mu\mathbf{G}}(\mathbf{k}) \end{aligned} \quad (4.23)$$

Similarly, the contribution of the muffin-tin at atom μ $H_{MT^{\mu}}^{\mathbf{G}'\sigma'\mathbf{G}\sigma}(\mathbf{k})$ to the non-collinear Hamiltonian $H^{\mathbf{G}'\sigma'\mathbf{G}\sigma}(\mathbf{k})$ can be expressed in term of the muffin-tin contribution $H_{MT^{\mu}\sigma}^{\mathbf{G}'\mathbf{G}}(\mathbf{k})$ to the collinear spin-dependent Hamiltonian $H_{\sigma}^{\mathbf{G}'\mathbf{G}}(\mathbf{k})$.

$$\begin{aligned} H_{MT^{\mu}\sigma}^{\mathbf{G}'\mathbf{G}}(\mathbf{k}) &= \int_{MT^{\mu}} \left(\sum_{L'} \left(A_{L'\sigma}^{\mu\mathbf{G}'}(\mathbf{k}) u_{l'\sigma}^{\alpha}(r) + B_{L'\sigma}^{\mu\mathbf{G}'}(\mathbf{k}) \dot{u}_{l'\sigma}^{\alpha}(r) \right) Y_L(\hat{\mathbf{r}}) \chi_{\sigma} \right)^* \mathcal{H}_{MT^{\mu}\sigma} \\ &\quad \left(\sum_L \left(A_{L\sigma}^{\mu\mathbf{G}}(\mathbf{k}) u_{l\sigma}^{\alpha}(r) + B_{L\sigma}^{\mu\mathbf{G}}(\mathbf{k}) \dot{u}_{l\sigma}^{\alpha}(r) \right) Y_L(\hat{\mathbf{r}}) \chi_{\sigma} \right) d^3r \end{aligned} \quad (4.24)$$

In the non-collinear case an additional summation over the local spin σ^{α} has to be performed.

$$\begin{aligned} H_{MT^{\mu}}^{\mathbf{G}'\sigma'\mathbf{G}\sigma}(\mathbf{k}) &= \\ \int_{MT^{\mu}} \left(\sum_{\sigma^{\alpha}} \sum_{L'} \left(A_{L'\sigma'\sigma^{\alpha}}^{\mu\mathbf{G}'}(\mathbf{k}) u_{l'\sigma^{\alpha}}^{\alpha}(r) + B_{L'\sigma'\sigma^{\alpha}}^{\mu\mathbf{G}'}(\mathbf{k}) \dot{u}_{l'\sigma^{\alpha}}^{\alpha}(r) \right) Y_L'(\hat{\mathbf{r}}) \chi_{\sigma^{\alpha}}^{\alpha g} \right)^* &\mathcal{H}_{MT^{\mu}} \\ \left(\sum_{\sigma^{\alpha}} \sum_L \left(A_{L\sigma\sigma^{\alpha}}^{\mu\mathbf{G}}(\mathbf{k}) u_{l\sigma^{\alpha}}^{\alpha}(r) + B_{L\sigma\sigma^{\alpha}}^{\mu\mathbf{G}}(\mathbf{k}) \dot{u}_{l\sigma^{\alpha}}^{\alpha}(r) \right) Y_L(\hat{\mathbf{r}}) \chi_{\sigma^{\alpha}}^{\alpha g} \right) &d^3r \end{aligned} \quad (4.25)$$

However, $\mathcal{H}_{MT^{\mu}}$ is diagonal in $\chi_{\sigma^{\alpha}}^{\alpha g}$, and $(\chi_{\sigma^{\alpha}}^{\alpha g})^* \chi_{\sigma^{\alpha}}^{\alpha g} = \delta_{\sigma^{\alpha}\sigma^{\alpha}}$. Hence, 4.25 becomes:

$$\begin{aligned} H_{MT^{\mu}}^{\mathbf{G}'\sigma'\mathbf{G}\sigma}(\mathbf{k}) &= \\ \sum_{\sigma^{\alpha}} \int_{MT^{\mu}} \left(\sum_{L'} \left(A_{L'\sigma'\sigma^{\alpha}}^{\mu\mathbf{G}'}(\mathbf{k}) u_{l'\sigma^{\alpha}}^{\alpha}(r) + B_{L'\sigma'\sigma^{\alpha}}^{\mu\mathbf{G}'}(\mathbf{k}) \dot{u}_{l'\sigma^{\alpha}}^{\alpha}(r) \right) Y_L'(\hat{\mathbf{r}}) \chi_{\sigma^{\alpha}}^{\alpha g} \right)^* &\mathcal{H}_{MT^{\mu}} \\ \left(\sum_L \left(A_{L\sigma\sigma^{\alpha}}^{\mu\mathbf{G}}(\mathbf{k}) u_{l\sigma^{\alpha}}^{\alpha}(r) + B_{L\sigma\sigma^{\alpha}}^{\mu\mathbf{G}}(\mathbf{k}) \dot{u}_{l\sigma^{\alpha}}^{\alpha}(r) \right) Y_L(\hat{\mathbf{r}}) \chi_{\sigma^{\alpha}}^{\alpha g} \right) &d^3r \end{aligned} \quad (4.26)$$

Using 4.23 and the fact that $(\chi_{\sigma^{\alpha}}^{\alpha g})^* \mathcal{H}_{MT^{\mu}} \chi_{\sigma^{\alpha}}^{\alpha g} = H_{MT^{\mu}\sigma^{\alpha}}^{\mathbf{G}'\mathbf{G}}(\mathbf{k})$ 4.26 simplifies to:

$$H_{MT^{\mu}}^{\mathbf{G}'\sigma'\mathbf{G}\sigma}(\mathbf{k}) = \sum_{\sigma^{\alpha}} ((\chi_{\sigma^{\alpha}}^{\alpha g})^* \chi_{\sigma'})^* (\chi_{\sigma^{\alpha}}^{\alpha g})^* \chi_{\sigma} H_{MT^{\mu}\sigma^{\alpha}}^{\mathbf{G}'\mathbf{G}}(\mathbf{k}) \quad (4.27)$$

In complete analogy the muffin-tin contribution to the non-collinear overlap-matrix is given by:

$$S_{MT^{\mu}}^{\mathbf{G}'\sigma'\mathbf{G}\sigma}(\mathbf{k}) = \sum_{\sigma^{\alpha}} ((\chi_{\sigma^{\alpha}}^{\alpha g})^* \chi_{\sigma'})^* (\chi_{\sigma^{\alpha}}^{\alpha g})^* \chi_{\sigma} S_{MT^{\mu}\sigma^{\alpha}}^{\mathbf{G}'\mathbf{G}}(\mathbf{k}) \quad (4.28)$$

4.3 Possible Extensions of the Method

The results that have been obtained for the unsupported monolayers of Cr (Ag(111) geometry) and Mn (Cu(111) geometry) show (cf. Chapter 6), that the accuracy of the frozen potential approximation is limited. The main reason that causes the inaccuracy are the approximations that have to be made in the interstitial and vacuum region. With these approximations made, the method can only be applied to systems with large local magnetic moments, well confined inside of the muffin-tin spheres, and small interstitial and vacuum magnetizations. The requirements are satisfied reasonably by the unsupported Cr monolayer in the Ag(111) geometry (Cr UML-Ag(111)), that we have investigated, but for the Mn UML-Cu(111), with its smaller lattice constant and local magnetic moments, the limits of this approximation is reached (cf. Chapter 6). However, the unsupported monolayers are already close to the limit of free atoms, with their large magnetic moments. Thus, in order to allow the application of the method to a larger class of systems it is necessary to extend the method to selfconsistent non-collinear calculations. Different ways of performing such selfconsistent calculations are thinkable.

One option is to allow a general magnetization density in the interstitial region, with both, magnitude and direction, depending on the position vector \mathbf{r} , while having the magnetization inside each muffin-tin point along a single direction. This means, that, after each iteration of a selfconsistent calculation, the magnetization density in the interstitial and vacuum region is calculated according to (2.17). Inside the muffin-tin sphere the expectation value of the magnetization is computed along one local quantization axis only. Thus, the magnetization density inside the spheres is a scalar rather than a vector field.

$$m^\alpha(\mathbf{r}) = \sum_{i=1}^N \psi_i^*(\mathbf{r}) \sigma^l \psi_i(\mathbf{r}) \quad (4.29)$$

σ^l is the spin operator corresponding to the local quantization axis. The direction of the local quantization axis can either be kept fixed, so that the magnetization is forced to be directed along a chosen direction, or it can be determined selfconsistently after each iteration. Within this approximation the rotation of the atomic magnetic moments with respect to each other, the inter-atomic non-collinear magnetism, can be described [SHK89, Küb95, SK96], while changes of the direction of the magnetization inside single atoms, the intra-atomic non-collinear magnetism [NS96], is neglected. The most general scheme is to allow the magnetization to have a different direction everywhere in space and, thus to include also the intra-atomic non-collinear magnetism. Thus, the magnetization density has to be calculated selfconsistently according to (2.17) everywhere in space. Such calculations are most accurate, because no approximations to the direction of the magnetization are made. However, due to larger number of degrees of freedom and the small energy differences that are associated with changes of the direction of the magnetization, many iterations are needed on the way to selfconsistency. Therefore, such calculations may turn out to be laborious.

Chapter 5

The Local Orbital Extension

For certain applications it is desirable to improve the variational freedom of the FLAPW basis set. As a result of the linearization around the energy parameter E_l the FLAPW method may only yield accurate results, if the calculated eigenvalues ϵ are reasonably close to the energy parameters. In some cases however, it is necessary to deal with eigenvalues in a broader energy region. Our main motivation to implement the local orbitals was to obtain a spin-independent basis set. In the current implementation of the FLAPW method the radial functions u_l and \dot{u}_l are calculated separately for both spin directions, with different energy parameters. The energy difference between the spin-up and -down bands is of the order of 2eV at surfaces, therefore these states cannot be treated accurately with a single set of radial functions. A second example where a greater variational freedom is needed are semicore states. Semicore states are high lying core states, typically 1 to 3 Ry (15 – 40 eV) below the Fermi energy. They show a small dispersion of the energy bands due to a weak overlap of their wavefunctions. So far, these states have either been added to the core, or treated with a second set of energy parameters in a separate energy window (semicore window), the latter method is usually referred to as multiple window FLAPW method. Both methods have serious disadvantages. If the semicore states are added to the core their dispersion is neglected. The core states are treated like an atomic problem, i.e. the overlap with other atoms is neglected. This approximation leads to wrong results in applications where the dispersion of these states plays an important role, e.g. during the calculation of lattice constants [Sin91a], phonon frequencies [SK91], forces or electric field gradients [BSSS92]. Another difficulty arises, because the FLAPW basis functions are not orthogonal to the semicore states. It can be shown, that the radial basis functions are orthogonal to any core state that is zero outside the muffin-tin sphere. However, this condition is satisfied poorly by the semicore states. Therefore, these states can appear in the valence eigenvalue spectrum as the so called “ghost-bands”. The eigenvalues of these states are usually far off the correct energy of the semicore state, due to the poor representation of these states within the valence FLAPW basis. A very good discussion of this problem can be found in [Sin94]. In multiple window calculations the dispersion of the semicore states is treated correctly, but the ghost-band problem may still be present. The

implementation of multiple windows in the current version of our FLAPW code will be discussed in the next section.

The local orbitals are an extension to the FLAPW basis set, that has been introduced by Singh [Sin91b]. The original motivation was the treatment of semicore states, though the local orbitals can be applied in any situation that demands for a greater variational freedom of the basis set. With this extension semicore and valence states can be treated in a single window, and the difficulties described above are removed. During the implementation of the local orbitals, their application to the semicore states of titanium and tungsten served as a test.

5.1 Multiple Window FLAPW

In a multiple window FLAPW calculation a second set of basis functions, that have exactly the same form as in (3.4), but with different energy parameters, is used. In order to distinguish these basis functions an additional index “ w ”, counting the windows, is introduced.

$$\varphi_{w,\mathbf{G}}(\mathbf{k}, \mathbf{r}) = \begin{cases} e^{i(\mathbf{G}+\mathbf{k})\mathbf{r}} & \text{interstitial region} \\ \sum_L A_{L,w}^{\mu\mathbf{G}}(\mathbf{k}) u_{l,w}(r) Y_L(\hat{\mathbf{r}}) + B_{L,w}^{\mu\mathbf{G}}(\mathbf{k}) \dot{u}_{l,w}(r) Y_L(\hat{\mathbf{r}}) & \text{muffin-tin } \mu \end{cases} \quad (5.1)$$

If the planewave cut-off in the semicore window was chosen to equal the cut-off in the valence window, G_{max} , this would result in a twice bigger basis set as compared to the single window calculation. That means, however, that the solution of the secular problem would take about eight times as long. Therefore, the overlap between the two windows is usually neglected. This leads to the solution of two independent eigenvalue problems per selfconsistent iteration, within which the size of the eigenvalue problem is the same as it is in the case of a single window calculation. Since, the semicore states have little dispersion, less k-points are needed in the semicore window, which makes this a rather efficient scheme. However, neglecting the overlap can lead to ghost-bands in the valence window. And, in some applications, the overlap has to be included to obtain accurate results [YFP⁺91].

An improvement to this scheme can be achieved, if the overlap between the windows is included in a second-variation step. The Hamiltonian and overlap matrix can be split into two parts:

$$\mathbf{H} = \mathbf{H}^0 + \mathbf{H}', \quad \mathbf{S} = \mathbf{S}^0 + \mathbf{S}' \quad (5.2)$$

Where \mathbf{H}^0 and \mathbf{S}^0 contain all matrix elements except those, that couple the two windows, i.e. \mathbf{H}^0 and \mathbf{S}^0 consist of two completely independent matrices, one for each window. \mathbf{H}' and \mathbf{S}' contain the overlap of the two windows. In the first variation step the two windows are treated separately, as described above, i.e. the two independent secular equations

$$\left\{ \mathbf{H}_w^0 - \epsilon_{1,w}^0 \mathbf{S}_w^0 \right\} \mathbf{c}_{1,w}^0 = 0 \quad (5.3)$$

are solved, yielding the eigenfunctions

$$\psi_{i,w}^0 = \sum_{\mathbf{G}} c_{i,w,\mathbf{G}} \varphi_{w,\mathbf{G}} \quad (5.4)$$

in each window. These eigenfunctions serve as a basis in the second-variation step. The secular problem of the second-variation step is much smaller, using twice the number of occupied states in each window usually gives a sufficient basis set. In the second variation step the overlap between the windows is taken into account. Thus, the semicore states can be treated very accurately within this scheme. However, the same k-point set has to be used in both windows. Therefore, this scheme is less efficient, than calculations neglecting the overlap. In the current version of our FLAPW code the latter scheme is implemented, i.e. multiple window calculation are performed neglecting the overlap between the windows.

5.2 Implementation of the Local Orbital Extension

The local orbitals are an extension to the FLAPW basis, that can be used to improve the variational freedom for a specific purpose, e.g. to improve the representation of the semicore states. The extra basis functions are completely localized inside the muffin-tin spheres, i.e. their value and derivative falls to zero at the muffin-tin radius. Thus, no additional boundary conditions have to be satisfied. This can be achieved via a linear combination including three radial function¹, the standard FLAPW functions u_l^α and \dot{u}_l^α plus a further radial function $u_{l_o}^\alpha$. This new radial function is constructed in the same way as u_l^α , but with a different energy parameter $E_{l_o}^\alpha$. If the local orbitals are used to treat semicore states, this energy parameter is set to the energy of these states. The local orbitals can be used very specifically, e.g. if they are applied to the 5*p* semicore states of tungsten only local orbitals with *p*-character are added to the basis. Hence, very few extra functions are needed, which makes local local calculations very efficient. In the case of the tungsten 5*p* states only three local orbitals per atom ($l = 1, m = -1, 0, 1$) are needed instead of to 60–100 augmented planewaves.

At this point a few remarks about the notation that will be used throughout this chapter should be made. The combination of the three radial function and a spherical harmonic, $(a_{l_o}^\alpha u_l^\alpha(r) + b_{l_o}^\alpha \dot{u}_l^\alpha(r) + c_{l_o}^\alpha u_{l_o}^\alpha(r))Y_L$, will be called local orbital. l is the angular momentum quantum number of the local orbital, $l = l_{l_o}$. The index l_o counts the different local orbital radial functions. Let's consider an example, the treatment of the 2*p*, 3*s* and 3*p* semicore states of Ti. Three additional radial functions are needed, e.g. 2*p*: $l_o = 1$, 3*s*: $l_o = 2$ and 3*p*: $l_o = 3$, thus $l_{l_o=1} = 1$, $l_{l_o=2} = 0$ and $l_{l_o=3} = 1$. The local orbitals with $l_o = 1$ and $l_o = 3$ have the same angular momentum quantum number, they differ only by their energy parameters, $E_{l_o=1} \neq E_{l_o=3}$ and, as

¹Within this section the radial functions are denoted $u_l(r)$ for simplicity, though in scalar-relativistic calculating the functions $g_l(r)$ and $\phi_l(r)$ are used instead of $u_l(r)$.

a consequence, by their radial functions, $u_{l_0=1}(r) \neq u_{l_0=3}(r)$. Latter in this chapter linear combinations of the local orbitals will be constructed, by formally coupling the local orbitals to planewaves, as if boundary conditions had to be satisfied. These linear combinations will also be called local orbitals.

5.3 Construction of the Local Orbitals

The three functions u_l^α , \dot{u}_l^α and $u_{l_0}^\alpha$ have to be combined, so that the value and the derivative of the local orbital fall to zero at the muffin-tin radius. Additionally, the resulting radial functions can be required to be normalized. Hence, to determine the coefficients of the radial functions $a_{l_0}^\alpha$, $b_{l_0}^\alpha$ and $c_{l_0}^\alpha$ we make use of the following three conditions:

$$a_{l_0}^\alpha u_l^\alpha(R_{MT^\alpha}) + b_{l_0}^\alpha \dot{u}_l^\alpha(R_{MT^\alpha}) + c_{l_0}^\alpha u_{l_0}^\alpha(R_{MT^\alpha}) = 0 \quad (5.5)$$

$$a_{l_0}^\alpha \frac{\partial u_l^\alpha}{\partial r}(R_{MT^\alpha}) + b_{l_0}^\alpha \frac{\partial \dot{u}_l^\alpha}{\partial r}(R_{MT^\alpha}) + c_{l_0}^\alpha \frac{\partial u_{l_0}^\alpha}{\partial r}(R_{MT^\alpha}) = 0 \quad (5.6)$$

$$\int_0^{R_{MT^\alpha}} (a_{l_0}^\alpha u_l^\alpha(R_{MT^\alpha}) + b_{l_0}^\alpha \dot{u}_l^\alpha(R_{MT^\alpha}) + c_{l_0}^\alpha u_{l_0}^\alpha(R_{MT^\alpha}))^2 r^2 dr = 1 \quad (5.7)$$

Where, l_0 is the index of the local orbital, which is necessary because more than one local orbital can be added for each atom. Solving these equations for the coefficients yields:

$$a_{l_0}^\alpha = K_{a,l_0}^\alpha c_{l_0}^\alpha \quad (5.8)$$

$$b_{l_0}^\alpha = K_{b,l_0}^\alpha c_{l_0}^\alpha \quad (5.9)$$

$$c_{l_0}^\alpha = \frac{1}{\sqrt{(K_{a,l_0}^\alpha)^2 + (K_{b,l_0}^\alpha)^2 \dot{N}_l^\alpha + 1 + 2K_{a,l_0}^\alpha N_{l_0}^\alpha + 2K_{b,l_0}^\alpha \dot{N}_{l_0}^\alpha}} \quad (5.10)$$

with

$$K_{a,l_0}^\alpha = \frac{1}{W} \left(u_{l_0}^\alpha(R_{MT^\alpha}) \frac{\partial \dot{u}_l^\alpha}{\partial r}(R_{MT^\alpha}) - \frac{\partial u_{l_0}^\alpha}{\partial r}(R_{MT^\alpha}) \dot{u}_l^\alpha(R_{MT^\alpha}) \right) \quad (5.11)$$

$$K_{b,l_0}^\alpha = -\frac{1}{W} \left(u_l^\alpha(R_{MT^\alpha}) \frac{\partial u_{l_0}^\alpha}{\partial r}(R_{MT^\alpha}) - \frac{\partial u_l^\alpha}{\partial r}(R_{MT^\alpha}) u_{l_0}^\alpha(R_{MT^\alpha}) \right) \quad (5.12)$$

with the Wronskian

$$W = \left(\frac{\partial u_l^\alpha}{\partial r}(R_{MT^\alpha}) \dot{u}_l^\alpha(R_{MT^\alpha}) - u_l^\alpha(R_{MT^\alpha}) \frac{\partial \dot{u}_l^\alpha}{\partial r}(R_{MT^\alpha}) \right), \quad (5.13)$$

where

$$\dot{N}_l^\alpha = \int_0^{R_{MT^\alpha}} (\dot{u}_l^\alpha)^2 r^2 dr \quad (5.14)$$

$$N_{l_0}^\alpha = \int_0^{R_{MT^\alpha}} u_l^\alpha u_{l_0}^\alpha r^2 dr \quad (5.15)$$

$$\dot{N}_{l_0}^\alpha = \int_0^{R_{MT^\alpha}} \dot{u}_l^\alpha u_{l_0}^\alpha r^2 dr, \quad (5.16)$$

and it has been used, that

$$\int_0^{R_{MT^\alpha}} (u_l^\alpha)^2 r^2 dr = 1 \quad (5.17)$$

$$\int_0^{R_{MT^\alpha}} (u_{l_0}^\alpha)^2 r^2 dr = 1. \quad (5.18)$$

The index l in $N_{l_0}^\alpha$ and $\dot{N}_{l_0}^\alpha$ has been omitted, $N_{l_0}^\alpha$ and $\dot{N}_{l_0}^\alpha$ always refer to the overlap integral of $u_{l_0}^\alpha$ and the radial functions that corresponding to the same angular momentum quantum number l . Clearly, if $E_{l_0}^\alpha$ is set equal to the energy parameter E_l^α with the same l , the overlap integrals (5.15) and (5.16) become $N_{l_0}^\alpha = 1$ and $\dot{N}_{l_0}^\alpha = 0$. This has been exploited to test the implementation of these integrals.

In actual calculations linear combinations of local orbitals that satisfy Bloch's theorem have to be constructed. Therefore A-, B- and C-coefficients are employed, which are constructed in the same way as the FLAPW A- and B-coefficients (3.115). Hence the additional basis functions are given by:

$$\varphi_{\mathbf{G}_{l_0}}^{\mu, l_0}(\mathbf{k}, \mathbf{r}) = \sum_m \left(A_{L_0}^{\mu \mathbf{G}_{l_0}}(\mathbf{k}) u_l^\alpha + B_{L_0}^{\mu \mathbf{G}_{l_0}}(\mathbf{k}) \dot{u}_l^\alpha + C_{L_0}^{\mu \mathbf{G}_{l_0}}(\mathbf{k}) u_{l_0}^\alpha \right) Y_L(\hat{\mathbf{r}}) \quad (5.19)$$

with

$$\begin{aligned} A_{L_0}^{\mu \mathbf{G}_{l_0}}(\mathbf{k}) &= e^{i\mathbf{K}_{l_0} \cdot \boldsymbol{\tau}^\mu} a_{l_0}^\alpha 4\pi \frac{1}{W} i^l Y_L^*(\mathbf{R}^\mu \hat{\mathbf{K}}_{l_0}) \\ B_{L_0}^{\mu \mathbf{G}_{l_0}}(\mathbf{k}) &= e^{i\mathbf{K}_{l_0} \cdot \boldsymbol{\tau}^\mu} b_{l_0}^\alpha 4\pi \frac{1}{W} i^l Y_L^*(\mathbf{R}^\mu \hat{\mathbf{K}}_{l_0}) \\ C_{L_0}^{\mu \mathbf{G}_{l_0}}(\mathbf{k}) &= e^{i\mathbf{K}_{l_0} \cdot \boldsymbol{\tau}^\mu} c_{l_0}^\alpha 4\pi \frac{1}{W} i^l Y_L^*(\mathbf{R}^\mu \hat{\mathbf{K}}_{l_0}) \end{aligned} \quad (5.20)$$

Where \mathbf{K}_{l_0} abbreviates $\mathbf{G}_{l_0} + \mathbf{k}$ and L_0 abbreviates (l_0, m) . The local orbitals are coupled to "fictitious" planewaves, even though no boundary conditions have to be satisfied. The vectors \mathbf{G}_{l_0} can be chosen arbitrarily, subject to the constrain that they yield linearly independent functions $\varphi_{\mathbf{G}_{l_0}}^{\mu, l_0}(\mathbf{k}, \mathbf{r})$. Finding such vectors is straightforward, e.g. by selecting planewaves one at a time and testing whether the corresponding $\varphi_{\mathbf{G}_{l_0}}^{\mu, l_0}(\mathbf{k}, \mathbf{r})$ is linearly independent of the previous local orbitals. If this is the case, the planewave is accepted, otherwise it is rejected. This procedure is carried out separately for each atom, i.e. the radial functions and spherical harmonics at a single atom form a local orbital, which is added to the FLAPW basis set. Apparently, this form of the coefficients is more complicated than necessary. The structure factor $e^{i\mathbf{K}_{l_0} \cdot \boldsymbol{\tau}^\mu}$ alone would be enough to satisfy Bloch's theorem. However, a further modification is needed when using the local orbitals in the presents of inversion symmetry. In this case the origin is usually chosen at an inversion center so that the secular equation becomes real (see section 3.3.4). In order to exploit this with local orbitals, linear combinations that transform like planewaves ($\varphi(-\mathbf{r}) = \varphi^*(\mathbf{r})$) must be used. In this case the local orbitals at atoms that can be mapped onto each other via inversion have to be coupled to a common set of planewaves. If there are for

example two tungsten atoms in the unit cell, that are related by inversion, and the local orbitals are used to treat the $5p$ states, a common set of six vectors \mathbf{G}_{l_0} must be found, that generates six linearly independent $\varphi_{\mathbf{G}_{l_0}}^{\mu, l_0}(\mathbf{k}, \mathbf{r})$. The resulting local orbitals have nonzero values inside the muffin-tin spheres of both atoms, and transform like planewaves (cf. section 3.3.4). Clearly, in a system that possesses inversion symmetry there has to have an “inversion partner” for every atom. However, this “partner” might lie in another unit cell. In this case the property $\varphi(-\mathbf{r}) = \varphi^*(\mathbf{r})$ is already guaranteed by the structure constant $e^{i\mathbf{K}_{l_0}\cdot\mathbf{r}}$ and the factor i^l . The factors 4π and $1/W$ do not have any effect on the properties of the local orbitals. They are merely scaling factors, and could as well be omitted.

5.4 Construction of the Additional Hamiltonian and Overlap Matrix Elements

Including the local orbitals to the FLAPW basis set leads to extra Hamiltonian and overlap matrix elements. When we write the new basis vector as a super vector containing the original FLAPW basis set $\varphi_{\mathbf{G}}$ and the local orbitals $\varphi_{\mathbf{G}_{l_0}}^{l_0}$ the Hamiltonian and overlap matrix can be written in the form:

$$\begin{pmatrix} H^{\mathbf{G}'\mathbf{G}} & H^{\mathbf{G}'\mathbf{G}_{l_0}} \\ H^{\mathbf{G}_{l_0}'\mathbf{G}} & H^{\mathbf{G}_{l_0}'\mathbf{G}_{l_0}} \end{pmatrix} \quad (5.21)$$

and equivalently for S . The matrix elements of the local orbitals with the augmented planewaves are given by:

$$H^{\mathbf{G}'\mathbf{G}_{l_0}}(\mathbf{k}) = \int (\varphi_{\mathbf{G}'}(\mathbf{k}, \mathbf{r}))^* \mathcal{H} \varphi_{\mathbf{G}_{l_0}}^{l_0}(\mathbf{k}, \mathbf{r}) d^3 r \quad (5.22)$$

$$S^{\mathbf{G}'\mathbf{G}_{l_0}}(\mathbf{k}) = \int (\varphi_{\mathbf{G}'}(\mathbf{k}, \mathbf{r}))^* \varphi_{\mathbf{G}_{l_0}}^{l_0}(\mathbf{k}, \mathbf{r}) d^3 r \quad (5.23)$$

The matrix elements of the local orbitals with other local orbitals (or with themselves) are given by:

$$H^{\mathbf{G}_{l_0}'\mathbf{G}_{l_0}}(\mathbf{k}) = \int (\varphi_{\mathbf{G}_{l_0}'}^{l_0'}(\mathbf{k}, \mathbf{r}))^* \mathcal{H} \varphi_{\mathbf{G}_{l_0}}^{l_0}(\mathbf{k}, \mathbf{r}) d^3 r \quad (5.24)$$

$$S^{\mathbf{G}_{l_0}'\mathbf{G}_{l_0}}(\mathbf{k}) = \int (\varphi_{\mathbf{G}_{l_0}'}^{l_0'}(\mathbf{k}, \mathbf{r}))^* \varphi_{\mathbf{G}_{l_0}}^{l_0}(\mathbf{k}, \mathbf{r}) d^3 r \quad (5.25)$$

In general each extra radial function corresponding to the index l_0 is assigned a different set of G -vectors $\{\mathbf{G}_{l_0}\}$. However, (5.24) and (5.25) also cover the case where $l_0' = l_0$. In this case \mathbf{G}_{l_0}' and \mathbf{G}_{l_0} are different G -vectors that correspond to the same radial function. Due to the confinement of the local orbitals to particular muffin-tin spheres, only on-site contributions² add to the Hamiltonian and overlap matrix.

²The contributions from different atoms, say α and α' , are zero

5.4.1 The Overlap Matrix Elements

The overlap matrix elements of the local orbitals situated at atom μ or a pair of atoms related by inversion $\mu, -\mu$ with the augmented planewaves is given by:

$$S^{\mathbf{G}\mathbf{G}_{l_0}}(\mathbf{k}) = \sum_{(\mu, -\mu)} \int_{MT^\mu} \left(\sum_{L'} \left(A_{L'}^{\mu\mathbf{G}}(\mathbf{k}) u_{l'}^\alpha(r) + B_{L'}^{\mu\mathbf{G}}(\mathbf{k}) \dot{u}_{l'}^\alpha(r) \right) Y_{L'}(\hat{\mathbf{r}}) \right)^* \left(\sum_m \left(A_{L_0}^{\mu\mathbf{G}_{l_0}}(\mathbf{k}) u_l^\alpha(r) + B_{L_0}^{\mu\mathbf{G}_{l_0}}(\mathbf{k}) \dot{u}_l^\alpha(r) + C_{L_0}^{\mu\mathbf{G}_{l_0}}(\mathbf{k}) u_{l_0}^\alpha(r) \right) Y_L(\hat{\mathbf{r}}) \right) d^3r \quad (5.26)$$

The sum over the atom pair $(\mu, -\mu)$ appears only in the case of atoms that are related by inversion, otherwise the whole contribution comes from a single muffin-tin μ . Using the orthogonality of the spherical harmonics, the orthogonality of u_l^α and \dot{u}_l^α and the normalization of u_l^α , (5.26) becomes:

$$S^{\mathbf{G}\mathbf{G}_{l_0}}(\mathbf{k}) = \sum_{(\mu, -\mu)} \sum_m \left(A_L^{\mu\mathbf{G}}(\mathbf{k}) \right)^* \left(A_{L_0}^{\mu\mathbf{G}_{l_0}}(\mathbf{k}) + C_{L_0}^{\mu\mathbf{G}_{l_0}}(\mathbf{k}) N_{l_0}^\alpha \right) + \left(B_L^{\mu\mathbf{G}}(\mathbf{k}) \right)^* \left(B_{L_0}^{\mu\mathbf{G}_{l_0}}(\mathbf{k}) \dot{N}_l^\alpha + C_{L_0}^{\mu\mathbf{G}_{l_0}}(\mathbf{k}) \dot{N}_{l_0}^\alpha \right) \quad (5.27)$$

Where l is the angular momentum quantum number of the local orbital $l = l_{l_0}$. In the case of two atoms that can be mapped onto each other by inversion the $S^{\mathbf{G}\mathbf{G}_{l_0}}(\mathbf{k})$ is given by a sum of the contributions of the two atoms $S^{\mathbf{G}\mathbf{G}_{l_0}}(\mathbf{k}) = S_\mu^{\mathbf{G}\mathbf{G}_{l_0}}(\mathbf{k}) + S_{-\mu}^{\mathbf{G}\mathbf{G}_{l_0}}(\mathbf{k})$. However, it can be shown, that the two contributions are related by:

$$S^{\mu\mathbf{G}\mathbf{G}_{l_0}}(\mathbf{k}) = \left(S^{-\mu\mathbf{G}\mathbf{G}_{l_0}}(\mathbf{k}) \right)^* \quad (5.28)$$

Thus

$$S^{\mathbf{G}\mathbf{G}_{l_0}}(\mathbf{k}) = 2 \operatorname{Re} \left\{ S^{\mu\mathbf{G}\mathbf{G}_{l_0}}(\mathbf{k}) \right\} \quad (5.29)$$

This relation has been used for the implementation of the local orbitals. Substituting the A-, B- and C-coefficients the overlap can be written:

$$S^{\mu\mathbf{G}\mathbf{G}_{l_0}}(\mathbf{k}) = e^{i(\mathbf{G}_{l_0} - \mathbf{G})\boldsymbol{\tau}^\mu} \left(\frac{4\pi}{W} \right)^2 \sum_{m=-l}^l F_l^\alpha(K) Y_L(\mathbf{R}^\mu \hat{\mathbf{K}}) (a_{l_0}^\alpha + c_{l_0}^\alpha N_{l_0}^\alpha) Y_L^*(\mathbf{R}^\mu \hat{\mathbf{K}}_{l_0}) + G_l^\alpha(K) Y_L(\mathbf{R}^\mu \hat{\mathbf{K}}) (b_{l_0}^\alpha \dot{N}_{l_0}^\alpha + c_{l_0}^\alpha \dot{N}_{l_0}^\alpha) Y_L^*(\mathbf{R}^\mu \hat{\mathbf{K}}_{l_0}) \quad (5.30)$$

Where

$$F_l^\alpha(K) = \left[\dot{u}_l^\alpha(R_{MT^\alpha} K) \frac{\partial j_l}{\partial r}(R_{MT^\alpha} K) - \frac{\partial \dot{u}_l^\alpha}{\partial r}(R_{MT^\alpha}) j_l(R_{MT^\alpha} K) \right] \\ G_l^\alpha(K) = \left[u_l^\alpha(R_{MT^\alpha} K) \frac{\partial j_l}{\partial r}(R_{MT^\alpha} K) - \frac{\partial u_l^\alpha}{\partial r}(R_{MT^\alpha}) j_l(R_{MT^\alpha} K) \right] \quad (5.31)$$

\mathbf{K} abbreviates $\mathbf{G} + \mathbf{k}$ and $K = |\mathbf{K}|$. This can be simplified further using the addition theorem for the spherical harmonics:

$$P_l(\cos \omega) = \frac{4\pi}{2l+1} \sum_{m=-l}^l Y_L(\hat{\mathbf{k}}_1) Y_L^*(\hat{\mathbf{k}}_2) \quad (5.32)$$

Where ω is the angle between the two vectors. Applying this theorem (5.30) becomes:

$$\begin{aligned} S_\mu^{\mathbf{G}\mathbf{G}_{l_o}}(\mathbf{k}) &= e^{i(\mathbf{G}_{l_o}-\mathbf{G})\boldsymbol{\tau}^\mu} \left(\frac{4\pi}{W}\right)^2 \frac{2l+1}{4\pi} P_l(\cos \omega) \\ &\quad \left(F_l^\alpha(K) (a_{l_o}^\alpha + c_{l_o}^\alpha N_{l_o}^\alpha) + G_l^\alpha(K) (b_{l_o}^\alpha \dot{N}_{l_o}^\alpha + c_{l_o}^\alpha \dot{N}_{l_o}^\alpha) \right) \end{aligned} \quad (5.33)$$

with

$$\cos \omega = \hat{\mathbf{K}} \cdot \hat{\mathbf{K}}_{l_o} \quad (5.34)$$

The overlap between different local orbitals can be derived in exactly the same way. Clearly, it can only be non-zero, if the angular momentum quantum number l of the local orbitals are equal $l_{l_o} = l_{l_o'}$.

$$\begin{aligned} S_\mu^{\mathbf{G}_{l_o'}\mathbf{G}_{l_o}}(\mathbf{k}) &= e^{i(\mathbf{G}_{l_o}-\mathbf{G}_{l_o'})\boldsymbol{\tau}^\mu} \left(\frac{4\pi}{W}\right)^2 \frac{2l+1}{4\pi} P_l(\cos \omega) \left(a_{l_o'}^\alpha (a_{l_o}^\alpha + c_{l_o}^\alpha N_{l_o}^\alpha) \right. \\ &\quad \left. + b_{l_o'}^\alpha (b_{l_o}^\alpha \dot{N}_{l_o}^\alpha + c_{l_o}^\alpha \dot{N}_{l_o}^\alpha) + c_{l_o'}^\alpha (a_{l_o}^\alpha N_{l_o}^\alpha + b_{l_o}^\alpha \dot{N}_{l_o}^\alpha + c_{l_o}^\alpha N_{l_o',l_o}^\alpha) \right) \end{aligned} \quad (5.35)$$

Where the normalization of $u_{l_o}^\alpha$ and

$$N_{l_o',l_o}^\alpha = \int_0^{R_{MT}^\alpha} u_{l_o'}^\alpha u_{l_o}^\alpha r^2 dr \quad (5.36)$$

has been used. A relation which is equivalent to (5.28) holds for the overlap between different local orbitals. Hence, the elements of the overlap matrix between local orbitals situated at two atoms, that are related by inversion, can be written:

$$S^{\mathbf{G}_{l_o'}\mathbf{G}_{l_o}}(\mathbf{k}) = 2 \operatorname{Re} \left\{ S_\mu^{\mathbf{G}_{l_o'}\mathbf{G}_{l_o}}(\mathbf{k}) \right\} \quad (5.37)$$

5.4.2 The Hamiltonian Matrix Elements

The Hamiltonian matrix elements of the local orbitals situated at atom μ or a pair of atoms related by inversion $(\mu, -\mu)$ with the augmented planewaves is given by:

$$\begin{aligned} H^{\mathbf{G}\mathbf{G}_{l_o}}(\mathbf{k}) &= \left(\sum_{\mu, -\mu} \right) \int_{MT^\mu} \left(\sum_{L'} \left(A_{L'}^{\mu\mathbf{G}}(\mathbf{k}) u_{l'}^\alpha(r) + B_{L'}^{\mu\mathbf{G}}(\mathbf{k}) \dot{u}_{l'}^\alpha(r) \right) Y_{L'}(\hat{\mathbf{r}}) \right)^* \mathcal{H}_{MT^\alpha} \\ &\quad \left(\sum_m \left(A_{L_o}^{\mu\mathbf{G}_{l_o}}(\mathbf{k}) u_l^\alpha(r) + B_{L_o}^{\mu\mathbf{G}_{l_o}}(\mathbf{k}) \dot{u}_l^\alpha(r) + C_{L_o}^{\mu\mathbf{G}_{l_o}}(\mathbf{k}) u_{l_o}^\alpha(r) \right) Y_L(\hat{\mathbf{r}}) \right) d^3 r \end{aligned} \quad (5.38)$$

As in the case of the overlap matrix it can be shown, that the contribution of an atom (μ) and the inverse atom ($-\mu$) are related by:

$$H^{\mu\mathbf{G}\mathbf{G}_{l_0}}(\mathbf{k}) = \left(H^{-\mu\mathbf{G}\mathbf{G}_{l_0}}(\mathbf{k}) \right)^* \quad (5.39)$$

Thus

$$H^{\mathbf{G}\mathbf{G}_{l_0}}(\mathbf{k}) = 2 \operatorname{Re} \left\{ H^{\mu\mathbf{G}\mathbf{G}_{l_0}}(\mathbf{k}) \right\} \quad (5.40)$$

(5.38) involves integrations of the form

$$t_{L'L_0}^{\alpha\varphi\varphi} = \int_{MT^\alpha} (u_{l'}^\alpha Y_{L'}(\hat{\mathbf{r}}))^* \mathcal{H}_{MT^\alpha} u_{l_0}^\alpha Y_L(\hat{\mathbf{r}}) d^3 r \quad (5.41)$$

$$t_{L'L_0}^{\alpha\dot{\varphi}\varphi} = \int_{MT^\alpha} (\dot{u}_{l'}^\alpha Y_{L'}(\hat{\mathbf{r}}))^* \mathcal{H}_{MT^\alpha} u_{l_0}^\alpha Y_L(\hat{\mathbf{r}}) d^3 r \quad (5.42)$$

in addition to ((3.61)–(3.64)). For Hamiltonian matrix elements including two different local orbitals an additional integration is required.

$$t_{L_0'L_0}^{\alpha\varphi\varphi} = \int_{MT^\alpha} (u_{l_0'}^\alpha(r) Y_{L'}(\hat{\mathbf{r}}))^* \mathcal{H}_{MT^\alpha} u_{l_0}^\alpha(r) Y_L(\hat{\mathbf{r}}) d^3 r \quad (5.43)$$

These t -matrices do not depend on \mathbf{G} , \mathbf{G}_{l_0} or \mathbf{k} . Therefore, they need to be calculated only once per iteration. The calculation of these matrix elements is performed in the same way as the calculation of the analogous t -matrices for the FLAPW basis ((3.73)–(3.76)). If the energy parameters of the local orbitals are set equal to the values of the energy parameters of the FLAPW radial functions, the corresponding matrix elements become equal. This relation has been used to test the implementation of the t -matrices.

The Hamiltonian matrix elements (5.38) can now be written in terms of the t -matrices.

$$\begin{aligned} H^{\mu\mathbf{G}\mathbf{G}_{l_0}}(\mathbf{k}) = & \\ & \sum_{\substack{m \\ L'}} \left(A_{L'}^{\mu\mathbf{G}}(\mathbf{k}) \right)^* \left[t_{L'L}^{\alpha\varphi\varphi} A_{L_0}^{\mu\mathbf{G}_{l_0}}(\mathbf{k}) + t_{L'L}^{\alpha\varphi\dot{\varphi}} B_{L_0}^{\mu\mathbf{G}_{l_0}}(\mathbf{k}) + t_{L'L_0}^{\alpha\varphi\varphi} C_{L_0}^{\mu\mathbf{G}_{l_0}}(\mathbf{k}) \right] \\ & + \left(B_{L'}^{\mu\mathbf{G}}(\mathbf{k}) \right)^* \left[t_{L'L}^{\alpha\dot{\varphi}\varphi} A_{L_0}^{\mu\mathbf{G}_{l_0}}(\mathbf{k}) + t_{L'L}^{\alpha\dot{\varphi}\dot{\varphi}} B_{L_0}^{\mu\mathbf{G}_{l_0}}(\mathbf{k}) + t_{L'L_0}^{\alpha\dot{\varphi}\varphi} C_{L_0}^{\mu\mathbf{G}_{l_0}}(\mathbf{k}) \right] \end{aligned} \quad (5.44)$$

In analogy the Hamiltonian matrix elements including two local orbitals are given by:

$$\begin{aligned} H^{\mu\mathbf{G}_{l_0'}\mathbf{G}_{l_0}}(\mathbf{k}) = & \\ & \sum_{mm'} \left(A_{L_0'}^{\mu\mathbf{G}}(\mathbf{k}) \right)^* \left[t_{L'L}^{\alpha\varphi\varphi} A_{L_0}^{\mu\mathbf{G}_{l_0}}(\mathbf{k}) + t_{L'L}^{\alpha\varphi\dot{\varphi}} B_{L_0}^{\mu\mathbf{G}_{l_0}}(\mathbf{k}) + t_{L'L_0}^{\alpha\varphi\varphi} C_{L_0}^{\mu\mathbf{G}_{l_0}}(\mathbf{k}) \right] \\ & + \left(B_{L_0'}^{\mu\mathbf{G}}(\mathbf{k}) \right)^* \left[t_{L'L}^{\alpha\dot{\varphi}\varphi} A_{L_0}^{\mu\mathbf{G}_{l_0}}(\mathbf{k}) + t_{L'L}^{\alpha\dot{\varphi}\dot{\varphi}} B_{L_0}^{\mu\mathbf{G}_{l_0}}(\mathbf{k}) + t_{L'L_0}^{\alpha\dot{\varphi}\varphi} C_{L_0}^{\mu\mathbf{G}_{l_0}}(\mathbf{k}) \right] \\ & + \left(C_{L_0'}^{\mu\mathbf{G}}(\mathbf{k}) \right)^* \left[t_{L_0'L}^{\alpha\varphi\varphi} A_{L_0}^{\mu\mathbf{G}_{l_0}}(\mathbf{k}) + t_{L_0'L}^{\alpha\varphi\dot{\varphi}} B_{L_0}^{\mu\mathbf{G}_{l_0}}(\mathbf{k}) + t_{L_0'L_0}^{\alpha\varphi\varphi} C_{L_0}^{\mu\mathbf{G}_{l_0}}(\mathbf{k}) \right] \end{aligned} \quad (5.45)$$

Where the contribution of atom pair μ , $-\mu$ can be obtained from:

$$H^{\mathbf{G}_{l_0'}\mathbf{G}_{l_0}}(\mathbf{k}) = 2 \operatorname{Re} \left\{ H_{\mu}^{\mathbf{G}_{l_0'}\mathbf{G}_{l_0}}(\mathbf{k}) \right\} \quad (5.46)$$

Tests of the Hamiltonian and Overlap Matrix Elements

To test the set-up of the Hamiltonian and overlap matrix, we solved the secular equation and compared the semicore eigenvalues to those obtained from a two-window calculation. The $5s$ and $5p$ states of fcc La and the $5p$ states of bcc W served as test systems. In both cases we performed selfconsistent two-window calculations. Then we determined the eigenvalues with local orbitals at selected points in the Brillouin zone non-selfconsistently, using the charge density of the two window calculation. For La we used a lattice constant $a = 9.8 \text{ a.u.}$, a sphere radius $R_{MT} = 3.3 \text{ a.u.}$ and a planewave cut-off $R_{MT}G_{max} = 10.0$. The Brillouin zone integrations were performed using 60 special k-points in the irreducible part of the Brillouin zone. The W calculations were carried out at a lattice constant of $a = 5.91 \text{ a.u.}$ with a muffin-tin radius of $R_{MT} = 2.456 \text{ a.u.}$ and a planewave cut-off $R_{MT}G_{max} = 8.8$, using 126 k-points in the irreducible wedge of the Brillouin zone. For technical reasons we used a unit cell including two atoms in both cases. The results of these test are shown

Lanthanum	$5s$	$5p$	
2-window	-1.816558	-0.659386	-0.548262
local orbital	-1.816600	-0.664944	-0.549574

Table 5.1: Semicore eigenvalues of La at the Γ -point, calculated with 2-window FLAPW and local orbitals, using the same selfconsistent charge density (potential). The first value is the lower $5s$ eigenvalue, followed by the lowest and highest $5p$ eigenvalue. All eigenvalues are twofold spin-degenerate. The energies (given in Ry units) are with respect to the average interstitial potential, which is $0.5870 Ry$ below the Fermi energy.

Tungsten	$5p$	
2-window	-1.679244	-1.605268
local orbital	-1.608692	-1.605970

Table 5.2: Semicore eigenvalues of W at the Γ -point. The first value is the lowest $5p$ eigenvalue, followed by the highest $5p$ eigenvalue. Both eigenvalues are twofold spin-degenerate. The energies (given in Ry units) are with respect to the average interstitial potential, which is $1.1540 Ry$ below the Fermi energy.

for selected semicore eigenvalues in Fig. 5.1 and 5.2. The two methods are in good

agreement, the difference between the eigenvalues is of the order of 1 *mRy*. At other *k*-points with lower symmetry these differences are slightly larger. During the two window calculations the energy parameter in the semicore window for states with $l = 2$ and higher for La and states with $l = 0, l = 2$ and higher in the case of W were set far above the semicore band energies (4 *Ry*) to avoid ghost-bands. However, later test showed, that this is not necessary in the case of W, but that the artificial choice of energy parameters does affect the result of the calculations (e.g. the lattice constant). Therefore, we expect, that the agreement would be even better, if the energy parameters were set to the semicore band energy. We also carried out tests with W in four atom unit cell including an atom pair that can be mapped onto each other by inversion. This was necessary because such atom pairs are a special case in terms of the implementation of the local orbitals. These tests yielded an equally good agreement between the local orbital and the two-window calculation.

5.5 Construction of the Electron Density of Local Orbitals

The construction of the electron density in the FLAPW method has been discussed in section 3.6. Clearly, the local orbitals lead to extra contributions to the electron density inside the spheres. If local orbitals are used, the eigenfunctions of the Kohn-Sham equations are represented in the following form in the muffin-tins.

$$\begin{aligned} \psi_\nu^\mu(\mathbf{k}, \mathbf{r}) = & \sum_{\mathbf{G}} c_\nu^{\mathbf{G}}(\mathbf{k}) \sum_L \left(A_L^{\mu\mathbf{G}}(\mathbf{k}) u_l^\alpha(r) + B_L^{\mu\mathbf{G}}(\mathbf{k}) \dot{u}_l^\alpha(r) \right) Y_L(\hat{\mathbf{r}}) \\ & + \sum_{l_0} \sum_{\mathbf{G}_{l_0}} c_\nu^{\mathbf{G}_{l_0}}(\mathbf{k}) \sum_m \left(A_{L_0}^{\mu\mathbf{G}_{l_0}}(\mathbf{k}) u_l^\alpha(r) + B_{L_0}^{\mu\mathbf{G}_{l_0}}(\mathbf{k}) \dot{u}_l^\alpha(r) + C_{L_0}^{\mu\mathbf{G}_{l_0}}(\mathbf{k}) u_{l_0}^\alpha(r) \right) Y_L(\hat{\mathbf{r}}) \end{aligned} \quad (5.47)$$

The \mathbf{G} -dependent A-, B- and C-coefficients can be replaced by band-dependent coefficients, performing the summation over the planewaves (cf. (3.141)).

$$\begin{aligned} \psi_\nu^\mu(\mathbf{k}, \mathbf{r}) = & \sum_L \left(A_{L,\nu}^\mu(\mathbf{k}) u_l^\alpha(r) + B_{L,\nu}^\mu(\mathbf{k}) \dot{u}_l^\alpha(r) \right) Y_L(\hat{\mathbf{r}}) \\ & + \sum_{L_0} \left(A_{L_0,\nu}^\mu(\mathbf{k}) u_l^\alpha(r) + B_{L_0,\nu}^\mu(\mathbf{k}) \dot{u}_l^\alpha(r) + C_{L_0,\nu}^\mu(\mathbf{k}) u_{l_0}^\alpha(r) \right) Y_L(\hat{\mathbf{r}}) \end{aligned} \quad (5.48)$$

$$\begin{aligned} A_{L_0,\nu}^\mu(\mathbf{k}) = & \sum_{\mathbf{G}_{l_0}} c_\nu^{\mathbf{G}_{l_0}}(\mathbf{k}) A_{L_0}^{\mu\mathbf{G}_{l_0}}(\mathbf{k}), & B_{L_0,\nu}^\mu(\mathbf{k}) = & \sum_{\mathbf{G}_{l_0}} c_\nu^{\mathbf{G}_{l_0}}(\mathbf{k}) B_{L_0}^{\mu\mathbf{G}_{l_0}}(\mathbf{k}), \\ C_{L_0,\nu}^\mu(\mathbf{k}) = & \sum_{\mathbf{G}_{l_0}} c_\nu^{\mathbf{G}_{l_0}}(\mathbf{k}) C_{L_0}^{\mu\mathbf{G}_{l_0}}(\mathbf{k}) \end{aligned} \quad (5.49)$$

5.5.1 “l-like” Charge

The l-like charge can still be defined in the same way as in section 3.6.1 if local orbitals are used. However, the extra terms have to be taken into account. In section 3.6.1 we defined the k-dependent l-like charge by:

$$n_{\nu,l}^{\mu}(\mathbf{k}) = \int_{MT^{\mu}} |\psi_{\nu,l}^{\mu}(\mathbf{k}, \mathbf{r})|^2 d^3r \quad (5.50)$$

Substituting (5.48) yields:

$$\begin{aligned} n_{\nu,l}^{\mu}(\mathbf{k}) &= \sum_{m=-l}^l |A_L^{\mu\nu}(\mathbf{k})|^2 + |B_L^{\mu\nu}(\mathbf{k})|^2 \dot{N}_l^{\alpha} \\ &+ 2Re \left\{ \sum_{\substack{l_o \\ l_o=l}}^l \sum_{m=-l}^l \left(A_{L,\nu}^{\mu}(\mathbf{k}) \right)^* \left(A_{L_o,\nu}^{\mu}(\mathbf{k}) + C_{L_o,\nu}^{\mu}(\mathbf{k}) N_{l_o}^{\alpha} \right) \right. \\ &\quad \left. + \left(B_{L,\nu}^{\mu}(\mathbf{k}) \right)^* \left(B_{L_o,\nu}^{\mu}(\mathbf{k}) \dot{N}_l^{\alpha} + C_{L_o,\nu}^{\mu}(\mathbf{k}) \dot{N}_{l_o}^{\alpha} \right) \right\} \\ &+ \sum_{\substack{l_o, l_o' \\ l_o'=l_o=l}}^l \sum_{m=-l}^l \left(A_{l_o',m,\nu}^{\mu}(\mathbf{k}) \right)^* \left(A_{L_o,\nu}^{\mu}(\mathbf{k}) + C_{L_o,\nu}^{\mu}(\mathbf{k}) N_{l_o}^{\alpha} \right) \\ &\quad + \left(B_{l_o',m,\nu}^{\mu}(\mathbf{k}) \right)^* \left(B_{L_o,\nu}^{\mu}(\mathbf{k}) \dot{N}_l^{\alpha} + C_{L_o,\nu}^{\mu}(\mathbf{k}) \dot{N}_{l_o}^{\alpha} \right) \\ &\quad + \left(C_{l_o',m,\nu}^{\mu}(\mathbf{k}) \right)^* \left(A_{L_o,\nu}^{\mu}(\mathbf{k}) N_{l_o'}^{\alpha} + B_{L_o,\nu}^{\mu}(\mathbf{k}) \dot{N}_{l_o'}^{\alpha} + C_{L_o,\nu}^{\mu}(\mathbf{k}) N_{l_o',l_o}^{\alpha} \right) \end{aligned} \quad (5.51)$$

At this point, for the first time, a large number of cross-terms appear. This is a consequence of the fact, that the extra radial functions $u_{l_o}^{\alpha}$ are not orthogonal to the standard FLAPW radial functions.

5.5.2 The Optimal Local Orbital Energy Parameter

The optimal choice of the energy parameter for the local orbitals is defined by the requirement, that it minimizes the linearization error weighted with the l-like charge of the local orbitals, i.e. the charge that the local orbitals, which correspond to the energy parameter, contribute to the total charge (cf. section 3.6.2).

$$\int_{BZ} \sum_{\nu, \epsilon_{\nu}(\mathbf{k}) < E_F} (\epsilon_{\nu}(\mathbf{k}) - E_{l_o}^{\alpha})^2 n_{\nu,l_o}^{\mu}(\mathbf{k}) d^3k, \quad (5.52)$$

with

$$n_{\nu,l_o}^{\mu}(\mathbf{k}) = \sum_{m=-l_{l_o}}^{l_{l_o}} |C_{L_o,\nu}^{\mu}(\mathbf{k})|^2 \quad (5.53)$$

Setting the derivative ($\partial/\partial E_{lo}^\alpha$) equal to zero yields the optimal energy parameter:

$$E_{lo}^\alpha = \left(\int_{BZ} \sum_{\nu, \epsilon_\nu(\mathbf{k}) < E_F} \epsilon_\nu(\mathbf{k}) n_{\nu, lo}^\mu(\mathbf{k}) d^3 k \right) / \left(\int_{BZ} \sum_{\nu, \epsilon_\nu(\mathbf{k}) < E_F} n_{\nu, lo}^\mu(\mathbf{k}) d^3 k \right) \quad (5.54)$$

The Brillouin zone integration methods transform this into a sum over a discrete k-point set.

$$E_{lo}^\alpha = \left(\sum_{\mathbf{k}} \sum_{\nu} \epsilon_\nu(\mathbf{k}) n_{\nu, lo}^\mu(\mathbf{k}) w(\nu, \mathbf{k}) \right) / \left(\sum_{\mathbf{k}} \sum_{\nu} n_{\nu, lo}^\mu(\mathbf{k}) w(\nu, \mathbf{k}) \right) \quad (5.55)$$

There is one difficulty that arises within local orbital calculations. The FLAPW basis functions do contribute to the semicore eigenfunctions. Recall that the local orbitals are completely localized in the muffin-tin spheres. Therefore the components of the eigenfunctions that stretch beyond the spheres can only be described by the regular FLAPW functions. Hence, if the valence (FLAPW) energy parameters are determined by (3.151) with the l-like charge defined by (3.147), the contribution of the semicore states lowers the the energy parameters. This can lead to a ghost-band problem. It is therefore necessary to skip the semicore states in the sum over the band in (3.151). The local orbitals, however, contribute very little to the valence states. Thus, a similar distinction is not necessary during the determination of the local orbital energy parameters.

5.5.3 Construction of the Electron Density in the Muffin-Tins in the Presents of Local Orbitals

Substituting (5.48) into (3.137) yields the electron density in the muffin-tins.

$$\begin{aligned} n^\mu(\mathbf{r}) = & \frac{1}{V_{BZ}} \int_{BZ} \sum_{\nu, \epsilon_\nu(\mathbf{k}) < E_F} \left(\sum_{L'} A_{L', \nu}^\mu(\mathbf{k}) u_{l'}^\alpha(r) + B_{L', \nu}^\mu(\mathbf{k}) \dot{u}_{l'}^\alpha(r) \right. \\ & \left. + \sum_{Lo'} A_{Lo', \nu}^\mu(\mathbf{k}) u_{l'}^\alpha + B_{Lo', \nu}^\mu(\mathbf{k}) \dot{u}_{l'}^\alpha + C_{Lo', \nu}^\mu(\mathbf{k}) u_{lo'}^\alpha \right)^* Y_{L'}^*(\hat{\mathbf{r}}) \\ & \left(\sum_L A_L^{\mu\nu}(\mathbf{k}) u_l^\alpha(r) + B_{L, \nu}^\mu(\mathbf{k}) \dot{u}_l^\alpha(r) \right. \\ & \left. + \sum_{Lo} A_{Lo, \nu}^\mu(\mathbf{k}) u_l^\alpha + B_{Lo, \nu}^\mu(\mathbf{k}) \dot{u}_l^\alpha + C_{Lo, \nu}^\mu(\mathbf{k}) u_{lo}^\alpha \right) Y_L(\hat{\mathbf{r}}) d^3 k \end{aligned} \quad (5.56)$$

The coefficients $C_{L'}^\mu(r)$ (cf. 3.153) can be determined by multiplying (5.56) with $\int d\Omega Y_{L'}(\hat{\mathbf{r}})$. If the Brillouin zone integration is performed on a discrete k-point set the $C_{L'}^\mu(r)$ are given by:

$$C_{L'}^\mu(r) = \sum_{l'l} \left(\sum_{\mathbf{k}} \sum_{\nu} \sum_{m'm} \left(A_{L', \nu}^\mu(\mathbf{k}) \right)^* A_{L, \nu}^\mu(\mathbf{k}) G_{ll' m m'}^{m m'} w(\nu, \mathbf{k}) \right) u_{l'}^\alpha(r) u_l^\alpha(r)$$

$$\begin{aligned}
& + \sum_{l'o'l_0} \left(\sum_{\mathbf{k}} \sum_{\nu} \sum_{m'm} (B_{L'o',\nu}^{\mu}(\mathbf{k}))^* A_{L_o,\nu}^{\mu}(\mathbf{k}) G_{l'l''}^{mm'm''} w(\nu, \mathbf{k}) \right) \dot{u}_{l'}^{\alpha}(r) u_l^{\alpha}(r) \\
& + \sum_{l'o'l_0} \left(\sum_{\mathbf{k}} \sum_{\nu} \sum_{m'm} (B_{L'o',\nu}^{\mu}(\mathbf{k}))^* B_{L_o,\nu}^{\mu}(\mathbf{k}) G_{l'l''}^{mm'm''} w(\nu, \mathbf{k}) \right) \dot{u}_{l'}^{\alpha}(r) \dot{u}_l^{\alpha}(r) \\
& + \sum_{l'o'l_0} \left(\sum_{\mathbf{k}} \sum_{\nu} \sum_{m'm} (B_{L'o',\nu}^{\mu}(\mathbf{k}))^* C_{L_o,\nu}^{\mu}(\mathbf{k}) G_{l'l''}^{mm'm''} w(\nu, \mathbf{k}) \right) \dot{u}_{l'}^{\alpha}(r) u_{l_0}^{\alpha}(r) \\
& + \sum_{l'o'l_0} \left(\sum_{\mathbf{k}} \sum_{\nu} \sum_{m'm} (C_{L'o',\nu}^{\mu}(\mathbf{k}))^* A_{L_o,\nu}^{\mu}(\mathbf{k}) G_{l'l''}^{mm'm''} w(\nu, \mathbf{k}) \right) u_{l_0'}^{\alpha}(r) u_l^{\alpha}(r) \\
& + \sum_{l'o'l_0} \left(\sum_{\mathbf{k}} \sum_{\nu} \sum_{m'm} (C_{L'o',\nu}^{\mu}(\mathbf{k}))^* B_{L_o,\nu}^{\mu}(\mathbf{k}) G_{l'l''}^{mm'm''} w(\nu, \mathbf{k}) \right) u_{l_0'}^{\alpha}(r) \dot{u}_l^{\alpha}(r) \\
& + \sum_{l'o'l_0} \left(\sum_{\mathbf{k}} \sum_{\nu} \sum_{m'm} (C_{L'o',\nu}^{\mu}(\mathbf{k}))^* C_{L_o,\nu}^{\mu}(\mathbf{k}) G_{l'l''}^{mm'm''} w(\nu, \mathbf{k}) \right) u_{l_0'}^{\alpha}(r) u_{l_0}^{\alpha}(r)
\end{aligned} \tag{5.57}$$

Where the gaunt coefficients $G_{l'l''}^{mm'm''}$ are defined by (3.155), and (3.156) has been used. Apparently, there are only six combinations of radial functions ($u_{l'}^{\alpha}(r)u_l^{\alpha}(r), u_{l_0'}^{\alpha}(r)\dot{u}_l^{\alpha}(r), \dots, u_{l_0'}^{\alpha}(r)u_{l_0}^{\alpha}(r)$). Thus, the corresponding coefficients can be combined, but still all coefficients have to be calculated. (5.57) would simplify a lot, if the band-dependent coefficients of the local orbitals and the FLAPW basis functions, $A_{L_o,\nu}^{\mu}$ and $A_{L,\nu}^{\mu}$, $B_{L_o,\nu}^{\mu}$ and $B_{L,\nu}^{\mu}$, were combined. However, this has not been done in order to keep the old parts and the new parts of the program as separate as possible, to avoid errors and simplify the maintenance.

5.6 Test Calculation on Tungsten and Titanium

Titanium	a_0 -fcc	a_0 -hcp	$\Delta E_{fcc-hcp}$
1-window	5.363	5.371	7.32
2-window	5.359	5.367	7.27
local orbital	5.366	5.374	7.18
2-window*	5.462	—	—
2-window**	5.382	—	—

Table 5.3: Calculated lattice constants for fcc and hcp Ti in atomic units [a.u.]. In the last column the fcc-hcp energy ($E_{fcc} - E_{hcp}$) difference is given in Ry units. (* the semicore s, d and higher energy parameters have been set to 4.0 Ry, ** the semicore s, d and higher and the valence p energy parameters have been set to 4.0 Ry)

Tungsten	a_0 -bcc
1-window	5.945
2-window	5.943
local orbital	5.948
2-window*	6.050

Table 5.4: Calculated lattice constants for bcc W in atomic units [a.u.]. (* the semicore s, d and higher energy parameters have been set to 4.0 Ry and the valence p energy parameters have been set to 2.0 Ry)

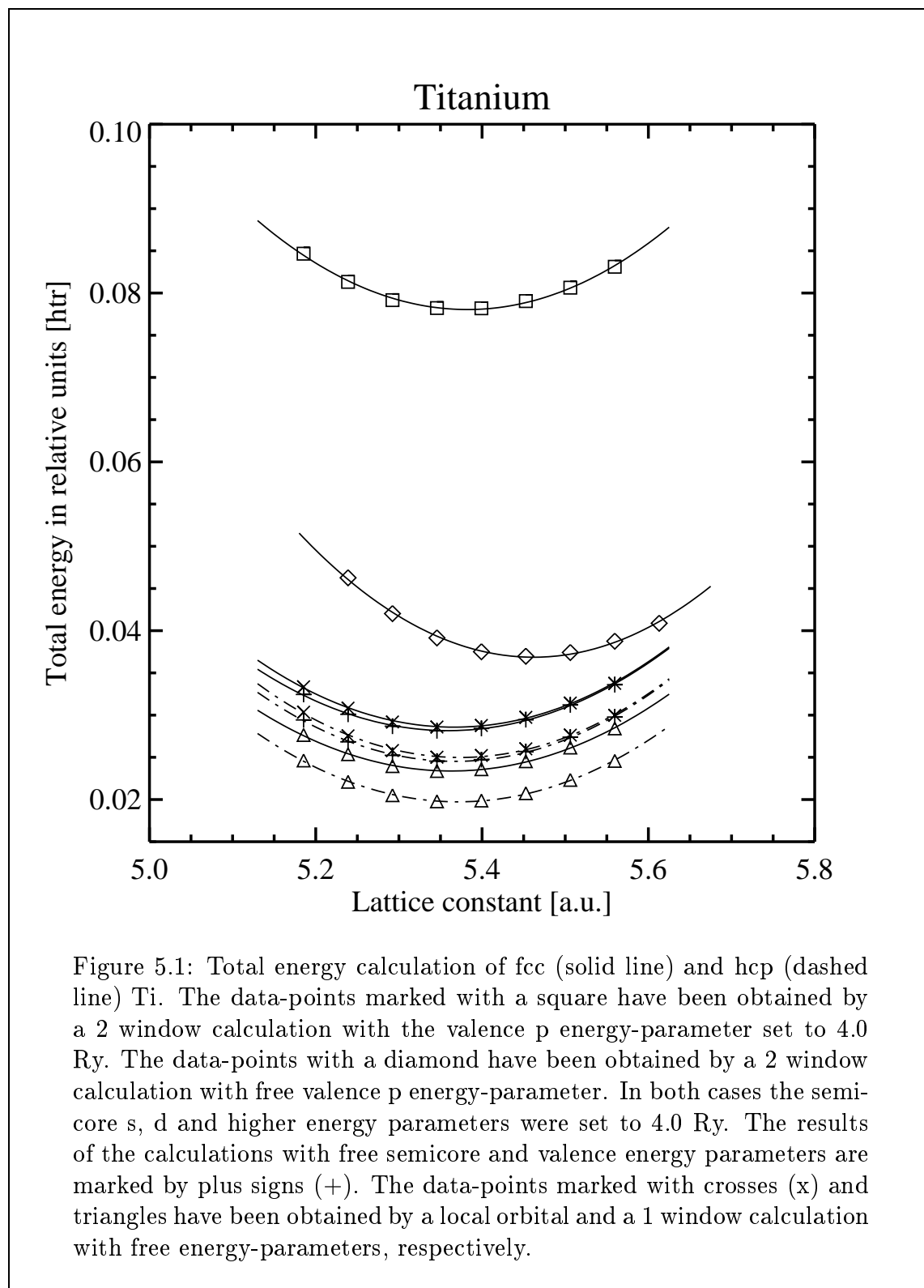
In order to test the implementation of the local orbitals, and in particular the construction of the charge density, we performed selfconsistent calculations of Ti and W. In both cases two-window and even one-window calculations lead to accurate results, which compare very well with the results obtained from a treatment with local orbitals. However, care must be taken choosing the energy parameters, only if all energy parameters are chosen reasonably close to the band energies accurate results are obtained. During the first two-window calculations we set the valence p-energy parameter and all semicore energy parameters except the p-parameter to values far above the band energies, to avoid ghost-bands (in both cases the highest lying semicore state is a p-state). Further calculations showed, that this is not necessary for Ti and W, and leads to wrong results. The Ti $3p$ -states are about 2.2 Ry lower in energy than the valence states, which make these states most likely to produce a ghost-band in the valence-window. The $3s$ -states are another 1.7 Ry lower than the $3p$ -states and could therefore cause a ghost-band in the semicore-window. To avoid the ghost-bands we first set the semicore s-, d- and higher energy parameters and the valence p-parameter to 4.0 Ry (these energies are given relative to the average interstitial potential, which is 0.62 Ry below the Fermi energy in the case of Ti, and 1.17 Ry for W. The values change slightly (≈ 0.1 Ry) with the lattice constant). The results of these total energy calculation are plotted in the uppermost curve in Fig. 5.1. The calculated lattice constant (cf. Table 5.3) is slightly larger than those obtained from latter, more accurate, calculations. If the valence p-parameter is relaxed, i.e. set to the computed optimal value (cf. Sec. 3.6.2) after each iteration, the results change substantially. The lattice constant became ever larger. Finally, we relaxed all semicore and valence energy parameters, which again lead to a considerable change. The results of the last calculation agree very well with the local orbital and even with a one-window calculations. The computed lattice constants differ by less than 0.15 %. The curves, which correspond to the two-window and the local orbital calculation are almost identical, whereas the one-window curve is shifted by about 10 mRy. We repeated the calculations with relaxed energy parameters for hcp Ti, in order to obtain the fcc-hcp energy difference. Again the results obtain with the

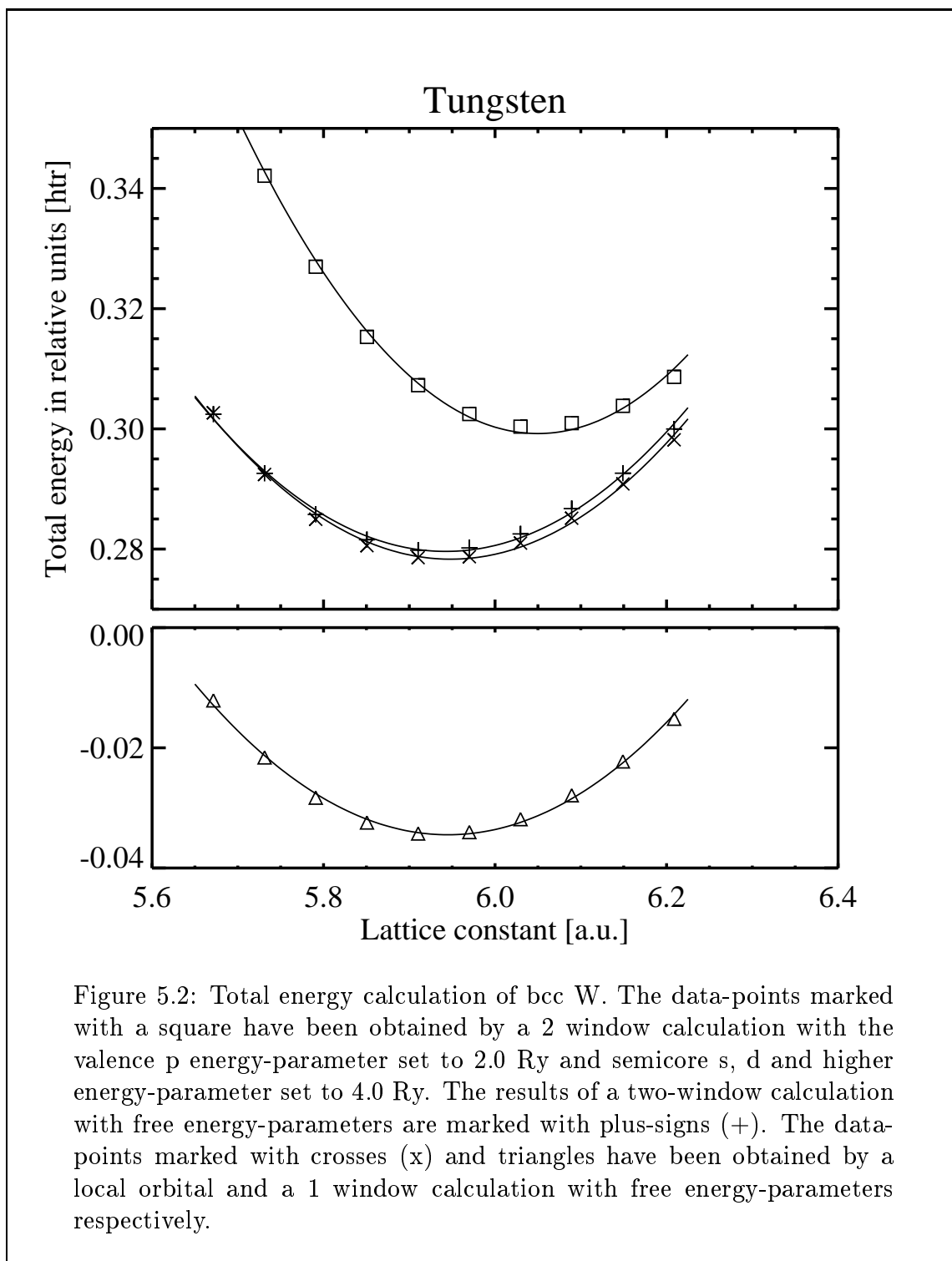
different schemes were very close to each other (cf. Table 5.3). The hcp structure is correctly predicted to be lower in energy than the fcc structure, and the energy difference agrees reasonably well with the results of other authors [AWJE93].

Clearly, setting the energy parameters to values far of the band energies has a strong effect on the calculations. This result is surprising in the case of the semicore states of Ti, since the s -, d - and f -like charge in the semicore window is extremely small (0.001 – 0.002 electrons). Thus, one should expect the results to depend very little on the corresponding parameters. However, if the energy parameters are raised above a certain value the number of nodes of the corresponding radial function increases. In the case of Ti this means, that, for example, the radial function u_0^α has $4s$ or $5s$ character rather than $3s$. This leads to a higher probability of finding the electron far from the nucleus, i.e. charge is pushed away from the nucleus. Apparently, this causes the increase of the lattice constant.

The results of the test calculations on W support this picture. If all energy parameters are relaxed, the results obtained from the three different schemes agree very well (cf. Fig. 5.2). The calculated lattice constants differ by less than 0.1 % (cf. Table 5.3) and lie within the range of the results of other authors [MH86, JF84, Koh95]. If, however, the semicore s -, d -, f -, ... and the valence p -energy parameters are raised above the band energies, the results change significantly, the lattice constant becomes more than 1.5 % larger.

Hence, we found, that in the case of Ti and W, where no ghost-band problem arises, local orbital, two-window and even one-window calculations agree very well. In systems that do show ghost-bands, these can, in general, not be removed by raising the corresponding energy parameter, because this can have a strong effect on the calculated properties.





Chapter 6

Non-Collinear Magnetism of Unsupported Monolayers with fcc(111) Geometry

$3d$ transition-metal monolayers on noble-metal substrates represent very interesting physical systems, both experimentally and theoretically [FPB⁺90, Sie92, LMF85, FFO85, Ter87, BDZD89, FW91, WB93, Blü95]. Due to filled d -bands of the noble-metals the $3d$ - $3d$ hybridization between the overlayer and the substrate is small, which leads to a narrowing of the d -bands in the monolayer compared to the bulk transition-metals. As a consequence, magnetism is enhanced and the magnetic moments become larger. Moreover, there is a possibility of new magnetic materials, which are non-magnetic as bulk metals. So far most of the work has been done on overlayers grown on the (100) orientated substrates, where the atoms of the monolayer are arranged on a square lattice. It turns out, that the early transition-metals, V, Cr and Mn, order $c(2 \times 2)$ antiferromagnetically on these surfaces, while Fe, Co and Ni prefer the $p(1 \times 1)$ ferromagnetic configuration. However, the $c(2 \times 8)$ reconstruction of Mn on Cu (100), which locally has a hexagonal structure, suggests that some of the transition-metal monolayers prefer a hexagonal geometry. This has been investigated by Pentcheva [Pen96] performing systematic calculations on unsupported $3d$ transition-metal monolayers with square and hexagonal geometry. The results prove, that in fact most $3d$ transition-metals except Cr prefer the hexagonal structure. However, this property is closely related to the magnetism of the monolayers, e.g. theoretical calculations suppressing the magnetism show that the non-magnetic quadratic UML of Mn is lower in energy than the hexagonal UML. In addition, Pentcheva compared two different magnetic configurations on the hexagonal lattice, the ferromagnetic structure and an antiferromagnetic configuration (Fig. 6.1 (a)), where four of the six nearest neighbor atoms have opposite magnetization, but the moments of the remaining two neighbors are parallel. Their calculations showed, that Cr and Mn prefer this antiferromagnetic structure. Assuming that this antiferromagnetism is predominantly driven by the nearest neighbor exchange coupling

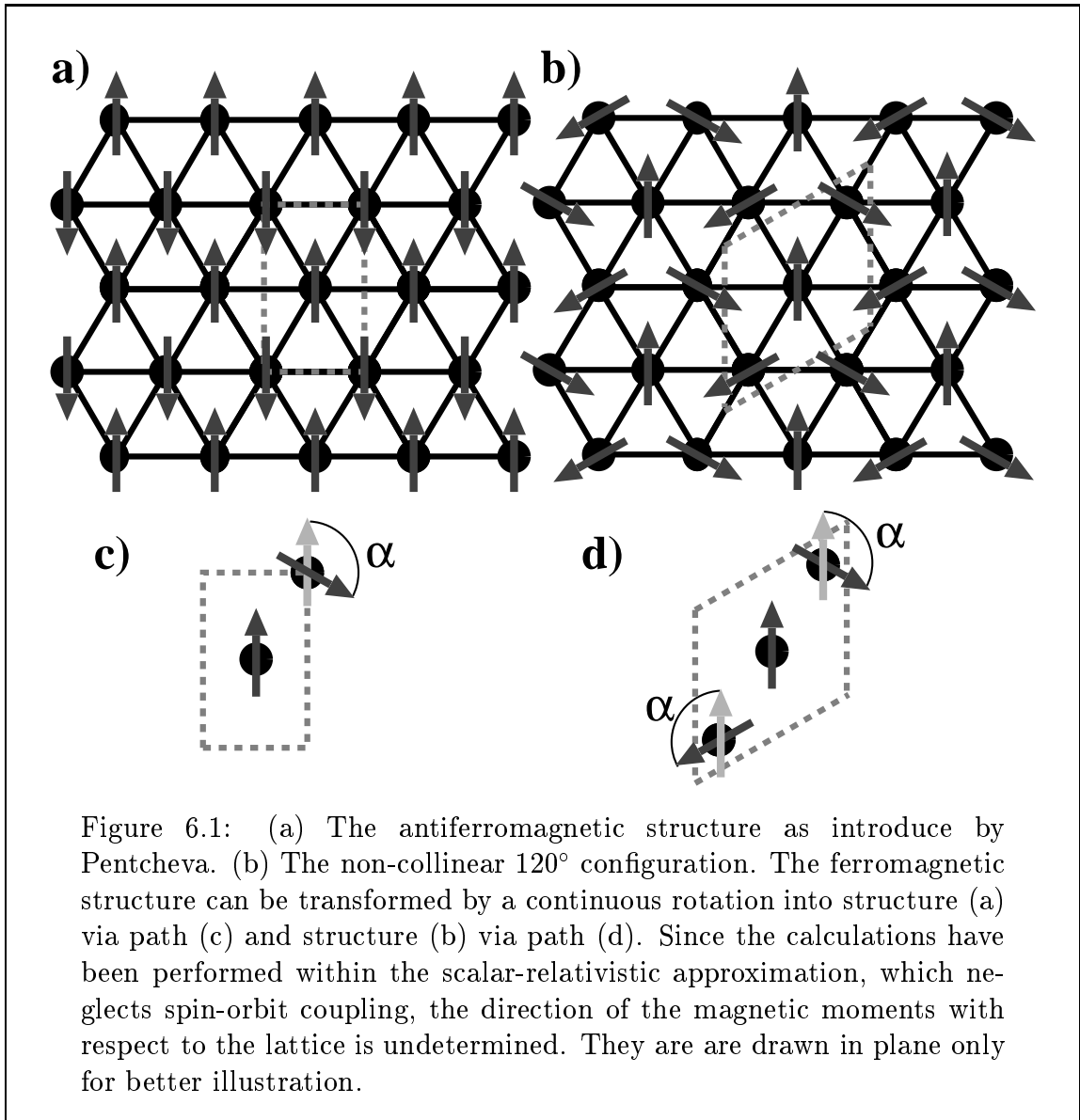
leads to the conclusion that the hexagonal monolayers of these metals constitute a frustrated spin-system.

In order to find a candidate for a possible non-collinear ground-state configuration we follow the idea of Wannier [Wan50]. We assume a two-dimensional planar Heisenberg model or x-y model and consider three atoms on a triangle. It can be shown, that if the coupling is antiferromagnetically, i.e. the Heisenberg parameter J is positive, the ground-state of this system is a configuration, where magnetic moments form 120° angles. At this point the idea of Wannier comes into play. Since this structure is compatible with the hexagonal lattice, this is also the ground-state of the hexagonal monolayer within the Heisenberg model. Therefore, we decided to compare this structure to the antiferromagnetic structure introduced by Pentcheva and a third collinear antiferromagnetic configuration.

The approximations we discussed in chapter 4 are only valid, if the magnetic moments inside the muffin-tin spheres are large and do not change much with the direction of the magnetization. Even more important for the accuracy of these approximations is a small interstitial magnetization. Therefore, we decided to apply our method to an unsupported Cr monolayer with Ag (111) geometry. Cr possesses a large magnetic moment, which is enhanced due to the big lattice constant of Ag. The lattice constant also allows for a large muffin-tin radius, which leads to a better confinement of the total magnetization inside the muffin-tin sphere. As a second system we investigated a Mn UML with the geometry of the Cu(111) surface. The Cu lattice constant is significantly smaller and the local magnetic moments of this system are not as big as is the case of the Cr UML-Ag(111). It turns out, that the Mn UML-(111) is less accurately described by the frozen potential approximation than the Cr UML-Ag(111).

6.1 Model Structures

We have investigated unsupported monolayers with hexagonal geometry with different collinear and non-collinear magnetic structures. The unit cell of the ferromagnetic structure is $p(1 \times 1)$ and contains one atom. The antiferromagnetic configurations as introduced by Pentcheva (a) and the non-collinear configuration with 120° angles (b) are shown in Fig. 6.1, which also contains the unit cells, marked by dotted lines. The antiferromagnetic unit cell contains two atoms, is rectangular and of twofold symmetry, while the unit cell of the 120° configuration contains three atoms and is of $(\sqrt{3} \times \sqrt{3})R30^\circ$ structure. It has the same shape as the $p(1 \times 1)$ unit cell, but it is rotated by 30° and $\sqrt{3}$ larger in linear dimension. We have also performed angle dependent calculations. The energy difference has been calculated along two different paths, which continuously transform the ferromagnetic structure into the antiferromagnetic configuration (Fig. 6.1 (c)) or the 120° configuration (Fig. 6.1 (d)). If the second path is extended up to $\alpha = 180^\circ$ we obtain an additional antiferromagnetic configuration with $2/3$ of the magnetic moments pointing along one direction and $1/3$ pointing along the opposite direction. This structure will be referred to as the



180° configuration.

6.2 Computational Details

The actual calculations have been performed using a unit cell containing six atoms. With this choice all configurations can be treated with the same unit cell, and thus inaccuracy in the energy difference due to different k-point sets for the Brillouin zone integration can be avoided. The Ag and the Cu lattice constants have been chosen according to Moruzzi, Janak and Williams [MJW78] $a_{Ag} = 7.79a.u.$, $a_{Cu} = 6.65a.u.$ We have used 15 k-points in the irreducible Brillouin zone (IBZ) for the k-integration.

As planewave cut-off for the wavefunctions we used $G_{max} = 3.2a.u.^{-1}$ in the case of the Cr UML-Ag(111) and $G_{max} = 3.6a.u.^{-1}$ in the case of the Mn UML-Cu(111), which amounts to about 110 basis functions per atom, while the potential and charge density are expanded up to $9.0a.u.^{-1}$. The non-spherical parts of the charge density, the potential and the wavefunctions have been expanded into spherical harmonics up to $l_{max} = 8$. We chose the muffin-tin radius as large as possible $R_{MT} = 2.75a.u.$. All parameters have been chosen correspondingly to the parameters of Pentcheva, except the wavefunction planewave cut-off. Convergence tests with respect to these parameters can be found in [Pen96].

6.3 Accuracy of the Frozen Potential Approximation

The energy differences between the different collinear and non-collinear magnetic configurations have been calculated via the frozen potential approximation (FPA) (cf. chap. 4). Within the frozen potential approximation the energy difference of two different magnetic configurations is estimated by the difference of the eigenvalue sums of non-selfconsistent calculations. First a selfconsistent collinear (e.g. ferromagnetic) calculation is performed yielding a potential $V(\mathbf{r})$ and a magnetic field $\mathbf{B}(\mathbf{r})$. A trial Hamiltonian, from which the eigenvalue sums are computed, is constructed by a rotation of the direction of the magnetic field, while the magnitude $B(\mathbf{r})$ is kept fixed (frozen). Within the local spin-density approximation (LSDA) $B(\mathbf{r})$ depends only locally on the magnitude of the magnetization $m(\mathbf{r})$. Therefore, this approximation is valid, if the magnitude of the magnetization does not change much with its direction. The hexagonal Cr UML-Ag(111) satisfies this condition very nicely. The selfconsistent magnetic moments per atom, i.e. $m(\mathbf{r})$ integrated over the muffin-tin sphere, show small differences. The antiferromagnetic moment is only about 1% smaller than the ferromagnetic moments, the 180° and the ferromagnetic configuration differ by about 3% (cf. Table 6.1). However, in FLAPW it is unclear

Atomic magnetic moments [in μ_B]	
FM	4.14
AFM	4.09
180° ($\uparrow\downarrow\uparrow$)	$m_\uparrow = 4.02, m_\downarrow = 3.99$

Table 6.1: Selfconsistent total magnetic moment per atom of the Cr UML-Ag(111) for different collinear magnetic configurations.

what has to be done with the interstitial magnetic field. Leaving the interstitial magnetic field unchanged, i.e. using the magnetic field obtained from a selfconsistent

ferromagnetic calculation, lead to very unsatisfactory results. The energy difference between the ferromagnetic and the antiferromagnetic structure is massively underestimated, and the 180° ($\uparrow\downarrow\uparrow$) configuration is incorrectly predicted to be lowest in energy (cf. Table 6.2). How large the effect of the interstitial magnetization is, can be appreciated from a comparison of the two 180° configurations, with $2/3$ ($\uparrow\downarrow\uparrow$) and $1/3$ ($\downarrow\uparrow\downarrow$) of the magnetic moments parallel to the interstitial magnetization. These two configurations, that are physically equivalent, differ by 12 mRy/atom, which is far larger than the energy differences we want to calculate. Clearly, the interstitial magnetic field favors the parallel orientation of the atomic moments. These results

$\Delta E = E - E_{FM}$ [mRy/atom]			
Config.	Selfconsistent	FPA no av.	FPA av.
AFM	-20.0	-3.6	-23.4
180° ($\uparrow\downarrow\uparrow$)	-18.8	-9.0	-23.0
180° ($\downarrow\uparrow\downarrow$)	-18.8	+3.0	-23.0

Table 6.2: Energy differences between the ferromagnetic configuration and different collinear antiferromagnetic configurations of the Cr UML-Ag(111). The first column contains the results of selfconsistent calculations. The frozen potential approximation without setting to zero (averaging) the interstitial and vacuum magnetic field (FPA no av.) yields the results in the second column. The last column (FPA av.) lists the results obtained with the frozen potential approximation, with zero interstitial and vacuum magnetic field.

can be substantially improved, if the interstitial and vacuum magnetic field is set to zero (averaged) (cf. section 4.1). The corresponding calculation (cf. Table 6.2) reproduce the correct trends. The antiferromagnetic structure is correctly predicted to be lowest in energy, and the two physically equivalent 180° configurations have the same energy. However, the energy differences between the antiferromagnetic and the ferromagnetic structures are overestimated by about 15%. The averaging of the magnetic field favors the antiferromagnetic systems, because they have smaller interstitial magnetizations and magnetic fields than the ferromagnetic structure. When comparing two antiferromagnetic configuration the quantitative error is smaller, but still present.

6.4 Results for the Cr UML

Our calculations for the Cr UML indeed show, that the 120° configuration is lowest in energy. This configurations is almost 4 mRy lower than the antiferromagnetic

structure, which is the collinear configuration with the lowest energy we found (cf. Table 6.3). This energy difference is clearly larger than the the error we should

$\Delta E = E - E_{FM}$ [mRy/atom]	
Config.	FPA av.
AFM	-23.4
180°	-23.0
120°	-27.2

Table 6.3: Energy differences between different collinear antiferromagnetic structures including the 120° configuration and the ferromagnetic structure of the Cr UML-Ag(111). All results have been obtained from the frozen potential approximation where the interstitial and vacuum magnetic field has been set to zero (averaged) (FPA av.).

expect, when comparing two antiferromagnetic structures. We also calculated the energy dependence on the angle of the local magnetization along two different paths, which transform the ferromagnetic structure into the antiferromagnetic (Fig. 6.1 (c)) and the 120° (Fig. 6.1 (d)) configuration respectively. The results are presented in Fig. 6.2. The curve that corresponds to paths Fig. 6.1 (c) shows a cosine like shape, while the curve corresponding to 6.1 (d) possesses a pronounced minimum at 120°. Following the latter curve further leads to the 180° configuration, which is slightly higher in energy than the antiferromagnetic configuration. In order to check our initial assumption of a Heisenberg like behavior, we fitted the data in Fig. 6.2 to the Heisenberg model including nearest neighbor interaction only. Within this model the energy per unit cell is given by:

$$E = \frac{1}{2} \sum_i^M \sum_j^{nn(i)} J_1 \mathbf{S}_i \cdot \mathbf{S}_j \quad (6.1)$$

The first sum is over the atoms in the unit cell and the second sum is over the nearest neighbors of each atom. For the path Fig. 6.1 (c) this amounts to the following energy per $c(2 \times 2)$ unit cell.

$$E = \frac{1}{2} J_1 \mathbf{S}^2 [8 \cos(\alpha) + 4] \quad (6.2)$$

For the path Fig. 6.1 (d) the energy per $(\sqrt{3} \times \sqrt{3})R30^\circ$ unit cell is given by:

$$E = \frac{1}{2} J_1 \mathbf{S}^2 [12 \cos(\alpha) + 6 \cos(2\alpha)] \quad (6.3)$$

Since the *ab-initio* calculations contain more than just the spin interaction energy, the energies are shifted by a constant. Therefore, the actual functions the results

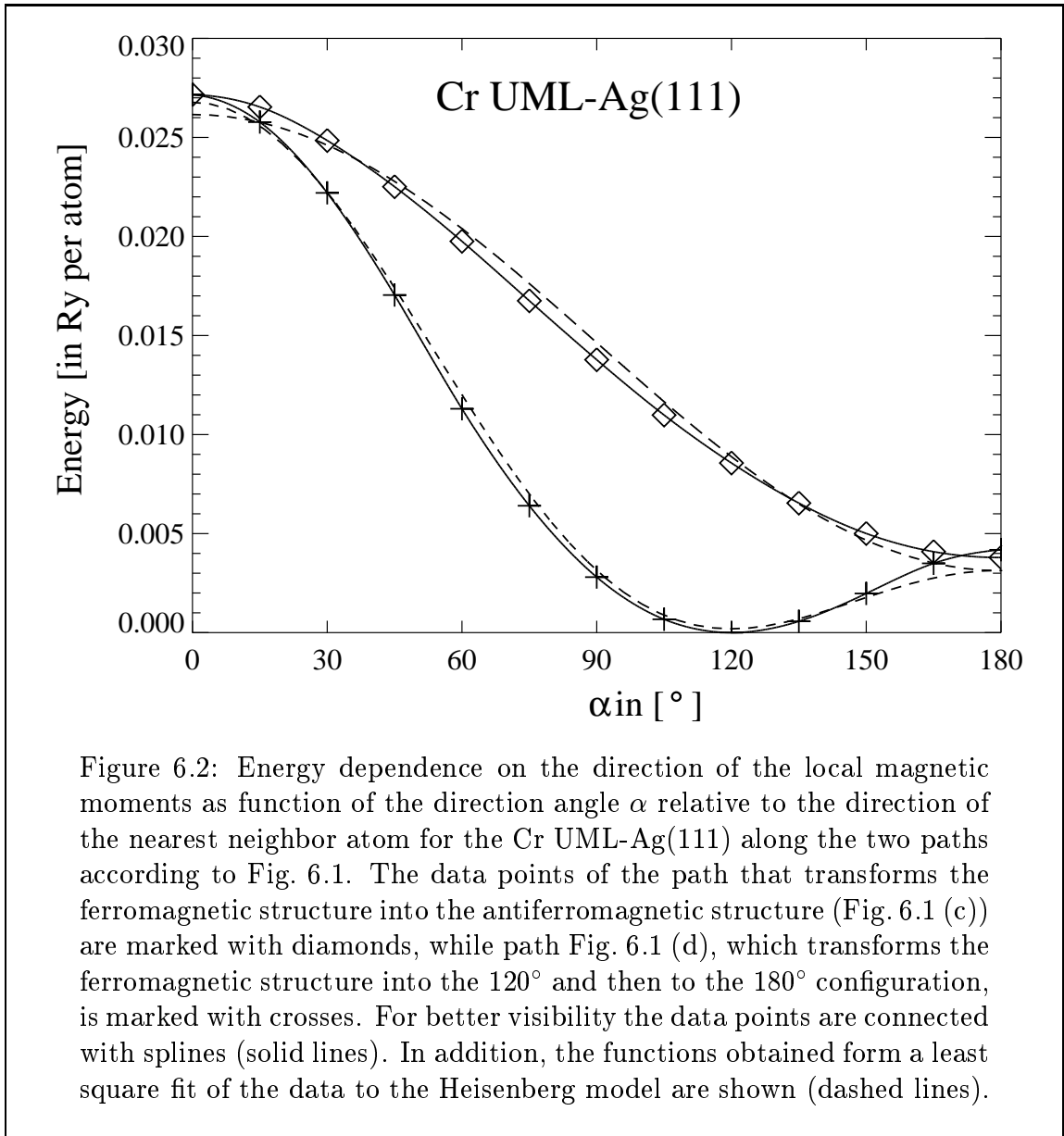


Figure 6.2: Energy dependence on the direction of the local magnetic moments as function of the direction angle α relative to the direction of the nearest neighbor atom for the Cr UML-Ag(111) along the two paths according to Fig. 6.1. The data points of the path that transforms the ferromagnetic structure into the antiferromagnetic structure (Fig. 6.1 (c)) are marked with diamonds, while path Fig. 6.1 (d), which transforms the ferromagnetic structure into the 120° and then to the 180° configuration, is marked with crosses. For better visibility the data points are connected with splines (solid lines). In addition, the functions obtained from a least square fit of the data to the Heisenberg model are shown (dashed lines).

have been fitted to are:

$$E = \frac{1}{2}J_1\mathbf{S}^2[8 \cos(\alpha)] + C \quad (6.4)$$

and

$$E = \frac{1}{2}J_1\mathbf{S}^2[12 \cos(\alpha) + 6 \cos(2\alpha)] + C \quad (6.5)$$

respectively. The fitted functions are also plotted in Fig. 6.2. The linear parameters J_1 and C have been obtained from a least square fit. The fitted Heisenberg curves are in good agreement with the data points. From both fits the exchange integral J_1 can be calculated, using the local magnetization from the selfconsistent ferromagnetic calculation as \mathbf{S} . The values that we obtained differ by only about 2%. We found

$J_1 = 0.168mRy/\mu_B^2$ for the paths according to Fig. 6.1 (c) and $J_1 = 0.172mRy/\mu_B^2$ for the paths according to Fig. 6.1 (d). These results justify the initial assumption of a Heisenberg like behavior.

Bandstructure of the Cr UML for Different Spin Configurations

In this section we will explain how the bandstructure of the Cr UML changes with the orientation of the local magnetic moments along path Fig. 6.1 (d). The corresponding magnetic configurations, including the 120° configuration, require a $(\sqrt{3} \times \sqrt{3})R30^\circ$ unit cell, containing three atoms. Therefore, we will first discuss how the bands in the Brillouin zone of the $p(1 \times 1)$ unit cell are “folded” into the Brillouin zone corresponding to the larger unit cell. For simplicity this will be done for the bandstructure obtained from a non-magnetic calculation. The two Brillouin zones are shown in Fig. 6.3. The Brillouin zone of the $(\sqrt{3} \times \sqrt{3})R30^\circ$ unit cell is by a factor

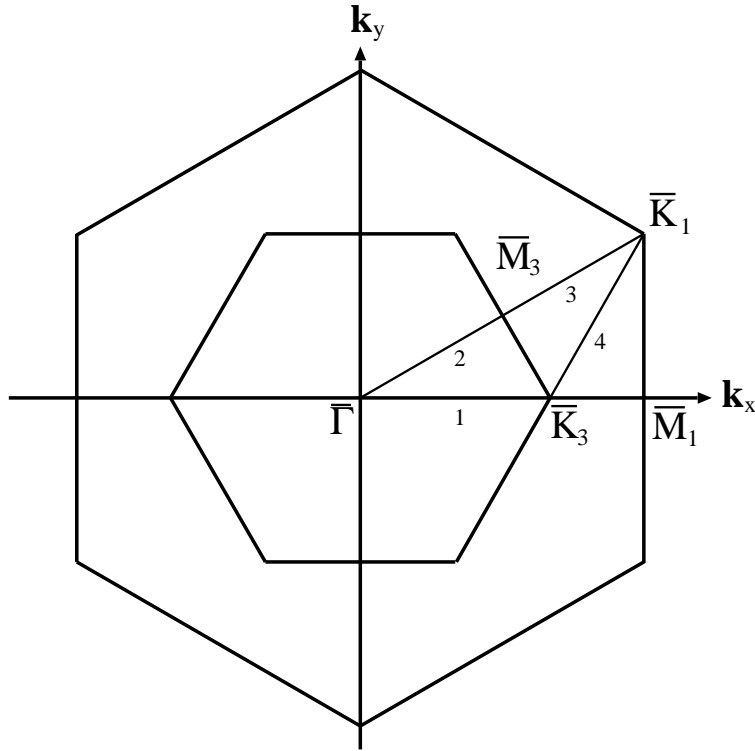


Figure 6.3: The Brillouin zones corresponding to the one and three atom unit cells. The smaller Brillouin zone, which corresponds to the three atoms unit cell, is rotated by 30° with respect to the larger Brillouin zone. The index of the symmetry points corresponds to the number of atoms the unit cell contains.

three smaller, and it is rotated by 30° with respect to the Brillouin zone of the $p(1 \times 1)$

unit cell. All bandstructures are plotted along the symmetry lines $\bar{\Gamma}-\bar{M}$ and $\bar{\Gamma}-\bar{K}$. The index of the symmetry points corresponds to the number of atoms the unit cell contains. Due to the rotation of the Brillouin zone the symmetry line $\bar{\Gamma}-\bar{M}_3$ of the $(\sqrt{3} \times \sqrt{3})R30^\circ$ Brillouin zone lies on the line $\bar{\Gamma}-\bar{K}_1$ of the $p(1 \times 1)$ Brillouin zone. Thus, the bandstructure along $\bar{\Gamma}-\bar{K}_1$ folds onto $\bar{\Gamma}-\bar{M}_3$ and correspondingly $\bar{\Gamma}-\bar{M}_1$ folds onto $\bar{\Gamma}-\bar{K}_3$.

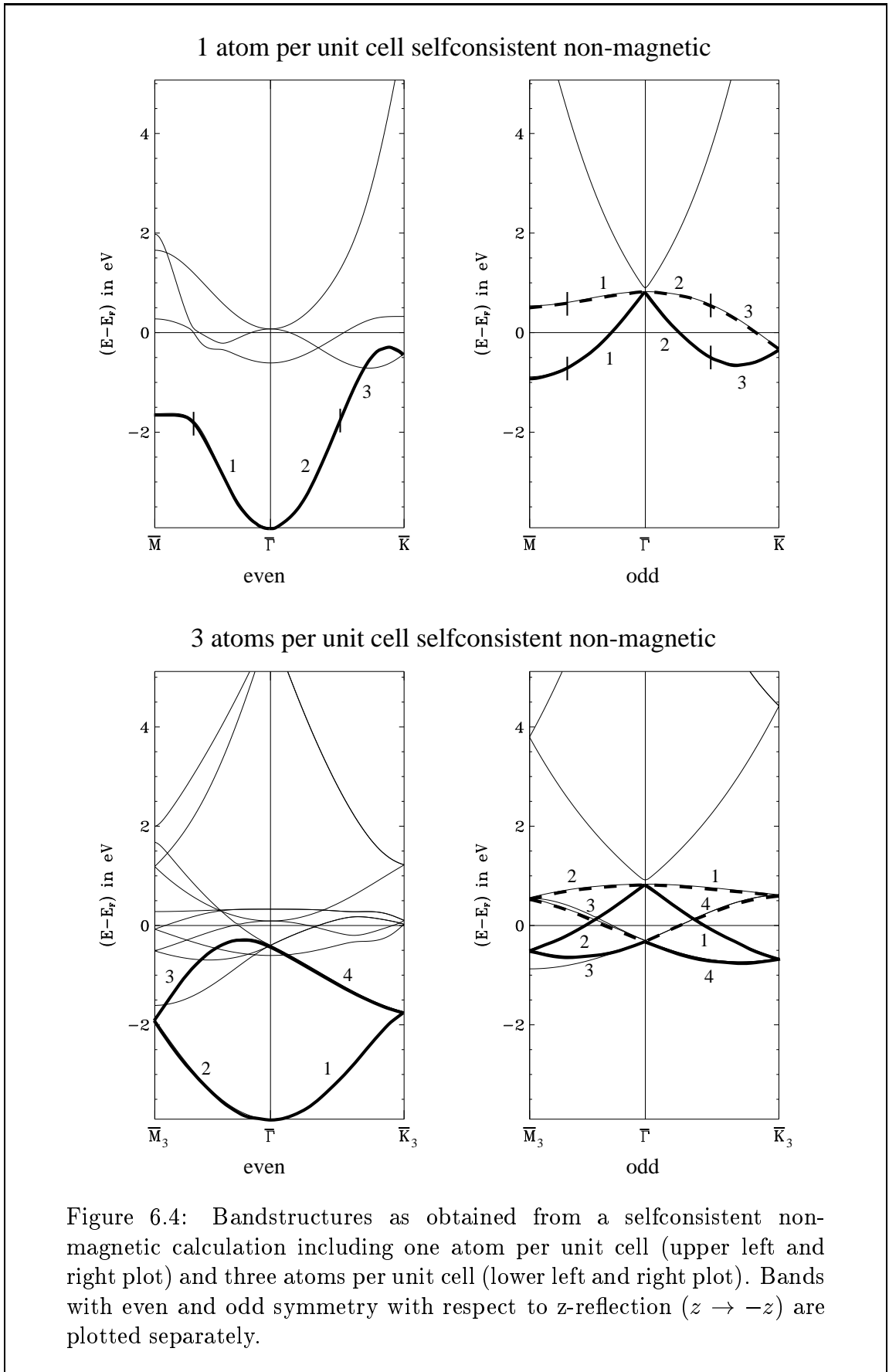
The bandstructures of a non-magnetic Cr UML with one and three atoms per unit cell are shown in Fig. 6.4. The UML clearly possesses symmetry with respect to a reflection at the x-y-plane ($z \rightarrow -z$). Therefore, all eigenfunction have to be either even or odd with respect to this operation. Although no selection rule for an experiment can be derived from this symmetry, for better visibility the corresponding bands are plotted separately. The left panels of Fig. 6.4 show the even bands of a non-magnetic calculation, the right panels show the odd bands. The upper panels show the bandstructure resulting from non-magnetic calculations containing one atom per unit cell, the lower panels show the bandstructure resulting from calculations containing three atoms. A first look reveals two types of bands. Around the Fermi energy we find the d -bands showing little dispersion. Below the Fermi energy and above about 2 eV we find strongly dispersive bands. The latter are basically of s -symmetry for even states and of p_z -symmetry in the case of the odd states. Comparing the upper left plot to the lower left graph it can be seen how the s -band (thick solid line) is folded into the smaller Brillouin zone of the three atom calculation. The part of this band between $\bar{\Gamma}$ and \bar{K}_1 (marked (2) and (3)) becomes folded onto $\bar{\Gamma}-\bar{M}_3$. Part of the band between \bar{M}_1 and $\bar{\Gamma}$ (1) can be identified on $\bar{\Gamma}-\bar{K}_1$, while the bandstructure between \bar{K}_3 and \bar{M}_1 cannot be found in the plot of the three atom unit cell. The latter part of the band could be found on the symmetry line $\bar{K}_3-\bar{M}_3$ of the smaller Brillouin zone, if it had been plotted. Instead another band (4) can be seen on $\bar{\Gamma}-\bar{K}_3$, which originates from $\bar{K}_3-\bar{K}_1$. In the same way the lowest two odd bands (upper right plot of Fig. 6.4 thick solid and dashed lines) are folded into the small Brillouin zone. As a consequence of the folding, the folded bands become degenerate at high symmetry points.

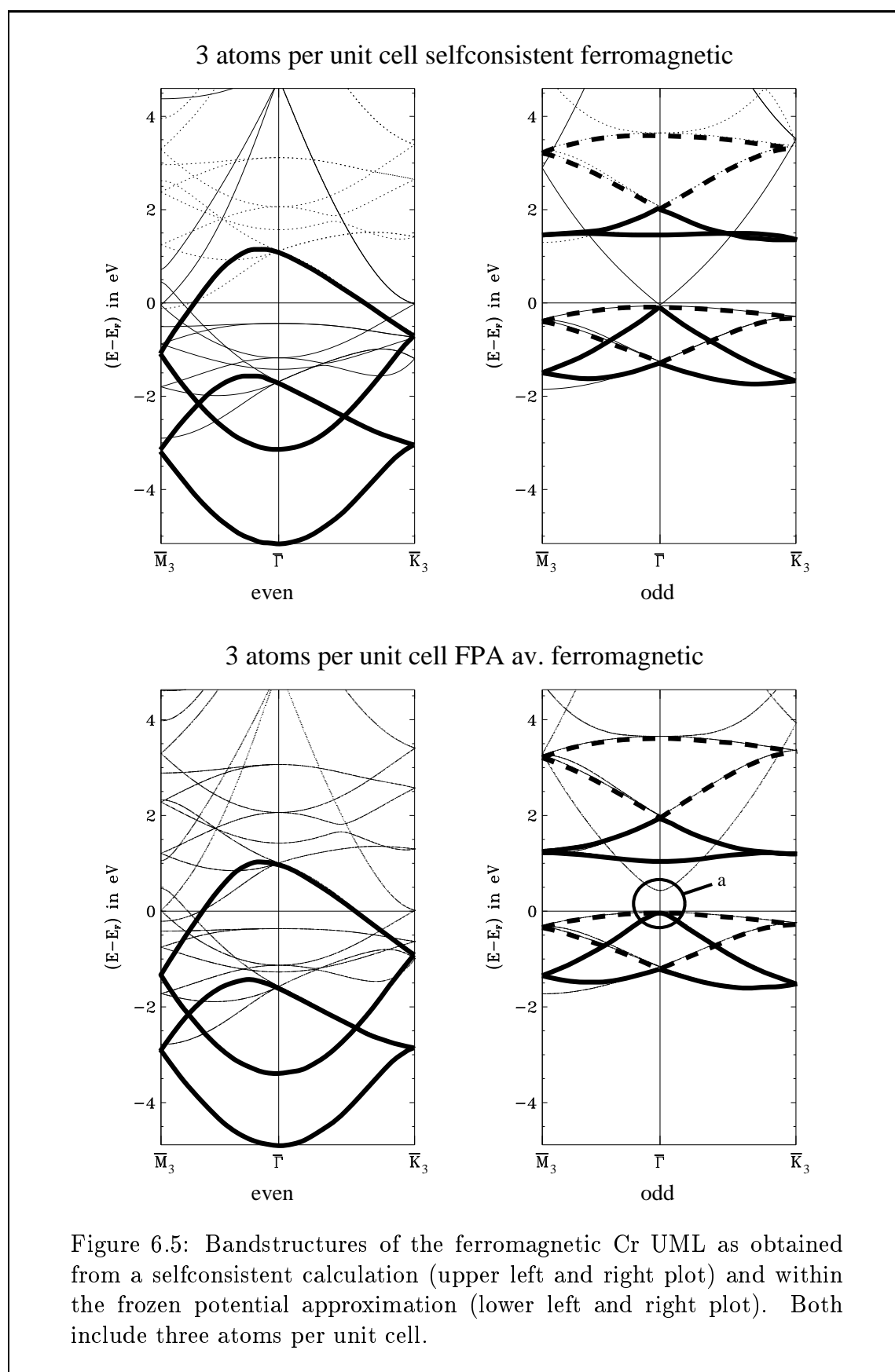
The non-collinear magnetic configurations break the symmetry and thus some of the degeneracies are lifted. In Fig. 6.5 the ferromagnetic bandstructure is shown, as obtained from a selfconsistent calculation (upper left and right plots) and from a calculation within the frozen potential approximation with zero interstitial and vacuum magnetic field (lower left and right plots). Since we used the ferromagnetic potential and magnetic field for all non-selfconsistent calculations, the only difference between the two calculations is the removal of the interstitial magnetic field. In the upper graphs the bands are plotted differently according to their spin character (solid lines indicate majority spin, dotted lines indicate minority spin). At first we see a large exchange splitting between the majority and minority states, which amounts to about 3.5 eV for bands with predominantly d -character. This reflects the large magnetic moment of about $4 \mu_B$. A closer look reveals that the spin splitting of the bands is not rigid as expected from the simple Stoner model. The minority

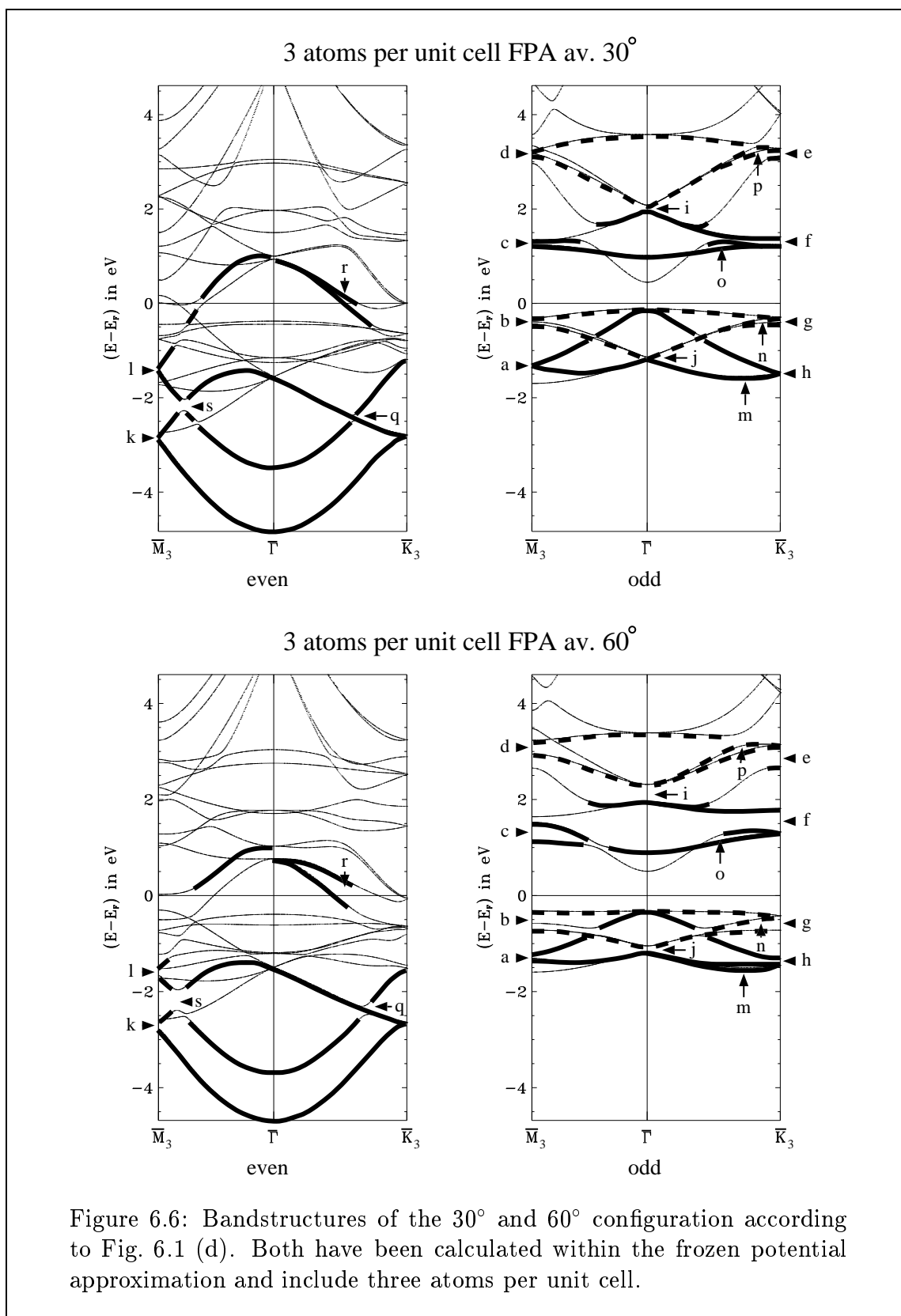
bands show a larger dispersion, since they are considerably higher in energy and as such much less localized than the majority states. The FPA calculation shows a slightly smaller difference between the spin up and down bands due to the missing interstitial and vacuum magnetic field. The most significant difference is a gap in the p -band denoted (a) in Fig. 6.5 that results from the FPA, apart from this gap the bandstructures are very similar.

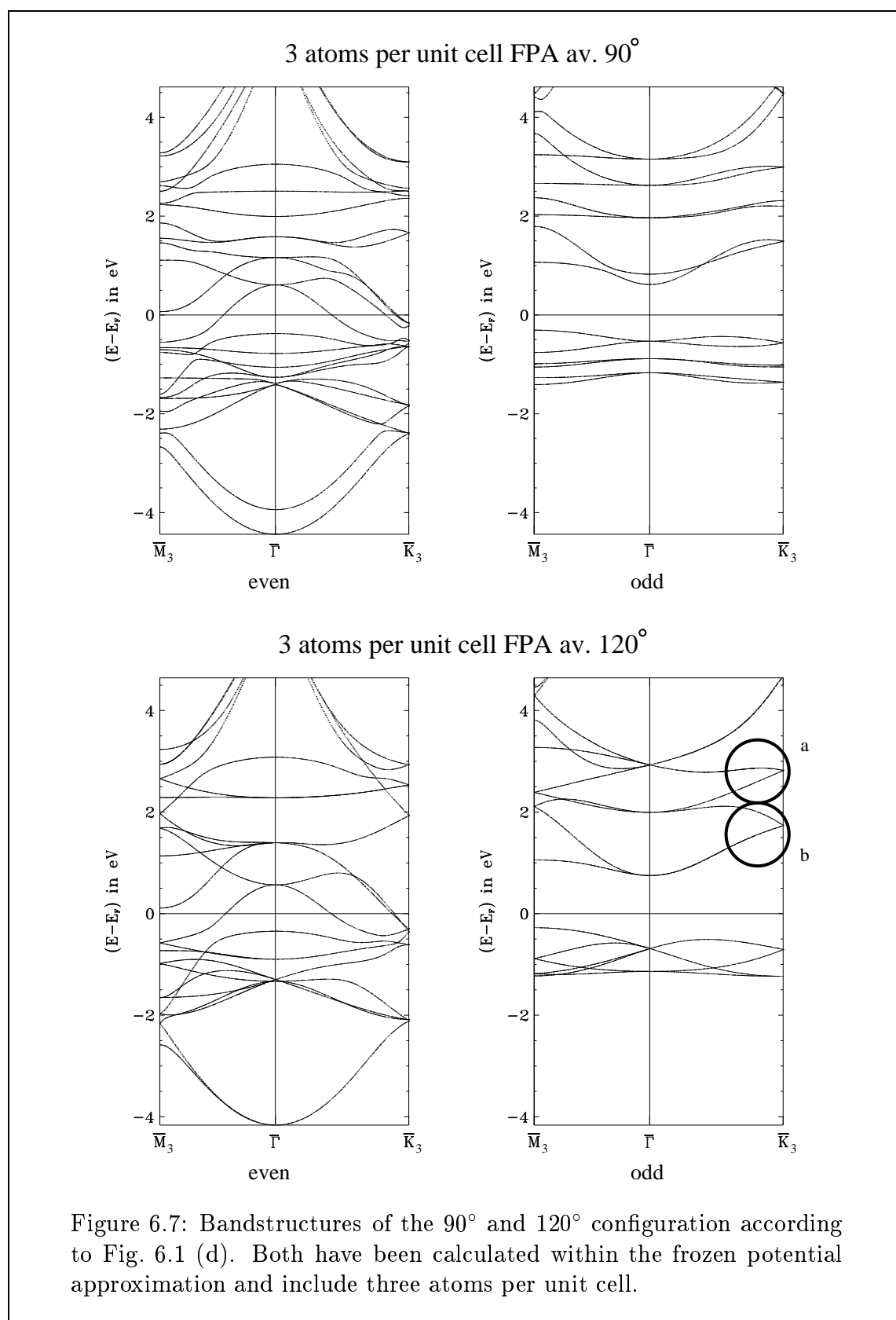
In Fig. 6.6 we present the bandstructure after a rotation of the magnetic moments of 30° and 60° according to Fig. 6.1 (d). Due to the rotation of the magnetic moment spin up and spin down electrons hybridize (s). For small rotation angles (30°) we observe an opening of band-gaps at the symmetry points (a-l), where the bands were degenerate in the ferromagnetic configuration. The size of these gaps increases with the rotation angle. In addition some bands, that were degenerate along the symmetry line $\bar{\Gamma}-\bar{K}$ split up (m-r). At a certain rotation angle the mixing of spin up and down states is so strong, that the ferromagnetic configuration becomes meaningless as a starting point to explain the band topology. Spin up and down states form new linear combinations.

At 90° and 120° the bandstructure has change dramatically (Fig. 6.7). The 120° configuration is highly symmetric. As a result, bands, that were split at intermediate angles, become degenerate at symmetry points and between $\bar{\Gamma}$ and \bar{K} . A comparison between the ferromagnetic structure and the 120° configuration shows, that the band structure has drastically changed. For example two of the (odd) bands near \bar{K} (a,b) are completely different for the two configurations. Such differences can be used to investigate experimentally the existence of the 120° structure with methods that probe the bandstructure. However, two problems have to be taken into account. First, the density functional theory does not always predict the position of bands accurately. Therefore, it is necessary to use methods, that can probe also the dispersion of the bands, like angle resolved ultraviolet photo emission (ARUPS). The second problem, that has to be taken into account, is that the present calculations have been done with unsupported monolayers, which leads to less dispersion, and increases the exchange splitting.









6.5 Results for the Mn UML

The second system that has been studied as part of this work is the Mn UML with Cu(111) geometry. In order to check whether the assumption underlying the FPA, that the magnetic moments change little with their direction is valid, we performed selfconsistent calculations for different collinear configurations. As in the case of the Cr monolayer the results show, that this assumption is justified (cf. Table 6.4). However, the Mn moments are considerably smaller than the Cr moments, and at the

Atomic magnetic moments [in μ_B]	
FM	3.05
AFM	3.08
180° ($\uparrow\downarrow\uparrow$)	$m_\uparrow = 3.23, m_\downarrow = 2.93$

Table 6.4: Selfconsistent local magnetic moment per atom of the Mn UML-Cu(111) for different collinear magnetic configurations.

same time the sum of the interstitial and vacuum magnetization is larger due to the smaller lattice constant of Cu. The ferromagnetic calculations yielded an interstitial and vacuum magnetization of $0.26 \mu_B/atom$ for the Cr UML and $0.39 \mu_B/atom$ for the Mn UML. Thus, the ratio of local and interstitial magnetization is significantly smaller for the Mn monolayer, which makes the approximation in the interstitial and vacuum region less accurate in the case of the Mn UML-Cu(111) system. As a consequence, the energy differences between the ferromagnetic and the antiferromagnetic configurations (AFM and 180°) are more strongly overestimated than in the case of the Cr UML. The predicted energy differences are about 6 mRy/atom larger than those obtained from selfconsistent calculations (cf. Table 6.5). However, the calculated differences between the two antiferromagnetic structures agree very well.

The results of the angle dependent calculations are presented in Fig. 6.8. In contrast to the Cr UML, we do not find the 120° configuration to be lowest in energy for the Mn UML. Instead, the computed energy of the antiferromagnetic configuration is more than 4 mRy/atom lower in energy. Even the 180° structure is predicted to be more stable than the 120° configuration.

The figure also contains the functions obtained from a fit of the data to the nearest neighbor Heisenberg model. Apparently the data is not well described by the Heisenberg model. The graph that corresponds to the rotation according to Fig. 6.1 does not possess a minimum at 120° in contradiction to the Heisenberg model. Instead the energy changes very little with the rotation angle between 90° and 180° . In addition, the values for the exchange integral J_1 differ significantly between the two paths. From the calculation according to path Fig. 6.1 (c) we obtained $J_1 = 0.431 mRy/\mu_B$, while path Fig. 6.1 (d) yielded $J_1 = 0.340 mRy/\mu_B$. This difference

$\Delta E = E - E_{FM}$ [mRy/atom]		
Config.	Selfconsistent	FPA av.
AFM	-26.3	-32.2
180°	-23.2	-29.2
120°	-.-	-27.8

Table 6.5: Energy differences between the ferromagnetic configuration different collinear antiferromagnetic configurations of the Mn UML-Cu(111). The first row contains the results of selfconsistent calculations. The second row contains the results obtained by the frozen potential approximation where the interstitial and vacuum magnetic field has been set to zero (averaged) (FPA av.).

and the fact, that the antiferromagnetic configuration is lower in energy than the 120° configuration can be explained by including next nearest neighbor interaction into the Heisenberg model.

If the next nearest neighbor interaction is taken into account, the energy of a Heisenberg spin system is given by:

$$E = \frac{1}{2} \sum_i^M \sum_j^{nn(i)} J_1 \mathbf{S}_i \cdot \mathbf{S}_j + \frac{1}{2} \sum_i^M \sum_j^{nnn(i)} J_2 \mathbf{S}_i \cdot \mathbf{S}_j \quad (6.6)$$

Where j in the second term sums over the nnn next nearest neighbors of each atom i . Assuming this model the energy per unit cell along the two rotation paths becomes

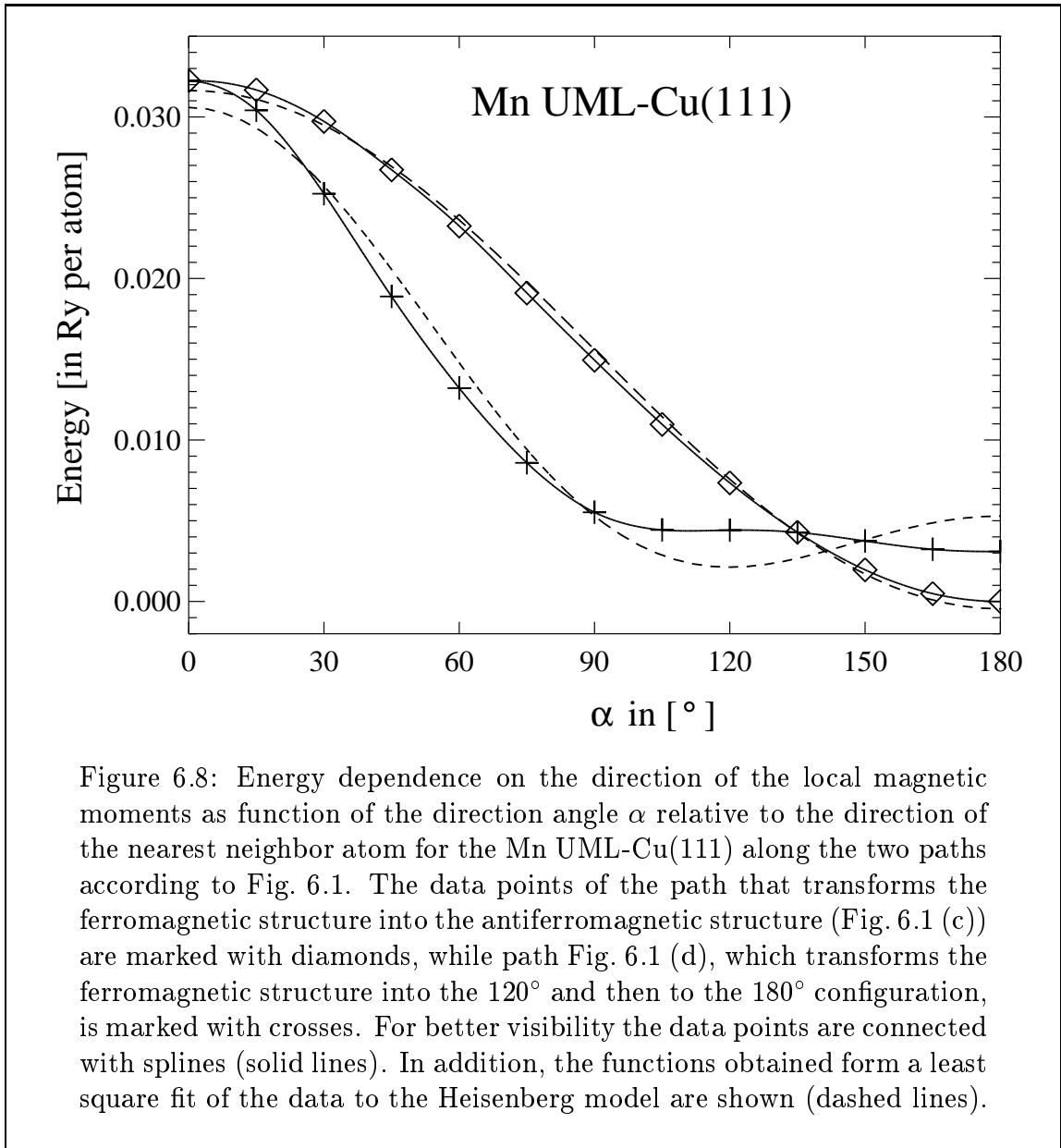
$$E = \frac{1}{2} (J_1 + J_2) \mathbf{S}^2 [8 \cos(\alpha) + 4] \quad (6.7)$$

for path Fig. 6.1 (c) and

$$E = \frac{1}{2} J_1 \mathbf{S}^2 [12 \cos(\alpha) + 6 \cos(2\alpha)] + \frac{1}{2} J_2 \mathbf{S}^2 36 \quad (6.8)$$

for path Fig. 6.1 (d), where the next nearest neighbor interaction contributes only to the constant term. In the case of the rotation according to Fig. 6.1 (c) the contribution to the energy is of the same form as the contribution from the nearest neighbor interaction. Thus, the value we have obtained from the Heisenberg fit is in fact the sum of J_1 and J_2 , in terms of the model including next nearest neighbor interaction.

The very flat shape of the functional dependence of the energy on the rotation angle along the path Fig. 6.1 (d) cannot be explained with the next nearest neighbor interaction. We obtained a far better fit to the *ab-initio* data, when we included a term $\cos(3\alpha)$ into the function the data has been fitted to. In terms of the Heisenberg



model this means, that the energy dependence on the angle is more complex than the simple cos form, and a Fourier series (including only the even (cos) terms) has to be used instead.

Since, the results of the calculations are not well described by the Heisenberg model in the case of the Mn UML-Cu(111), our initial assumption (of a Heisenberg like behavior) is not justified. Therefore, we cannot be sure, that the true ground-state is a magnetic structure we have not investigated, which might have a larger unit cell.

However, during the analysis of the results it must be kept in mind, that the accuracy of the frozen force approximation is limited. This is particularly critical in

the case of the Mn UML, where the ratio of the local and interstitial magnetization is smaller. The question of how much of the predicted properties of the Mn UML is actually physics, and how much is an artifact due to the FPA can only be resolved by carrying out selfconsistent non-collinear calculations.

Chapter 7

Conclusion and Outlook

In the present work we investigated the possibility and energetics of the non-collinear magnetic ground-state for particular ultrathin films. *Ab-initio* calculations based on the density functional theory in the local spin-density approximation have been performed. For this purpose, the FLAPW method has been extended to allow non-selfconsistent calculations for systems with a non-collinear orientation of the magnetic moments. These calculations have been performed within the frozen potential approximation, where the energy difference of the magnetic configurations is determined by the difference of eigenvalue sums. A trial Hamiltonian has been constructed by a rotation of the magnetic field obtained from a selfconsistent ferromagnetic calculation. This method has been applied to unsupported monolayers (UML) of Cr in the geometry of Ag(111) and Mn in the geometry of Cu(111). The calculations predict a non-collinear ground-state for the Cr UML, with 120° angles between the magnetic moments at nearest neighbor sites of the triangular lattice. The dependence of the energy on the rotation angle of the local magnetic moments has been investigated. Fitting the results to a model Hamiltonian showed, that the magnetism of the Cr UML is well described by the Heisenberg model including nearest neighbor interaction only. The bandstructure of the Cr UML has been calculated for different angles of the magnetic moments. The results show, that the bandstructure strongly depends on the magnetic configuration. Thus, experiments, which probe the bandstructure like angle-resolved ultraviolet photo-emission (ARUPS) or inverse photo-emission (BIS), should be able to identify the non-collinear ground-state. In addition, the predicted non-collinear magnetic ground-state breaks the symmetry of the atomic lattice. Therefore, feeble superstructure extra-spots in low energy electron diffraction (LEED) experiments should be expected [TBF88], which disappear or reappear, when the Neel temperature is crossed from below or above. Another way to identify the non-collinear ground-state is given by magnetic circular x-ray dichroism (MCXD) measurements [DvdL96], which allow the determination of the actual local magnetization vector.

In the case of the Mn UML with Cu(111) geometry we got a different picture. The frozen potential approximation proved to be less accurate when applied to this system, due to the smaller local magnetic moments of Mn and the smaller lattice constant

of Cu. Our calculations predicted a collinear antiferromagnetic configuration to be lower in energy than the non-collinear configuration we have found for the Cr UML-Ag(111). In addition, the results were not well described by the Heisenberg model. Therefore, we cannot rule out, that the true ground-state is a magnetic configuration we have not investigated, possibly including a larger unit cell. In order to obtain more accurate results for the Mn monolayer selfconsistent calculations are necessary.

In view of the future development to extend the method to allow an efficient selfconsistent treatment of non-collinear magnetism, the local orbital extension has been implemented. The local orbitals are an extension to the FLAPW method inside the muffin-tin spheres near the atomic nuclei. These extra basis functions improve the variational freedom of the FLAPW basis and make it possible to employ a spin-independent basis set. In order to test the implementation of the local orbitals, they have been applied to the semicore states of bcc W, fcc and hcp Ti. The results have been compared to the results obtained from two-window calculations, where the semicore and valence states are treated within two independent energy windows (panels). Both schemes correctly predicted hcp Ti to be lower in energy than the fcc phase. The calculated lattice constants were in good agreement. The ghost-band problem could be avoided.

The results that have been obtained for the unsupported monolayers of Cr (Ag(111) geometry) and Mn (Cu(111) geometry) show, that the accuracy of the frozen potential approximation in the current implementation is limited. In order to improve the accuracy and to allow the application of the method to a larger class of systems, which do not satisfy the requirement of large local magnetic moments which are well-confined inside the muffin-tin spheres around the atoms or that the magnitude of the local moments remains unchanged during rotation, it is essential to extend the method to selfconsistent non-collinear calculations. Several ways of performing such selfconsistent calculations are possible. One option is to allow a general magnetization density in the interstitial region, with both, magnitude and direction, depending on the position vector \mathbf{r} , while having the magnetization inside each muffin-tin point along a single direction. Within this approximation the rotation of the atomic magnetic moments with respect to each other, the inter-atomic non-collinear magnetism, can be described, while changes of the direction of the magnetization inside single atoms, the intra-atomic non-collinear magnetism, is neglected. The most general scheme is to allow the magnetization to have a different direction everywhere in space, and thus to include also the intra-atomic non-collinear magnetism.

The combination of non-collinear magnetism with the possibility to calculate the force acting on an atom to perform a structure optimization by molecular dynamics, which is already implemented in our current FLAPW code, opens the gate to future treatment of systems, where both the magnetic properties, including the magnetization direction, and the structural properties are intimately interwoven, and the atomic and the magnetic structure is *a priori* unclear. This is of particular importance for low dimensional systems, like reconstructed surfaces, ultrathin films with and without defects, step edges, magnetic chains at step edges, small magnetic clusters or for the

investigation of the growth (diffusion barrier and atom exchange mechanisms) and reaction paths involving magnetic atoms.

Bibliography

- [And75] O. K. Andersen. *Phys. Rev. B*, 12:3060, 1975.
- [AWJE93] R. Ahuja, J.M. Wills, B. Johansson, and O. Eriksson. Crystal structures of Ti, Zr, and Hf under compression: Theory. *Phys. Rev. B*, 22:16269, 1993.
- [BDZD89] S. Blügel, D. Drittler, R. Zeller, and P. H. Dederichs. Magnetic properties of 3d-monolayers on metal substrates. *Appl. Phys. A*, 49:547, 1989.
- [BJA94] P.E. Blöchl, O. Jepsen, and O.K. Andersen. Improved tetrahedron method for brillouin-zone integrations. *Phys. Rev. B*, 49:16223, 1994.
- [Blü88] S. Blügel. First principles calculations of the electronic structures of magnetic overlayers on transition metal surfaces. Jül. Report 2197, Forschungszentrum Jülich, 1988.
- [Blü95] S. Blügel. Groundstate properties of ultrathin magnetic films, habilitation. RWTH Aachen, 1995.
- [BSSS92] P. Blaha, D.J. Singh, P.I. Sorantin, and K. Schwarz. Electric-field-gradient calculations for systems with large extended-core-state contributions. *Phys. Rev. B*, 46:1321, 1992.
- [CA80] D. M. Ceperley and B. J. Alder. quantum monte carlo. *Phys. Rev. Lett.*, 45:566, 1980.
- [CC73] D. J. Chadi and Marvin L. Cohen. Special points in the brillouin zone. *Phys. Rev. B*, 8:5747, 1973.
- [Cun74] S. L. Cunningham. Special k-points in 2 dimensions. *Phys. Rev. B*, 10:4988, 1974.
- [DG90] R. M. Dreizler and E. K. U. Gross. *Density Functional Theory: An Approach to the Quantum Many-Body Problem*. Springer-Verlag, Berlin, 1990.

- [DvdL96] H.A. Dürr and G. van der Laan. Magnetic circular x-ray dichroism in transvers geometry: Importance of noncollinear ground state moments. *Phys. Rev. B*, 54:760, 1996.
- [FFOW85] A. J. Freeman, C. L. Fu, S. Ohnishi, and M. Weinert. page 3. World Scientific, Singapore, 1985.
- [FHW92] T. Flores, M. Hansen, and M. Wuttig. Structure and growth of mn on cu(100). *Surf. Sci.*, 279:251, 1992.
- [FPB⁺90] L. M. Falicov, D. T. Pierce, S. D. Bader, R. Gronsky, K. B. Hathaway, H. J. Hopster, D. N. Lambeth, S. S. P. Parkin, G. Prinz, M. Salamon, I. K. Schuller, and R. H. Victora. *J. Mater. Res.*, 5:1299, 1990.
- [FW91] A. J. Freeman and R. Wu. *J. Magn. Magn. Mater.*, 100:497, 1991.
- [Ham79] D. R. Hamann. *Phys. Rev. Lett.*, 212:662, 1979.
- [HK64] P. Hohenberg and W. Kohn. *Phys. Rev.*, 136:B864, 1964.
- [JA71] O. Jepsen and O.K. Andersen. *Solid State Commun.*, 9:1763, 1971.
- [Jac83] J.D. Jackson. *Klassische Elektrodynamik*. Walter de Gruyter, Berlin, New York, 1983.
- [JF84] H.J.F. Jansen and A.J. Freeman. *Phys. Rev. B*, 30:561, 1984.
- [JG89] R. O. Jones and O. Gunnarsson. The density functional formalism, its applications and prospects. *Rev. Mod. Phys.*, 61:689, 1989.
- [KH77] D. D. Koelling and B. N. Harmon. A technique for relativistic spin-polarized calculations. *J. Phys. C.*, 10:3107, 1977.
- [Koe72] D.D. Koelling. *Phys. Rev. B*, 2:290, 1972.
- [Koh85] W. Kohn. *Highlights of Condensed Matter Theorie*. North Holland, Amsterdam, 1985.
- [Koh95] B. Kohler. *Wasserstoffinduzierte Phononenanomalien der Mo(110)- und W(110)-Oberflächen*. PhD thesis, Technische Universität Berlin, 1995.
- [KPF79] H. Krakauer, M. Posternak, and A. J. Freeman. Linearized augmented plane-wave method for the electronic band structure of thin films. *Phys. Rev. B*, 19:1706, 1979.
- [KS65] W. Kohn and L. J. Sham. *Phys. Rev.*, 140:A1133, 1965.

- [Küb95] J. Kübler. Derivation of the single-particle schrödinger equation: Density and spin-density functional theory and the magnetic susceptibility, noncollinear ground states, towards the curie temperature. 1995. Lecture Notes from: Workshop on Condensed Matter Physics.
- [Lev79] M. Levy. Universal variational functionals of electron densities, first-order density matrices, and natural spin-orbits and solutions of the v-representability problem. In *Proc. Natl. Acad. Sci. USA*, volume 76, page 6062, 1979.
- [LMF85] J. Tersoff L. M. Falicov, R. H. Victora. In *The Structure of Surfaces*, volume 2 of *Springer Ser. Surf. Sci.*, page 453, Berlin and Heidelberg, 1985. Springer.
- [Lou67] T. Loucks. *Augmented Plane Wave Method*. Benjamin, New York, 1967.
- [LT72] G. Lehmann and M. Taut. On the numerical calculation of the density of states and related properties. *Status Solidi B*, 54:469, 1972.
- [MH86] L.F. Mattheiss and D.R. Hamann. Linear augmented-plane-wave calculation of the structural properties of bulk Cr, Mo, and W. *Phys. Rev. B*, 33:823, 1986.
- [MJW78] V. L. Moruzzi, J. F. Janak, and A. R. Williams. Pergamon, New York, 1978.
- [NKD86] W. Ning, C. Kailai, and W. Dingsheng. Work function of transition-metal surface with submonolayer alkali-metal coverage. *Phys. Rev. Lett.*, 56:2759, 1986.
- [NS96] L. Nordström and D.J. Singh. Noncollinear intra-atomic magnetism. *Phys. Rev. Lett.*, 76:4420, 1996.
- [OH93] G. Otter and R. Honecker. *Atome Moleküle Kerne, Band I Atomphysik*. B.G. Teubner, Stuttgart, 1993.
- [Pen96] R. Pentcheva. Ab-initio Rechnungen zum Zusammenhang zwischen Magnetismus und Struktur ultradünner Filme. Master's thesis, Universität Köln, 1996.
- [PZ81] J. P. Perdew and A. Zunger. *Phys. Rev. B*, 23:5048, 1981.
- [Ros61] E.M. Rose. *Relativistic Electron Theory*. Wiley, New York, 1961.
- [SDKW] A.B. Shick, V. Drchal, J. Kudrnovsky, and P. Weinberger. submitted.
- [SHK89] J. Sticht, K.H. Höck, and J. Kübler. Non-collinear itinerat magnetism: the case of mn₃sn. *J. Phys.: Condens. Matter*, 1:8155, 1989.

- [Sie92] H. C. Siegmann. *J. Phys.: Condens. Matter*, 4:8395, 1992.
- [Sin91a] D.J. Singh. Adequacy of the local-spin-density approximation for gd. *Phys. Rev. B*, 44:7451, 1991.
- [Sin91b] D.J. Singh. Ground-state properties of lanthanum: Treatment of extended-core states. *Phys. Rev. B*, 43:6388, 1991.
- [Sin94] D. Singh. *Planewaves, Pseudopotentials and the LAPW Method*. Kluwer Academic Publishers, Boston/Dordrecht/London, 1994.
- [SK91] D.J. Singh and H. Krakauer. H-point phonon in molybdenum: Super-linearized augmented-plane-wave calculations. *Phys. Rev. B*, 43:1441, 1991.
- [SK96] L.M. Sandratskii and J. Kübler. Non-collinear magnetism: effects of symmetry and relativity. *HCM newsletter*, 14:42, 1996.
- [Sla37] J. C. Slater. *Phys. Rev.*, 51:846, 1937.
- [Sto94] J. Stoer. *Numerische Mathematik 1*. Springer-Verlag, Berlin, 1994.
- [TBF88] E. Tamura, S. Blügel, and R. Feder. On the determination of surface antiferromagnetism by low-energy electron diffraction. *Solid State Commun.*, 65:1255, 1988.
- [Ter87] K. Terakura. volume 49 of *Studies in Physical and Theoretical Chemistry*. Elsevier, Amsterdam, 1987.
- [vBH72] U. von Barth and L. Hedin. local density approximation. *J. Phys. C.*, 5:1629, 1972.
- [VWN80] S. H. Vosko, L. Wilk, and N. Nusair. local density approximation. *Can. J. Phys.*, 58:1200, 1980.
- [Wan50] G.H. Wannier. *Phys. Rev.*, 79:357, 1950.
- [WB93] M. Weinert and S. Blügel. First-principles calculations of magnetic interfaces and multilayers. In L. H. Bennett and R. E. Watson, editors, *Magnetic Multilayers*, Singapore, 1993. World Scientific.
- [Wei81] M. Weinert. *J. Math. Phys.*, 22:2433, 1981.
- [WKWF81] E. Wimmer, H. Krakauer, M. Weinert, and A.J. Freeman. *Phys. Rev. B*, 24:864, 1981.
- [WWF82] M. Weinert, E. Wimmer, and A.J. Freeman. Total-energy all-electron density functional method for bulk solids and surfaces. *Phys. Rev. B*, 26:4571, 1982.

- [YFP⁺91] J. Yu, A.J. Freeman, R. Podloucky, P. Herzig, and P. Weinberger. Origin of electric field gradients in high temperature superconductors: $\text{YBa}_2\text{Cu}_3\text{O}_7$. *Phys. Rev. B*, 43:532, 1991.

Danksagung

Herrn Professor Dr. W. Eberhardt danke ich für die Möglichkeit, an seinem Institut diese Diplomarbeit erstellen zu dürfen.

Mein besonderer Dank gilt meinem Betreuer Dr. S. Blügel für die interessante Themenstellung und die intensive Unterstützung dieser Arbeit. Er hat sich immer viel Zeit genommen für Diskussionen, von denen ich sehr profitiert habe. Die freundschaftliche und entspannte Atmosphäre dieser Diskussionen habe meine Kreativität gefördert und dazu beigetragen, daß mir die Arbeit viel Spaß bereitet hat.

Für die gute und freundschaftliche Zusammenarbeit bedanke ich mich bei Frau Dipl. Phys. R. Pentcheva, Herrn Dr. A. Shick, Herrn S. Heinze und Herrn Dr. G. Bihlmayer.

Allen Mitarbeitern der Institute IEE und Theorie III danke ich für die Hilfsbereitschaft, für die angenehme Arbeitsatmosphäre, für viele interessante Diskussionen und auch für viele unterhaltsame Gespräche, die nichts mit der Physik zu tun hatten.

Ein besonders großer Dank gilt meiner Freundin Dunja, für ihre liebevolle Unterstützung und ihr Verständnis, mit dem sie mich während der gesamten Arbeit begleitete.

Nicht zuletzt danke ich meinen Eltern, die mich über die Jahre hinweg immer unterstützt haben und mir Rückhalt gaben. Ihnen verdanke ich meine Ausbildung und damit auch die Möglichkeit, diese Diplomarbeit anzufertigen.

Ein Großteil der Rechnungen wurden auf den CRAY X-MP Computern der KFA und des Höchstleistungsrechenzentrums (HLRZ) durchgeführt sowie auf dem CRAY T90 Computer im Rahmen des Projektes *Magnetismus, Struktur und elektronische Struktur von Oberflächen und ultradünnen Filmen*. Diese Arbeiten wurden unterstützt durch das BMBF im Rahmen des Verbundforschungsprojektes *Erforschung kondensierter Materie mit Synchrotronstrahlung*, Schwerpunkt *Zirkularpolarisierte Synchrotronstrahlung: Dichroismus, Magnetismus und Spinorientierung* und durch den VDI Verbundantrag im Rahmen des Förderprogrammes *Elektronische Korrelationen und Magnetismus*, Schwerpunkt *Austauschgekoppelte magnetische Multischichten für neuartige magnetische und magneto-optische Datenspeicher*.

Lebenslauf

Philipp Kurz

- 08.06.1971 geboren in Haan
Eltern: Gerhard Kurz und Ursula Kurz, geb. Krant
- 1977 – 1981 Grundschule, Gemeinschaftsschulen Nützenberger Straße,
Wuppertal
- 1981 – 1990 Gymnasium, Städtisches Gymnasium an der Bayreuther Straße
Abschluß: Abitur
- 1990 – 1991 Grundwehrdienst
- 1991 – 1993 Studium der Physik an der RWTH Aachen
- 1993 Vordiplom Physik
- 1993 – 1994 Studium der Physik am Imperial College, London
Abschluß: Imperial College International Diploma (ICIP)
- 1994 – 1995 Fortsetzung des Studiums an der RWTH Aachen
01.04.1995 Studentische Hilfskraft am
– 30.06.1995 Lehrstuhl für Theoretische Physik C der RWTH Aachen
- seit August 1995 Diplomarbeit am Institut für Festkörperforschung
des Forschungszentrums Jülich
- 01.10.1995 Studentische Hilfskraft am Institut für Festkörperforschung
– 30.09.1996 des Forschungszentrums Jülich